Journal of the Serbian Chemical Society

*e*Version
*e*lectronic

Available on line at

СХД
1897

www.shd.org.rs/JSCS/

CONTENTS*

* For colored figures in this issue please see electronic version at the Journal Home Page:
http://www.shd.org.rs/JSCS/

Development of biopolymer encapsulated enzyme for efficient acetaminophen degradation

AFAF AHMEDI[1]* and MAHMOUD ABOUSEOUD[2]

[1]*Laboratory of Biomaterials and Transfer Phenomena (LBMPT), Department of material Sciences, Faculty of Sciences, University Yahia Fares of Médéa, Médéa, 26000, Algeria and* [2]*Department of process and Environmental Engineering, Faculty of Technology, University Yahia Fares of Médéa, Médéa, 26000, Algeria*

Abstract: The study aimed to investigate the effectiveness of partially purified turnip (*Brassica rapa*) peroxidase immobilized in calcium alginate for degrading paracetamol, also known as acetaminophen (AAP), a commonly used over-the-counter analgesic and antipyretic. The encapsulation of peroxidase was optimized to minimize enzyme leakage and maintain maximum activity by adjusting the sodium alginate content, enzyme loading, and calcium chloride concentration. The optimal conditions for encapsulating peroxidase in calcium alginate matrices with the best retention and efficiency were determined to be 1.3 U/mL enzyme loading, 1.5 % sodium alginate, and 0.05 M calcium chloride concentration. This research focuses on investigating the efficacy and application of immobilized turnip peroxidase in degrading pharmaceutical effluents, specifically targeting paracetamol. The results revealed the maximum degradation of AAP at a pH of 2.0 and a temperature of 30 °C, with paracetamol and hydrogen peroxide concentrations of 1g/L and 1.2 mol/L, respectively, resulting in a 97 % yield using the stabilized peroxidase. The study also determined the kinetic characteristics of the enzymatic reaction, such as the maximum rate and the Michaelis–Menten constant. Furthermore, the stabilized enzyme can be utilized multiple times, specifically up to three occasions, in ideal conditions, while maintaining 80 % of its ability to degrade AAP.

Keywords: calcium alginate; decomposition; peroxidase, pharmaceutical effluent.

INTRODUCTION

Water, the most essential compound on our planet, has supported life for over 4.0 billion years without any other example of such abundant and persistent life conditions.[1] However, water is also the most vulnerable and readily polluted natural resource due to the popularization of synthetic chemical products, domes-

1285

tic and industrial effluents, inappropriate disposal of waste pesticides, agrochemicals, and especially of many therapeutic drugs, posing a major challenge for our society.[2,3] Acetaminophen (AAP), also known as paracetamol, is a widely used medication employed to treat mild pain, such as headaches, joint or muscle discomfort and to reduce fever.[4,5] Its action spectrum is identical to that of non-steroidal anti-inflammatory drugs.[6,7] Paracetamol is a safe and effective analgesic and antipyretic medication that can relieve headaches and eliminate pain without being expensive, with moderately few adverse effects when used at the recommended therapeutic dosage.[8,9]

The partial biodegradation of acetaminophen and other pharmaceutical compounds in urine lead to their presence in treated water.[4,10,11] These compounds, often referred to as active pharmaceutical ingredients (APIs), are introduced into the aquatic environment through wastewater treatment plants (WWTPs), hospital effluents and improper disposal methods.[12,13] Without adequate treatment, there is a high risk of acetaminophen contamination in waters due to its low removal efficiency in wastewater.[14,15] AAP, as an unregulated trace contaminant, can be found in aquatic environments at concentrations ranging from ng/L to μg/L. When taken in therapeutic doses, 58–68 % of the ingested AAP is excreted from the body unchanged.[16] Traditional biological treatments for water contamination do not fully eliminate AAP, with concentrations of several hundred ng/L still detected in treated effluent.[17,18] The conventional methods used to remove acetaminophen from contaminated water typically involve multiple chemical reactions or intensive energy sources, resulting in increased waste disposal costs.[19,20] As a result, there is a growing interest in exploring new methods for the removal of pharmaceutical compounds from the effluent. Bioremediation using enzymes stands out as one of the most secure and sustainable approaches to decontaminating polluted environments.[21] The peroxidase family of enzymes is a subject of extensive research and is considered essential for life in aerobic conditions.[22,23] Peroxidase, an oxidoreductase enzyme, possesses the unique ability to break down hydrogen peroxides, which is the basis for its name.[15] These enzymes can be found in a wide variety of organisms, including plants, bacteria and humans, in various isoforms.[24,25] The most well-known plant enzymes used for paracetamol degradation, include horseradish peroxidase (HRP), a well-studied plant peroxidase capable of oxidizing paracetamol *via* hydrogen peroxide-dependent radical mechanisms; its use has been explored in cancer enzyme prodrug therapy and environmental applications.[26,27] Laccase enzymes, which have also been demonstrated to transform acetaminophen via oxidative coupling leading to polymerized, biologically inactive products.[28]

Chemical modification has been found to enhance TP's activity, improving its stability and catalytic performance, which is beneficial for wastewater treatment involving pharmaceuticals.[29]
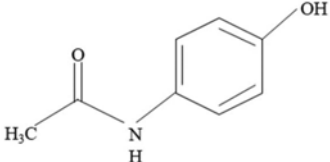
Enzymes are well known for their highly specific catalytic activity, typically at mild reaction conditions, but are highly susceptible to heat and denaturation, resulting in the loss of their catalytic activity.[30] Enzyme immobilization is a process where the enzyme is attached to a surface and trapped in suitable matrices, such as inorganic materials, organic polymers and hydrogels, to enhance their stability, reusability and selectivity.[31,32] Various methods of enzyme immobilization in biopolymers, such as hydrogel beads, have been utilized to encapsulate enzymes in their porous structure.[33] Sodium alginate crosslinking by calcium ions has the properties to form semi-permeable beads with suitable mechanical and chemical stability, as well as good compatibility with enzyme proteins, making it widely used for immobilizing different enzymes.[32] The focus of this study was to investigate the removal of AAP using immobilized turnip peroxidase entrapped in calcium alginate (ITP–Ca-AG) beads. The initial phase involved optimizing the immobilization parameters, including determining the appropriate dose of calcium alginate, the concentration of calcium chloride and the optimal concentration of peroxidase for effective immobilization. Once the optimal conditions for immobilization were established, the study proceeded to examine the effects of various parameters on the removal efficiency, such as pH, temperature, contact time, mass of beads and substrate concentrations of hydrogen peroxide and acetaminophen (AAP).

EXPERIMENTAL

Chemicals

Crude peroxidase was extracted from fresh vegetables of turnip (*Brassica rapa*) collected from local market. Acetone, Sephadex gel G-100, hydrogen peroxide aqueous solution (30 mass %), phenol and 4-amino-antipyrine were of analytical grade and were obtained from Sigma–Aldrich. Paracetamol, also known as acetaminophen, was obtained from Merck. Detailed properties of AAP along with the structure are presented in Table I.

TABLE I. Characteristics of acetaminophen[9]

Name of the drug	Acetaminophen
Chemical name	*N*-Acetyl-*p*-aminophenol
f	$C_8H_9NO_2$
Molecular weight	151.16 g/mol
IUPAC name	*N*-(4-Hydroxyphenyl)acetamide
Stability	Dry, pure paracetamol is stable up to 45 °C
Structure	

Isolation and purification of turnip peroxidase (TP)

The process of separating and purifying TP using acetone at low temperature of 4 °C has been thoroughly explained in prior research.[34,35] Gel filtration serve as the final stage in the purification of proteins, requiring a relatively pristine preparation with a small volume for optimal effectiveness. The stationary phase is composed of Sephadex G-100 gel, which is poured into a column measuring 25 cm×1cm in dimensions. The mobile phase consists of semi-purified TP dissolved in a pH 6.0 buffer solution, which is passed through a 1 cm×60 cm column at a slow flow rate of 15.75 mL/h. The collected solutions were chosen to be in fractions of 1 ml, diluted in 2 ml of the pH 6.0 buffer solution.

Storage stability of TP

Free and partial purified TP were incubated in phosphate buffer at 4 °C (50 mM, pH 6.0). The stability of the peroxidase in both cases, crude and purified, was assessed by measuring the peroxidase activity at regular time intervals every 5 days for a period exceeding three months.

Preparation of alginate beads and optimization of immobilization conditions

The enzyme was purified and then immobilized in sodium alginate using a method similar to one described in a previous study.[35] To achieve this, a volume of semi-purified TP solution was thoroughly mixed with a mass of sodium alginate under continuous agitation until a homogeneous mixture was obtained. Subsequently, this mixture was dispensed dropwise through a 23G syringe needles into a solution of $CaCl_2$ under agitation, resulting in the instantaneous formation of calcium alginate beads with a diameter of approximately 2.8–2.9 mm. These beads were then agitated for about 2 h to harden and stabilize the enzyme within them. Finally, the beads underwent a washing process with distilled water and were stored at 4 °C in a pH 6.0 buffer solution until further use. It is crucial to optimize the parameters related to the support and the enzyme to achieve a higher enzyme retention rate and improved activity. This optimization is necessary to reduce enzyme leakage and overcome diffusional limitations, thereby enhancing process efficiency. The immobilization conditions to be optimized include the concentration of sodium alginate (AG-Na, ranging from 1 to 2.5 %), enzyme loading concentration (measured in UI/ml), and the concentration of the gelating agent $CaCl_2$ (ranging from 0.05 to 0.2 M). The efficiency of immobilization and factor efficiency were calculated using Eqs. (1) and (2), while the activity of free, immobilized, and filtrate TP was measured using the phenol-4 aminoantipyrine method:[36]

$$IE(\%) = 100 \frac{A_0 V_0 - A_f V_f}{A_0 V_0} \tag{1}$$

$$\eta(\%) = 100 \frac{\text{Total activity of beads (U)}}{\text{Total free TP activity used for beads production (U)}} \tag{2}$$

where A_0 and A_f are activities of free and filtrate TP, respectively; V_0 and V_f are the volumes of TP of free and filtrate solution respectively.

Enzyme and protein assay

The activity of free and entrapped peroxidase in aqueous solution was determined spectrophotometrically at 517 nm using the 4-aminoantipyrene method,[36] with phenol and hydrogen peroxide as substrates and 4-aminoantipyrene as the chromogen.[37] Protein concentration was determined by the Bradford method,[38] with absorbance measured at 280 nm, and bovine serum albumin was used to generate the standard calibration curve.

Removal of acetaminophen

Removal of acetaminophen from the aqueous phase by immobilized TP was studied using the one-factor-at-a-time (OFAT) experimental method as shown in Table II and the optimal value was selected for the following experiment. Experiments were conducted in a closed tube under constant temperature 20 °C. The reaction mixtures contained 1 mL of hydrogen peroxide 0.1 M, 1 mL of AAP 0.5 g/L, 8 mL of buffer solution and a mass of 0.3 g of alginate beads. Mixtures were kept for a fixed duration for 1h without agitation and the treated solution was centrifuged at 4000 rpm for 5 min to separate the precipitate. Details are presented in Table II.

TABLE II. Ranges of experimental parameters

Parameter	Range
pH	2–10
Temperature, °C	20–80
$[H_2O_2]$ / M	0.1–1.2
[AAP] / g L^{-1}	0.1–1
m_{beads} / g	0.3–1.5
Contact time, min	0–80

The residual drug concentration was measured spectrophotometrically at 288 nm. Optimum values were those that resulted in the highest degradation yield. Control (blank) experiments were conducted without immobilized TP to assess abiotic (nonenzymatic) degradation *via* photocatalytic or chemical processes. The decomposition yield for acetaminophen was calculated, with the percent degradation parameter defined as:

$$\text{Decomposition yield(\%)} = 100\frac{A_0 - A_t}{A_0} \tag{3}$$

where A_0 and A_t represent the absorbance before and after enzyme treatment, respectively.

Reusability of immobilized TP

The reusability of immobilized TP was investigated by conducting multiple experiments using the same beads for the removal of drug AAP under consistent optimal conditions. The study involved performing consecutive experiments over five batches, with the beads containing immobilized TP being separated from the mixture, rinsed with distilled water, and reused in a fresh degradation medium after each reaction. To monitor the drug biotransformation, absorbance at λ_{max} (288 nm) was measured using UV–Vis spectroscopy at the conclusion of each batch. All enzymatic degradation experiments were conducted in triplicate to ensure the reliability of the results.

RESULTS AND DISCUSSION

Extraction, purification and stability test of TP

Purification of peroxidase is necessary to maintain its maximum catalytic power by removing protein and non-protein impurities. The test results for both the crude and purified extract are summarized in Table III.

Sephadex G-100 gel filtration was used to achieve purification by separating molecules based on their size and shape. The elution profile of the chromatogram

(Fig. 1) demonstrates a complete separation of the compounds, with larger molecules being eluted first. The larger molecules with higher peroxidase activity are eluted between fractions 15 and 20, as indicated by the curve of enzymatic activity variation. The second peak in the elution profile represents proteins that do not possess peroxidase activity.

TABLE III. Characteristics of enzymatic solutions before and after purification

Purification step	Total protein, mg	Total activity, U	Specific activity, U/mg	Purification factor	Activity yield %
Crude enzyme	46.6	2.474	0.053	–	100
Purification with acetone	17.5	1.557	0.089	1.689	63
Sephadex gel G-100 purification	0.045	0.8	17.84	336.60	32
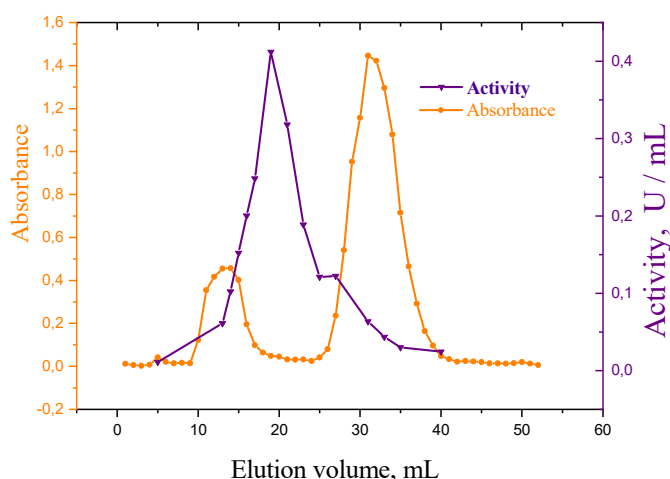
Fig. 1. Elution profile of TP on a Sephadex G-100 resins.

Table III presents the purification process of peroxidase extracted from turnip (*Brassica rapa*), which can be analyzed and explained based on the results provided. A decrease in purification yield indicates the loss of enzyme activity during the purification process, as observed when the purification yield decreases to 63 % with acetone purification and further to 32 % with Sephadex gel filtration. This suggests that significant enzyme activity is lost due to incomplete recovery or enzyme denaturation during these purification steps. The purification factor measures the concentration and purification of the enzyme in each step, with an increase indicating successful concentration and purification. When purified with acetone, the purification factor increases to 1.7, suggesting some initial concentration but not significant purification. In contrast, the purification factor dramatically increases to 336 with Sephadex gel filtration, indicating successful

concentration and purification of the peroxidase enzyme into a smaller volume. In summary, acetone precipitation concentrates the enzyme to some extent with moderate purification, while Sephadex gel filtration greatly concentrates and purifies the peroxidase enzyme, despite a lower final yield. When peroxidase from *Peganum harmala* seeds is purified using gel filtration, a purification fold of 4.4 and an enzyme recovery of 15 % are achieved.[39] On the other hand, the purification of peroxidase from the leaf of oil palm (*Elaeis guineensis*) using the same gel filtration method results in an overall purification fold of 4 with 51.9 % enzyme recovery.[40]

Storage stability of crude and semi-purified TP

Acetone precipitation is a method used to concentrate and stabilize enzymes during the precipitation process. The activity of the crude turnip peroxidase (CTP) can be observed to decrease over time, as shown in Fig. 2. After two weeks, the activity begins to drop and after one month it decreases significantly from 2.3 to 0.4 U/mL. This indicates that the crude enzyme is not stable over time and loses most of its activity within a month. In contrast, the semi-purified enzyme exhibits much better stability, with its activity remaining constant at 1.2 U/mL for three months. This suggests that the purification process with acetone has significantly improved the enzyme's stability. Despite the crude enzyme's higher initial activity, it is less stable and loses most of its activity within a month. On the other hand, the semi-purified enzyme, starting with a lower initial activity of 1.2 U/mL, remains stable and retains its activity for at least three months.
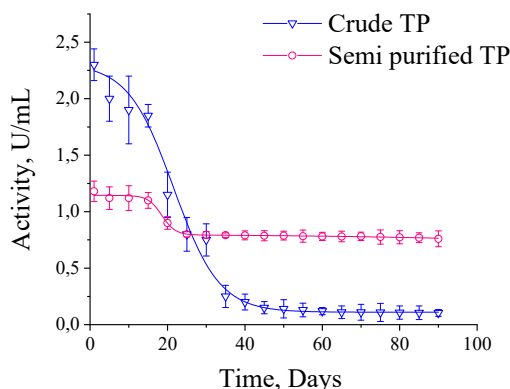
Fig. 2. Storage stability of crude and semi purified TP.

Optimization of immobilization parameters for paracetamol degradation

Alginate is a commonly used biopolymer for immobilization by inclusion due to its gelling properties, non-toxicity, biodegradability, ease of use and cost--effectiveness. The efficiency of immobilization increases with the concentration of the support, specifically with the mass of alginate, as shown in Table IV. The

presence of more gel in the sodium alginate/peroxidase mixture increases viscosity and leads to the formation of firmer beads, enhancing enzyme retention and reducing leakage into the surrounding medium. The optimum immobilization efficiency, reaching 76.59 %, is achieved at an AG-Na concentration of 1.5 %. The concentration of the enzyme to be immobilized significantly impacts enzyme retention and activity, with higher concentrations resulting in better retention but decreased enzymatic activity due to steric hindrance. An enzyme concentration of 1.3 U/mL is found to be optimal for good enzyme retention and maximal efficiency factor, as reported in Table IV. Calcium chloride serves as a gelling agent, and Table IV illustrates that the highest immobilization and efficiency factor of the ITP–Ca-AG are achieved at a concentration of 0.05 M $CaCl_2$. Using 1.5 % sodium alginate, an enzyme loading concentration of 1.3 U/mL, and a calcium chloride concentration of 0.05 M are the optimal conditions for entrapping peroxidase within calcium alginate beads, achieving the highest efficiency and retention rate. In contrast to the study of Gao *et al*., employing a higher sodium alginate and calcium chloride concentration of 2 % and 0.3 M, respectively, is aimed at reinforcing bead rigidity while maintaining diffusion efficiency.[41]

TABLE IV. Immobilization and factor efficiency (*IE*, η) of alginate beads obtained at different gelation conditions

Essay 1	Sodium alginate concentration, %; $[CaCl_2]$ = 0.1 M; [E] = 0.7 U/mL			
	1	1.5	2	2.5
IE / %	71.94	76.59	76.01	83.32
η / %	26.27	45.73	37.96	32.00
Essay 2	Enzyme loading, U/mL; [AG-Na] = 1.5 %; $[CaCl_2]$ = 0.05 M			
	0.7	1.0	1.3	1.8
IE / %	77.82	60.08	63.45	54.00
η / %	13.98	30.10	40.82	41.94
Essay 3	Chloride calcium dose, M; [AG-Na] = 1.5 %; [E] = 1.3 U/mL			
	0.05	0.1	0.15	0.2
IE / %	52.30	35.78	50.01	46.23
η / %	30.86	28.39	27.90	27.40

Morphology of ITP–Ca-AG beads

Alginate beads were observed using scanning electron microscopy (SEM). In Fig. 3, the distribution of peroxidase on the outer layer of the alginate bead can be seen, where the enzyme appears as multiple white dots. This can be confirmed after enlarging the image 160 times, where the presence of the enzyme is clear in the bead containing peroxidase, as illustrated in Fig. 3, compared to the empty bead.

Effect of pH

Fig. 4A illustrates the impact of pH on ITP–Ca-AG activity. The study investigates the degradation rates of AAP at various pH levels to identify the

most favorable conditions for maximum degradation efficiency. The optimal pH for this biodegradation process is determined to be 2, resulting in a 24 % biodegradation yield. Under neutral and basic pH conditions, the biodegradation efficiency is observed to be comparatively low. The immobilization of the enzyme in calcium alginate serves to stabilize it and potentially improve its catalytic performance, particularly in extreme pH environments.

(a1)   (b1)

(a2)   (b2)
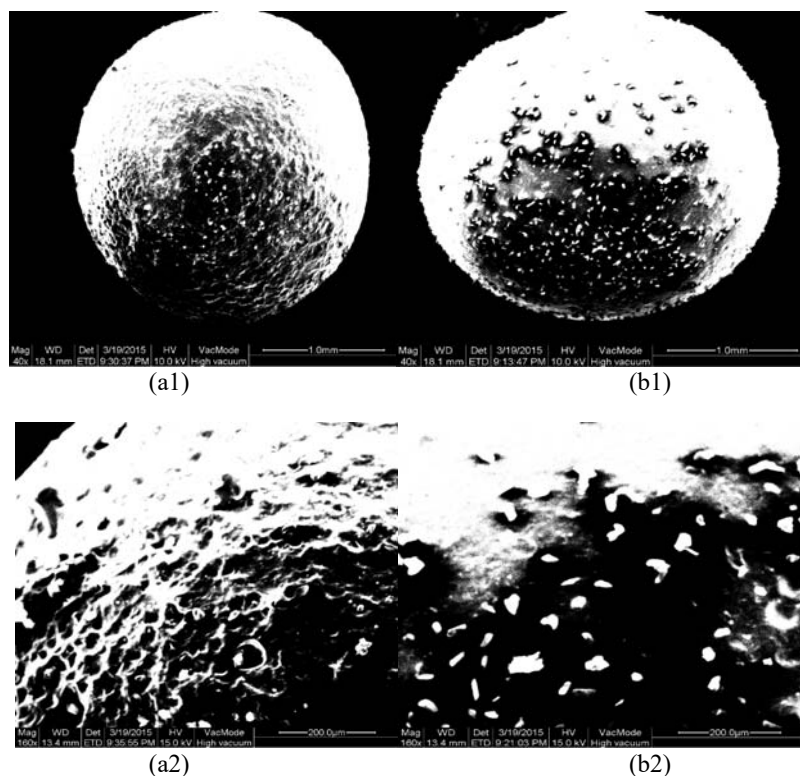
Fig. 3. SEM photographies of the outer layer of calcium alginate beads: a) without enzyme, b) with enzyme at different magnification (1, 40×, 2, 160×).

Effect of temperature

When peroxidase is immobilized in calcium alginate, its thermal stability is enhanced. The alginate matrix offers some protection against temperature-induced denaturation of the enzyme. The degradation of AAP by ITP–Ca-AG is affected by temperature, with a temperature range of 30 °C being optimal for maximum enzyme activity, as illustrated in Fig. 4B, both excessively high and low temperatures can have negative effects on the process, either by denaturing the enzyme or by slowing down the reaction rate. At temperatures beyond the optimal range (T_{opt}), the decomposition efficiency decreases to 23 % at 50 °C

and 20 % at 70 °C. For temperatures lower than the optimal range, the efficiency decreases by 17 %.
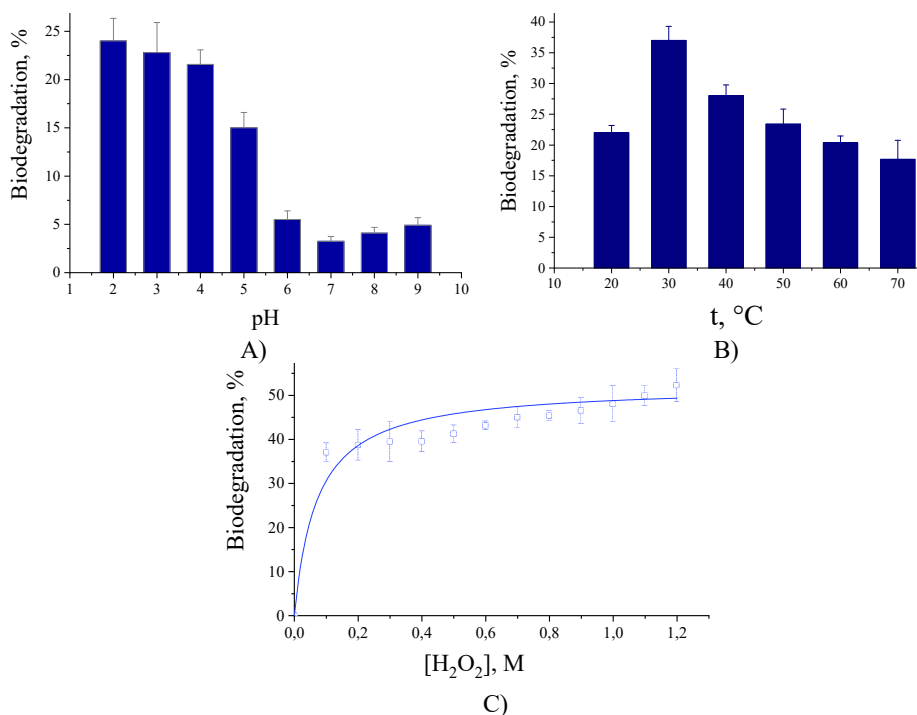
Fig. 4. Effect of: A) pH, B) temperature and C) H_2O_2 concentration on the degradation of AAP by ITP–Ca-AG.

Effect of hydrogen peroxide concentration

Fig. 4C demonstrates the impact of hydrogen peroxide on the degradation of AAP, revealing a notable increase in efficiency. With the increase in H_2O_2 concentration from 0.1 to 1.2 M, there is a substantial enhancement in the degradation yield, rising from 38 to 58 %. In the reaction, hydrogen peroxide functions as an electron acceptor, while peroxidase enzymes play a role in facilitating the transformation of AAP molecules into less harmful substances. Turnip peroxidase isoenzymes have demonstrated high thermostability and resistance to hydrogen peroxide inactivation compared to horseradish peroxidase, suggesting advantages in oxidative applications.[42] TP has also shown a great potential in degrading phenols, volatile organic compounds (VOCs) and dyes.[34,35,43]

Effect of AAP concentration

Fig. 5A illustrates that as the concentration of AAP increases, both the degradation and removal rate of AAP also increase. When the paracetamol dose was

(A)

$r^{-1} = 0.0356 + 0.0035 \cdot [AAP]^{-1}$
$R^2 = 0.95$

(B)
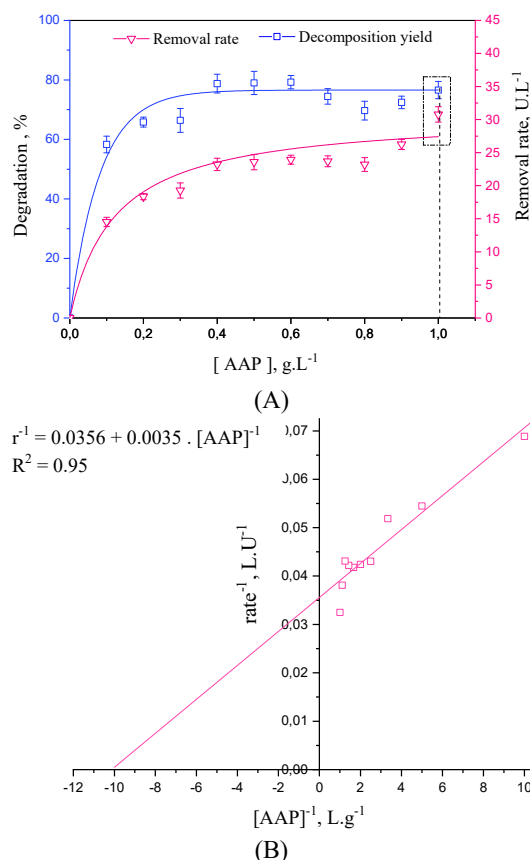
Fig. 5. Effect of: A) AAP concentration on the degradation yield and rate with ITP–Ca-AG and B) their double reciprocal plot or Lineweaver–Burk plot for the substrate paracetamol.

varied from 0.1 to 0.4 g/L, the decomposition yield, which represents the efficiency of the breakdown process, increased by 20 %. This indicates that the catalytic efficiency of turnip peroxidase increases when it is immobilized at higher concentrations of AAP, likely due to the enzyme having more substrate (AAP) available to interact with, thus increasing its catalytic activity. The results demonstrate that the maximum decomposition yield and removal rates were achieved for AAP concentrations as high as 1 g/L, suggesting that at this concentration, the enzyme operates at its peak efficiency. In Fig. 5B, the linearization of the Lineweaver–Burk plot, or the double reciprocal representation of velocity and AAP concentration, yields a straight line with a maximum velocity (r_{max}) of 28.1 U/L and a Michaelis–Menten constant (K_m) of 0.1 g/L.

Effect of beads quantity

From Fig. 6A, it was observed that the removal of AAP increased from 84 to 97 % as the mass of immobilized enzyme beads increased from 0.3 to 0.8 g. This indicates a positive correlation between the quantity of enzyme beads and the

efficiency of paracetamol degradation. At lower masses (0.3 g), the reaction is less efficient due to the limited availability of enzyme molecules to bind with paracetamol. Increasing the mass of enzyme beads is likely to increase the surface area available for the reaction, allowing more paracetamol molecules to interact with the enzyme simultaneously, resulting in higher degradation of AAP.

Effect of contact time under optimal conditions

Fig. 6B illustrates the impact of contact time on the decomposition of paracetamol under optimal conditions. In environmental settings, optimizing contact time is crucial for maximizing the efficiency of paracetamol decomposition processes. The kinetics of degradation yield by ITP–Ca-AG under optimal conditions demonstrates a gradual increase in paracetamol decomposition over time. After 10 min, 26 % of the drug is decomposed, and the yield reaches 97 % after 1 h. The initial slower rate of decomposition followed by accelerated degradation suggests that the enzymatic reaction proceeds more efficiently over longer periods, leading to a higher overall yield of paracetamol degradation.
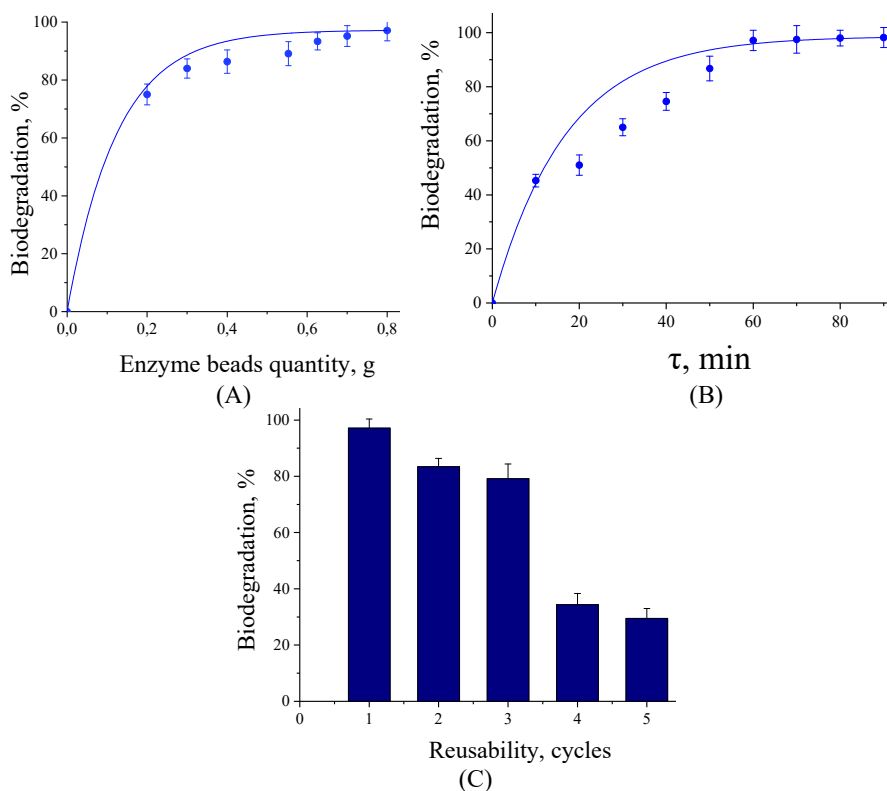
Fig. 6. AAP removal; A) effect of ITP–Ca-AG beads quantity, B) under optimal conditions and C) reuse cycles of immobilized enzyme.

Reuse of immobilized enzyme

When peroxidase enzyme is immobilized in calcium alginate, it is protected from denaturation and degradation, leading to a prolonged activity. The immobilized enzyme can be easily separated from the reaction mixture and reused, resulting in cost-effectiveness and reduced waste. In a study illustrated in Fig. 6C, it was observed that the activity of ITP–Ca-AG remained stable, with the degradation of paracetamol being maintained above 80 % up to the third batch, showing only a 20 % decrease compared to the first batch. Based on the results, it can be inferred that the immobilization process is effective, enabling the practical reuse of peroxidase for the degradation of pharmaceutical effluents. In the same study, paracetamol removal was achieved by combining the biocatalytic activity of horseradish peroxidase (HRP) with the adsorption capacity of a thermally cross-linked nanofibrous membrane, while the immobilized HRP showed a similar removal rate to the free enzyme (83.5 *vs.* 84.4 %).[27] Alternatively; in a separate work, paracetamol remained undegraded at pH 5 when using sol–gel encapsulated LiP- and HRP-based nanocomposites.[44] Whereas photocatalytic oxidation achieved 84.34 % degradation in over 1.5 h.[45] However, ITP–Ca-AG was able to degrade AAP to 99 % in less than 1 h. The study also included a comparison with previous research on the degradation of acetaminophen using various methods. It was noted that while photocatalytic oxidation, UV irradiation, and microbiological approaches can degrade AAP, they generally require a much longer time compared to enzymatic methods. The ITP–Ca-AG employed in the study demonstrated a significantly faster and more efficient degradation of AAP compared to the reported physical and microbiological methods. For instance, the yield of biological treatment of AAP by *Pseudomonas PrS10* strain isolated from pharmaceutical industrial effluents could reach 96.37 % within 7 days.[7] While photocatalytic oxidation gave 84.34 % degradation within 1.5 h,[45] whereas 97 % was obtained by ITP–Ca-AG after 60 min.

Despite its known catalytic properties, the application of turnip peroxidase (TP) in paracetamol degradation is less explored compared to HRP, presenting potential novelty due to its stability and efficiency in harsh conditions such as wastewater treatment. Turnip peroxidase (TP) has emerged as a promising biocatalyst for environmental remediation due to its oxidative capabilities and eco--friendly origin. Derived from a low-cost and readily available plant source, TP is an inexpensive and abundant enzymatic tool that can be readily exploited for the degradation of emerging pollutants, including pharmaceuticals, dyes and phenolic compounds. Its application in wastewater treatment offers a sustainable alternative to conventional chemical methods, particularly when immobilized or used in combination with hydrogen peroxide under mild conditions. The broad substrate specificity of TP, along with its potential for large-scale extraction from

agro-industrial waste, positions it as a viable candidate for green remediation technologies.

CONCLUSION

In conclusion, the breakdown of paracetamol utilizing partially purified turnip (*Brassica rapa*) peroxidase immobilized in calcium alginate beads under optimized conditions (1.3 U/mL enzyme loading, 1.5 % sodium alginate, and 0.05 M calcium chloride) with a maximum degradation yield of 97 % at pH 2.0 and 30 °C was achieved. The immobilized enzyme exhibited favorable kinetic parameters and maintained 80 % of its activity after three reuse cycles, indicating good stability and reusability. The findings suggest that the enzymatic mechanism was successful in breaking down pharmaceutical substances. While organic material was present at the end of the treatment, it was in a non-toxic and insoluble form. Future research could focus on scaling up the process, exploring degradation of other pharmaceutical contaminants and improving enzyme immobilization techniques to enhance stability and operational lifespan.

ИЗВОД

РАЗВОЈ ЕНЗИМА ИНКАПСУЛИРАНОГ У БИОПОЛИМЕРУ ЗА ЕФИКАСНУ РАЗГРАДЊУ АЦЕТАМИНОФЕНА

AHMEDI AFAF[1] и MAHMOUD ABOUSEOUD[2]

[1]*Laboratory of Biomaterials and Transfer Phenomena (LBMPT), Department of material Sciences, Faculty of Sciences, University Yahia Fares of Médéa, Médéa, Algeria и* [2]*Department of process and Environmental Engineering, Faculty of Technology, University Yahia Fares of Médéa, Médéa, Algeria*

У овој студији је испитивана ефикасност делимично пречишћене пероксидазе из репе (*Brassica rapa*) имобилизоване у калцијум алгинату, за разлагање парацетамола, познатог и као ацетаминофен (AAP), често коришћеног аналгетика и антипиретика који се набавља без рецепта. Инкапсулација пероксидазе је оптимизована у циљу минимизирања цурења ензима и задржавања максималне активности, подешавањем концентрације калцијум-алгината, полазне количине ензима и концентрације калцијум-хлорида. Оптимални услови инкапсулирања пероксидазе у калцијум-алгинатној матрици, са најповољнијим задржавањем и активношћу ензима су били: 1,3 U/mL почетна активност ензима, 1,5 % натријум-алгината и 0,05 M калцијум-хлорида. Фокус овог истраживања је био на испитивању ефикасности и могућности примене имобилизоване пероксидазе из репе у разлагању фармацеутских остатака, специфично циљајући парацетамол. Резултати су показали да је максимална разградња AAP на pH 2,0 и на температури од 30 °C, при концентрацији парацетамола и водоник пероксида од 1 g/L, односно 1,2 mol/L, дајући принос од 97 %. У студији су, такође, одређени кинетички параметри ензимске реакције, као што су максимална брзина и Микаелис–Ментенова (*Michaelis–Menten*) константа. Стабилизован ензим се може користити више пута, минимум три пута, задржавајући, у идеалним условима, 80 % своје способности да разгради AAP.

(Примљено 24. маја, ревидирано 14. јула, прихваћено 19. септембра 2025)

REFERENCES

1. B. R. Moss, *Ecology of Fresh Waters: Man and Medium, Past to Future*, John Wiley & Sons, New York, 2009
2. R. K. Mishra, S. S. Mentha, Y. Misra, N. Dwivedi, *Water-Energy Nexus* **6** (2023) 74 (https://doi.org/10.1016/j.wen.2023.08.002)
3. E. Tehrani, A. R. Faraji, N. Shojaei, S. Shahinmehr, A. Najafi, Z. Hekmatian, Z. Tehrani, B. Bornas, *J. Environ. Chem. Eng.* **11** (2023) 111575 (https://doi.org/10.1016/j.jece.2023.111575)
4. S. Wu, L. Zhang, J. Chen, *Appl. Microbiol. Biotechnol.* **96** (2012) 875 (https://doi.org/10.1007/s00253-012-4414-4)
5. M. Bagheri, H. Shekaari, M. Mokhtarpour, A. Alavi, S. Dorosti, M. Sillanpää, K. Nguyen, *J. Mol. Liq.* **406** (2024) 124999 (https://doi.org/10.1016/j.molliq.2024.124999)
6. A. H. Shah, M. A. Rather, *Environ. Sci. Pollut. Res.* **30** (2023) 93916 (https://doi.org/10.1007/s11356-023-28928-5)
7. K. Poddar, D. Sarkar, D. Chakraborty, P. B. Patil, S. Maity, A. Sarkar, *Int. Biodet. Biodeg.* **175** (2022) 105490 (https://doi.org/10.1016/j.ibiod.2022.105490)
8. A. A. Ignatiev, A. A. Gushchin, V. I. Grinevich, E. Yu. Kvitkova, A. A. Izvekova, V. V. Rybkin, *High Energy Chem.* **57** (2023) 522 (https://doi.org/10.1134/S0018143923060048)
9. S. S. Ayoub, *Temperature (Austin)* **8** (2021) 351 (https://doi.org/10.1080/23328940.2021.1886392)
10. H. I. Abdel-Shafy, M. S. Mohamed-Mansour, *Egypt. J. Chem.* **56** (2013) 449 (https://doi.org/10.21608/ejchem.2013.1123)
11. J. P. Fernandes, C. M. R. Almeida, M. A. Salgado, M. F. Carvalho, A. P. Mucha, *Toxics* **9** (2021) 257 (https://doi.org/10.3390/toxics9100257)
12. E. S. Massima Mouele, J. O. Tijani, K. O. Badmus, O. Pereao, O. Babajide, C. Zhang, T. Shao, E. Sosnin, V. Tarasenko, O. O. Fatoba, K. Laatikainen, L. F. Petrik, *Int. J. Environ. Res. Pub. Health* **18** (2021) 1683 (https://doi.org/10.3390/ijerph18041683)
13. S. C. Wiles, M. G. Bertram, J. M. Martin, H. Tan, T. K. Lehtonen, B. B. M. Wong, *Environ. Sci. Technol.* **54** (2020) 8072 (https://doi.org/10.1021/acs.est.0c01625)
14. C. Bührer, S. Endesfelder, T. Scheuer, T. Schmitz, *Int. J. Mol. Sci.* **22** (2021) 11156 (https://doi.org/10.3390/ijms222011156)
15. J. Gan, M. Bilal, X. Li, S. Z. Hussain Shah, B. A. Mohamed, T. Hadibarata, H. Cheng, *Chemosphere* **307** (2022) 136035 (https://doi.org/10.1016/j.chemosphere.2022.136035)
16. K. Jayalakshmi, A. B. Sangeetha, M. Sasikala, C. Selvi, M. Paramasivam, in *Environmental Contaminants. Impact, Assessment, and Remediation*, P. Ganguly, J. Mandal, M. Paramsivam, S. Patra, Eds., Apple Academic Press, Palm Bay, FL, 2024
17. M. D. G. de Luna, R. M. Briones, C.-C. Su, M.-C. Lu, *Chemosphere* **90** (2013) 1444 (https://doi.org/10.1016/j.chemosphere.2012.09.003)
18. T. Li, X. Gong, G. Yang, Q. Li, J. Huang, N. Zhou, X. Jia, *Bioprocess Biosys. Eng.* **45** (2022) 865 (https://doi.org/10.1007/s00449-022-02704-0)
19. C. Calas-Blanchard, G. Istamboulié, M. Bontoux, G. Plantard, V. Goetz, T. Noguer, *Chemosphere* **131** (2015) 124 (https://doi.org/10.1016/j.chemosphere.2015.03.019)
20. S. A. Snyder, S. Adham, A. M. Redding, F. S. Cannon, J. DeCarolis, J. Oppenheimer, E. C. Wert, Y. Yoon, *Desalination* **202** (2007) 156 (https://doi.org/10.1016/j.desal.2005.12.052)

21. R. Abejón, M. De Cazes, M. P. Belleville, J. Sanchez-Marcano, *Water Res.* **73** (2015) 118 (https://doi.org/10.1016/j.watres.2015.01.012)
22. H. Vishwakarma, S. Sharma, K. P. Panzade, P. S. Kharate, A. Kumar, N. Singh, H. Avashthi, P. Rangan, A. K. Singh, A. Singh, U. B. Angadi, K. H. M. Siddique, K. Singh, G. P. Singh, R. Pandey, R. Yadav, *Plant Stress* **11** (2024) 100367 (https://doi.org/10.1016/j.stress.2024.100367)
23. M. Bilal, J. Zdarta, T. Jesionowski, H. M. N. Iqbal, *Int. J. Biol. Macromol.* **234** (2023) 123531 (https://doi.org/10.1016/j.ijbiomac.2023.123531)
24. F. K. de Oliveira, L. O. Santos, J. G. Buffon, *Food Res. Int.* **143** (2021) 110266 (https://doi.org/10.1016/j.foodres.2021.110266)
25. A. Azizi, M. Abouseoud, A. Ahmedi, *J. Biochem. Technol.* **5** (2014) 795 (https://jbiochemtech.com/article/phenol-removal-by-soluble-and-alginate-entrapped-turnip-peroxidase)
26. D. Humer, O. Spadiut, *Monatsh. Chem.* **152** (2021) 1389 (https://doi.org/10.1007/s00706-021-02848-x)
27. R. Xu, Y. Si, F. Li, B. Zhang, *Environ. Sci. Pollut. Res. Int.* **22** (2015) 3838 (https://doi.org/10.1007/s11356-014-3658-1)
28. K. Ratanapongleka, S. Punbut, *Environ. Technol.* **39** (2018) 336 (https://doi.org/10.1080/09593330.2017.1301563)
29. F. Quintanilla-Guerrero, M. A. Duarte-Vázquez, R. Tinoco, M. Gómez-Suárez, B. E. García-Almendárez, R. Vazquez-Duhalt, C. Regalado, *J. Agric. Food Chem.* **56** (2008) 8058 (https://doi.org/10.1021/jf801400h)
30. J. Meena, A. Gupta, R. Ahuja, M. Singh, A. K. Panda, *J. Mol. Liq.* **338** (2021) 116602 (https://doi.org/10.1016/j.molliq.2021.116602)
31. J. Zdarta, T. Jesionowski, M. Pinelo, A. S. Meyer, H. M. N. Iqbal, M. Bilal, L. N. Nguyen, L. D. Nghiem, *Biores. Technol.* **344** (2022) 126201 (https://doi.org/10.1016/j.biortech.2021.126201)
32. F. L. C. Almeida, A. S. Prata, M. B. S. Forte, *Biofuels Bioprod. Bioref.* **16** (2022) 587 (https://doi.org/10.1002/bbb.2313)
33. M. Bilal, A. K. Singh, H. M. N. Iqbal, T. H. Kim, G. Boczkaj, K. Athmaneh, S. S. Ashraf, *Environ. Res.* **239** (2023) 117192 (https://doi.org/10.1016/j.envres.2023.117192)
34. A. Ahmedi, M. Abouseoud, A. Couvert, A. Amrane, *Zeitschrift Naturforsch., C* **67** (2012) 429 (https://doi.org/10.1515/znc-2012-7-811)
35. A. Ahmedi, M. Abouseoud, A. Abdeltif, C. Annabelle, *Enzyme Res.* **2015** (2015) 575618 (https://doi.org/10.1155/2015/575618)
36. A. Bhunia, S. Durani, P. P. Wangikar, *Biotechnol. Bioeng.* **72** (2001) 562 (https://doi.org/10.1002/1097-0290(20010305)72:5%3C562::AID-BIT1020%3E3.0.CO;2-S)
37. A. Azizi, L. Abouda, H. Cherifi, A. Krika, F. Krika, *Desalination Water Treat.* **265** (2022) 157 (https://doi.org/10.5004/dwt.2022.28626)
38. M. M. Bradford, *Anal. Biochem.* **72** (1976) 248 (https://doi.org/10.1016/0003-2697(76)90527-3)
39. H. N. Al-Mentafji, M. H. Al-Fahdawi, A. F. Al-farras, *Int. J. Drug Deliv. Technol.* **9** (2019) 689 (https://doi.org/10.25258/ijddt.9.4.30)
40. J. N. Ozioko, B. O. Ezema, K. O. Omeje, S. O. O. Eze, *J. Appl. Sci. Environ. Manage.* **25** (2021) 1163 (https://doi.org/10.4314/jasem.v25i7.9)

41. H. Gao, E. Khera, J.-K. Lee, F. Wen, *J. Vis. Exp.* (2016) 53944 (https://doi.org/10.3791/53944)
42. E. Agostini, J. Hernández-Ruiz, M. B. Arnao, S. R. Milrad, H. A. Tigier, M. Acosta, *Biotechnol. Appl. Biochem.* **35** (2002) 1 (https://doi.org/10.1042/ba20010049)
43. N. Tandjaoui, M. Abouseoud, A. Couvert, A. Amrane, A. Tassist, *Chemosphere* **148** (2016) 55 (https://doi.org/10.1016/j.chemosphere.2016.01.021)
44. I. V. Pylypchuk, G. Daniel, V. G. Kessler, G. A. Seisenbaeva, *Nanomaterials* **10** (2020) 282 (https://doi.org/10.3390/nano10020282)
45. A. Irshad, M. H. H. Mahmoud, Usman, R. Umer, M. Naeem, I. H. El Azab, Z. M. El-Bahy, *Desalination Water Treat.* **319** (2024) 100415 (https://doi.org/10.1016/j.dwt.2024.100415).

A novel Zn(II) coordination compound exhibits selective and sensitive detection of Fe^{3+} and acetylacetone

RUI DAI[1,2], YUETONG WANG[1], HUA ZHANG[1] and ZHIGUO KONG[1,2]*

[1]Department of Chemistry, Jilin Normal University, Siping 136000, China and [2]Key Laboratory of Preparation and Applications of Environmental Friendly Materials, Jilin Normal University, Ministry of Education, Changchun 130103, China

Abstract: Pyridine derivatives have strong coordination ability, tunable electronic, optical properties and excellent stability as ligands. Their substituent engineering and conjugation extension provides an ideal platform for the construction of efficient fluorescent probes, catalysts and biological functional materials. Based on this, a new coordination compound [Zn(phen)(L)(H$_2$O)]·4H$_2$O was synthesized under solvothermal conditions used 1,10-phenanthroline (phen), 3-carboxy-1-carboxymethyl-2-oxidopyridinium (H$_2$L) and Zn(II). The crystal structure and composition of the coordination compound were confirmed by single crystal X-ray diffraction and thermogravimetric analysis. Structural analysis confirmed by single crystal X-ray diffraction reveals its unique coordination geometry. In addition, it exhibits significant luminescence, making it a candidate for sensing applications. The luminescence and sensing properties of the coordination compound were investigated in detail. The K_{sv} values for the detection of Fe^{3+} and acac were found to be 3.29×10^5 and 6.67×10^5 M^{-1}, which confirmed high and efficient sensing ability of the synthesized sensor.

Keywords: zinc(II); coordination compound; solvothermal reaction; X-ray crystallography; fluorescence sensing.

INTRODUCTION

Acetylacetone (acac) is an organic coordination compound belonging to the *β*-diketone class, known for its excellent coordination ability and volatility. It is widely used in metal organic synthesis, catalyst preparation, and drug chemistry. However, its safety issues during actual use are increasingly receiving attention.[1] Studies show that acute exposure to acetylacetone through respiratory or skin contact can cause significant harm to the human body: its vapor has irritant effects on mucous membranes and respiratory tracts, and long-term exposure may lead to

---

1303

liver and kidney dysfunction.[2] Additionally, the environmental persistence of this substance should not be overlooked, its hydrophilicity also makes it easy to diffuse with water flow, pollute groundwater sources, destroy the integrity of aquatic biological cell membranes, inhibit algae photosynthesis and cause fish gill tissue damage.[3]

In addition, as an important representative of transition metal ions, Fe^{3+} has multiple functions in nature and industry, covering biological metabolism, catalytic reaction and environmental remediation.[4,5] However, ecological studies have shown that Fe^{3+} has significant toxicity to aquatic organisms.[6] Under occupational exposure scenarios, long-term inhalation of Fe^{3+} containing dust may cause pulmonary fibrosis, and the high solubility of Fe^{3+} in acidic environment will further enhance its bioavailability.[7] Besides, Fe^{3+} easily forms complexes with organic matter such as humic acid in soil and can enhance migration ability, destroy microbial community balance and threaten ecosystem stability.[8] In addition, excess iron ions in the body may cause various hazards, such as kidney failure, neurological disorders and certain types of cancer. Excessive iron can also cause health risks such as organ damage, increased risk of infection and digestive problems. Therefore, it is necessary to find a quick and efficient method for detecting Fe^{3+}, which has attracted increasing attention in environmental and medical fields.[9]

As a transition metal, Zn(II) is particularly suitable for the preparation of photoluminescent complexes because of their zero crystal field stability and their unique d^{10} configuration, which makes them absent from the potential quenching process caused by the d–d transition.[10–12] Zn is an essential trace element for human body, its complex easily metabolize under physiological conditions[13] and its cytotoxicity is significantly lower than that of heavy metal complexes (such as Cd^{2+} and Hg^{2+}).[14,15] Zn-based MOF fluorescent probes are gaining popularity for their high sensitivity, selectivity and stability.[16,17]

In this paper, a coordination compound $[Zn(phen)(L)(H_2O)]\cdot4H_2O$ was synthesized by solvothermal reaction using transition metal Zn (II), 1,10-phenanthroline (phen) and 3-carboxy-1-carboxymethyl-2-oxidopyridinium (H_2L) as raw materials. Detailed studies on its luminescent and sensing performance have found that it has good luminescent sensing performance for Fe^{3+} and acac which gives it significant application potential, such as the detection of Fe^{3+} and acac in water samples, the detection of Fe^{3+} in drugs, the detection of acac residue in chemical plants, *etc*.

EXPERIMENTAL

Materials and methods

All chemicals used for syntheses and characterization were reagent-grade and used as received from commercial sources, without further purification. PXRD were carried out on a Bruker – AXS Smart CCD X-ray diffractometer. Fluorescence experiments were carried out on

the RF-6000 fluorescence spectrophotometer. Thermogravimetric analysis (TGA) was performed on a NETZSCH STA 449F3 thermal analyzer.

Synthesis of [Zn(phen)(L)(H₂O)]·4H₂O

A mixture of $ZnSO_4$ (0.0288 g, 0.1 mmol), H_2L (0.0112 g, 0.06 mmol), phen (0.0186 g, 0.1 mmol), H_2O (2.5 ml) and DMF (2.5 ml) were sealed in a glass vial. After heating to 88 °C and maintaining the temperature for 72 h, heating was stopped to obtain colorless transparent rectangular-shaped crystals after cooling at a rate of 5° C per hour. Yield: 0.0221 g (41 %) based on Zn. Anal. (%); Calcd. for $C_{20}H_{23}N_3O_{10}Zn$: C, 45.26; H, 4.37; N, 7.92; Found %: C, 44.80; H, 4.32; N, 7.82.

X-ray crystallography

At 298(2)K, a Rigaku Raxis-Rapid diffractometer equipped with a graphite monochromator (MoKα radiation, λ = 0.71073 Å) was used to X-ray diffractometer analyze the single crystal, SIR2014 was used to solve the structure by direct method, and SHELXL2018/3 was used to optimize the F^2 by the full matrix least squares method.

A crystal of suitable size was selected by using an optical microscope, and the crystal size was determined to be 0.232 mm×0.211 mm×0.191 mm, and single crystal diffraction data were collected at a temperature environment around 25 °C. References were analyzed and refined.[18,19] Hydrogen atoms participate in final structure refinement (N–H, 0.86 Å, C–H, 0.93 Å), $Uiso$(H) = 1.2 Ueq. The final R = 0.0477, wR = 0.1162. (w = 1/[$s2(Fo2)$ + (0.0568P)2 + 0.7642P], P = ($Fo2$ + 2$Fc2$)/3), S = 1.045. The crystallographic summary of [Zn(phen)(L)(H₂O)]·4H₂O (1) is shown in Table I, bond lengths and bond angles in Table II and hydrogen bonds in Table III.

TABLE I. Crystal data, data collection and refinement details

Chemical formula	$C_{20}H_{23}N_3O_{10}Zn$
Formula weight	530.78
Temperature	298(2) K
Wavelength	0.71073 Å
Crystal system	triclinic
Space group	$P\bar{1}$
a / Å	9.134(3)
b / Å	10.539(4)
c / Å	12.228(4)
α / °	77.003(6)
β / °	77.770(6)
γ / °	85.245(6)
V / Å³	1120.2(7)
Z	2
Density (calculated)	1.574 mg/m³
F(000)	548
Final R indices (I > 2$sigma$(I))	$R1$ = 0.0477, $wR2$ = 0.1162
S	1.045
Absorption coefficient	1.158 mm⁻¹
Crystal size	0.232 mm×0.211 mm×0.191 mm
Absorption correction	Semi-empirical from 14 ≤ l ≤ 14
Max. and min. transmission	0.809 and 0.775

TABLE I. Continued

Index ranges	$-10 \leq h \leq 9,\ -12 \leq k \leq 9,\ 14 \leq l \leq 14$
Independent reflections	3847 (R(int) = 0.0263)
Reflections collected	5718
Refinement method	Full-matrix least-squares on F^2
Data/restraints/parameters	3847 / 0 / 307
Goodness-of-fit on F^2	1.003
Final R indices ($I > 2sigma(I)$)	$R1$ = 0.0477, $wR2$ = 0.1162
Final R indexes (all data)	$R1$ = 0.0606, w$R2$ = 0.1281
$\Delta\rho_{max}$, $\Delta\rho_{min}$, e Å^{-3}	0.512 / –0.505
Flack parameter	n/a

The crystallographic data were deposited with the Cambridge Crystallographic Data Centre (CCDC no. 2453636). Copies of this information can be obtained free of charge at: www.ccdc.cam.ac.uk or from the CCDC, 12 union Road, Cambridge CB2 1EZ, UK (fax: 0044 1223 336 033; e-mail: deposit@ccdc.cam.ac.uk).

TABLE II. Selected bond lengths and bond angles

Bond	Distance, Å	Bond	Distance, Å
N(2)–Zn(1)	2.117(3)	O(3)–Zn(1)	2.044(2)
N(3)–Zn(1)	2.092(3)	O(4)–Zn(1)	1.981(3)
O(1W)–Zn(1)	2.005(3)		
Bonds	**Angle, °**	**Bonds**	**Angle, °**
O(4)–Zn(1)–O(3)	87.46(10)	O(4)–Zn(1)–N(2)	87.62(12)
O(1W)–Zn(1)–O(3)	104.26(11)	O(1W)–Zn(1)–N(2)	104.33(11)
O(4)–Zn(1)–N(3)	154.63(13)	O(3)–Zn(1)–N(2)	151.35(11)
O(1W)–Zn(1)–N(3)	100.64(11)	N(3)–Zn(1)–N(2)	79.49(13)
O(3)–Zn(1)–N(3)	93.44(11)		

TABLE III. Geometrical parameters for intermolecular interactions; symmetry transformations used to generate equivalent atoms: [i]–x+1, –y, –z+1; [ii]x, y–1, z; [iii]–x+1, –y, –z; [iv]–x, –y+1, –z+1; [v]–x+1, –y+1, –z+1; [vi]x, y+1, z+1; [vii]x, y+1, z

D–H⋯A	d(D–H) / Å	d(H⋯A) / Å	d(D⋯A) / Å	∠DHA, °
O(1W)–H(1A)⋯O(5W)[ii]	0.85	1.77	2.567(4)	156.6
O(1W)–H(1B)⋯O(5)[iii]	0.85	1.80	2.640(4)	169.2
O(2W)–H(2A)⋯O(2)	0.85	2.01	2.798(5)	154.0
O(2W)H(2B)⋯O(2W)[iv]	0.85	2.24	2.813(7)	124.7
O(3W)–H(3A)⋯O(4W)[v]	0.85	1.94	2.759(5)	162.7
O(4W)–H(4A)⋯O(1)[i]	0.86	2.10	2.891(4)	152.6
O(4W)–H(4B)⋯O(5)[vi]	0.85	2.11	2.858(4)	147.8
O(5W)–H(5A)⋯O(2)[iv]	0.85	1.88	2.705(4)	162.4
O(5W)–H(5B)⋯O(1)[vii]	0.86	2.13	2.760(4)	129.7

Fluorescence sensing experiments

The following procedure was carried out: 3 mg of the coordination compound was dissolved in 9 mL of water, subjected to ultrasonic treatment, and then allowed to stand at room temperature for three days. The supernatant was then collected for fluorescence testing.[20]

<div align="center">RESULTS AND DISCUSSION</div>

Crystal structure description

Single crystal X-ray diffraction structure analysis indicates that the coordination compound belongs to the triclinic crystal system with the space group $P\bar{1}$: the key the structure data are presented in Table I. The asymmetric unit is composed of a crystallographically independent Zn^{2+}, one L ligand, one phen ligand, one coordination water molecule and four free water molecules. The Zn^{2+} in complex is five-coordinated. The Zn^{2+} is attached to two oxygen atoms (O3, O4), two nitrogen atoms (N2, N3), and one coordinated water molecule (O1) from three different ligands (Fig. 1) in a twisted triangular bipyramid configuration. The geometry of the coordination environment is nearly regular square-pyramidal, with a geometric distortion index of $\tau_5 = 0.05$.
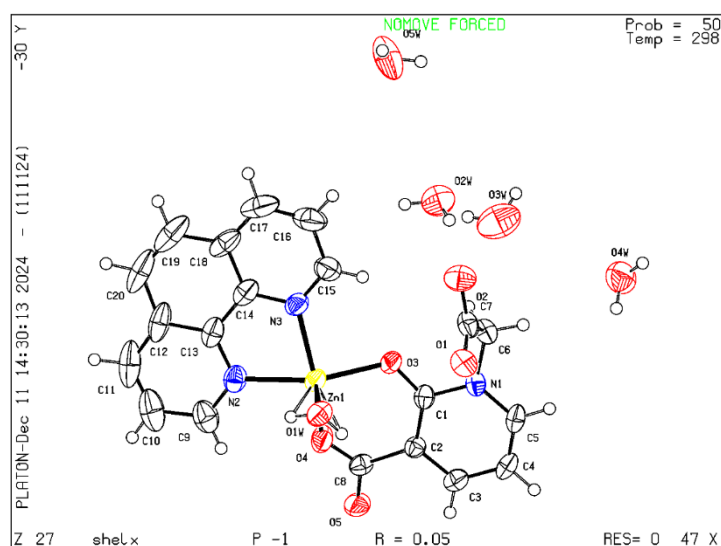
Fig. 1. Coordination environment of Zn^{2+} in the coordination compound. Displacement ellipsoids are drawn at the 50 % probability level and H atoms have been omitted for clarity.

The 1D chain is formed by the π–π interaction (Fig. 2a) between the pyridine ring (N1,C1) and the phenanthroline ring (N(2)[viii]/N(3)[viii]/C(9)[viii]–C(20)[viii] (symmetry codes: [viii]$x+1, y, z$)) of the adjacent unit. The shortest distances from the centroid to the centroid and from the centroid to the plane of the two rings are 3.693(2) and 3.4238(15) Å, respectively, and the dihedral angle between the two planes is 6.56(15)°. The 1D chain structure connects another adjacent 1D chain structure by hydrogen bonds (Table III) to form 1D double chains (Fig. 2b).[21] Eventually, the 1D double chains structure stacks up into a 3D network structure *via* hydrogen bonds (Fig. 3).[22]
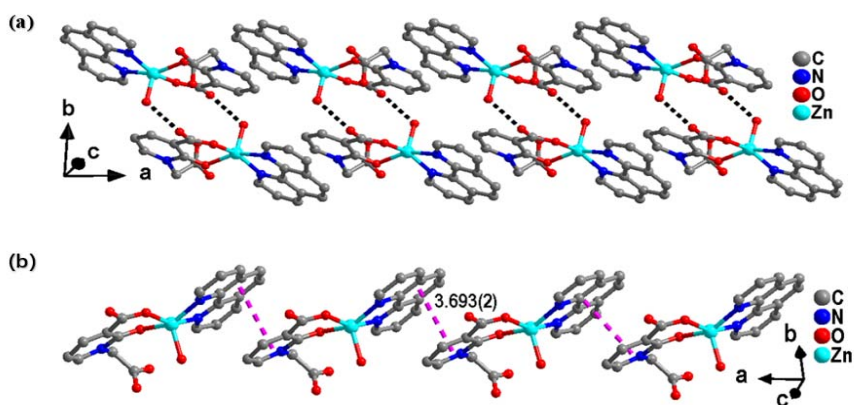
Fig. 2. a) 1D chain structure is formed by π–π interaction. b) 1D double chain structure formed by hydrogen bonding.
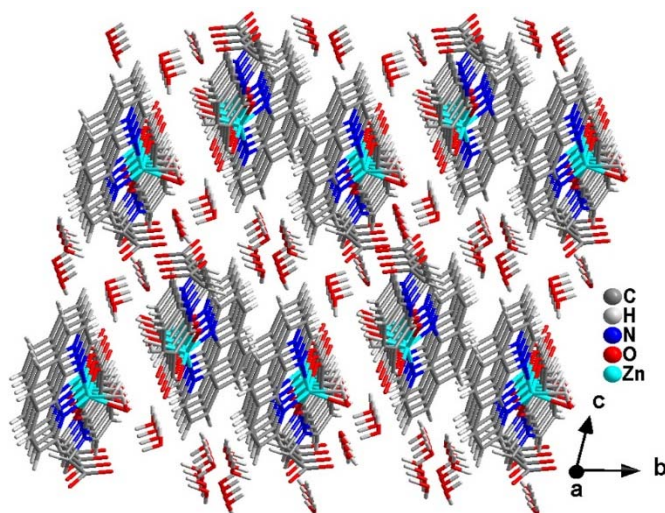
Fig.3.The 3D network structure.

PXRD analyses

In order to test the phase purity of the coordination compound, the powder X-ray diffraction analysis was carried out using Bruker-AXS Smart CCD X-ray diffractometer. The experimental result (Fig. 4) shows that the experimental peak value of the coordination compound is consistent with the one simulated by single crystal X-ray diffraction, which indicates that the good phase purity of the coordination compound, a certain degree of preferred orientation of crystallites is observed, as evidenced by the increase in intensity of discrete peaks with rising 2θ values.
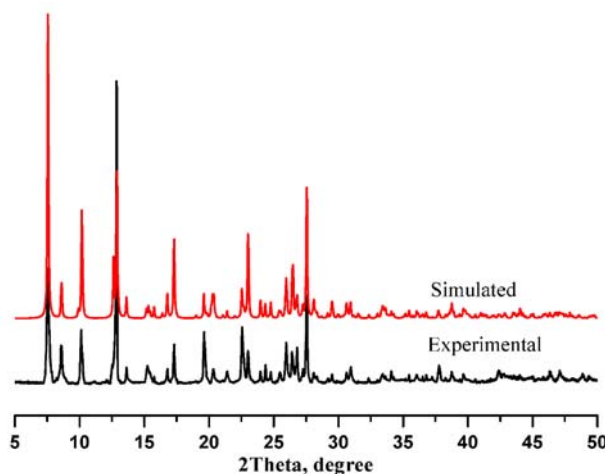
Fig. 4. PXRD patterns of the coordination compound.

TGA analysis of the coordination compound

Analysis shows (Fig. 5) that there is a slight increase in the coordination compound weight near 50°, which can be attributed to carbon dioxide and water molecules in the air. When the temperature rises to 150°, the weight of the coordination compound decreases by about 3.4 %. This is because the departure of unstable coordinated water molecules in the complex molecular framework, followed by a relatively gradual decrease of about 10 % in the coordination compound weight until the temperature rises to 270°, which is due to evaporation of four free water molecules within the complex molecular framework. The result is higher than actual, possibly due to incomplete drying of the sample, followed by a sharp decrease in the coordination compound weight immediately before the temperature rises to 420°. This remarkable decrease is related to the thermal decomposition of phen ligand and organic group $C_8H_5NO_5$ of L. At 453°, the ligand has not completely decomposed, and the weight of the coordination compound continues to decrease at a relatively smooth rate after heating, but the decomposition rate is slower. The above TGA results show that the coordination compound is unstable when heated, the whole framework is gradually collapsing and the results are basically consistent with the crystal structure.[24]

Photoluminescence properties

The fluorescence spectra of phen, H_2L and the coordination compound were investigated in the solid state (Fig. 6a). As shown, the coordination compound in solid state displays good emission characteristics at 366 nm (λ_{ex} = 250 nm), whereas ligands show emission with fluorescence peaks at 363 and 380 nm for phen (λ_{ex} = 280 nm) and 387 nm for H_2L (λ_{ex} = 325 nm). It is obvious that the

peak positions of the coordination compound and phen are very close. Which is attributed not only to the coordination between metal centers and ligands, but also to the superposition of the two luminous peaks of the phen ligand.
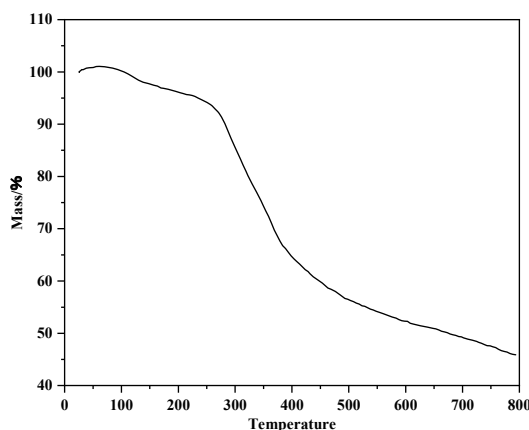
Fig. 5. The TGA of the coordination compound.

The liquid fluorescence of the coordination compound was also examined (Fig. 6b). When prepared as a 3mg/9ml solution, it has a sharp excitation peak at 363nm. Therefore, it can be seen that water has almost no effect on its luminescence, so water was chosen as the solvent for subsequent tests.
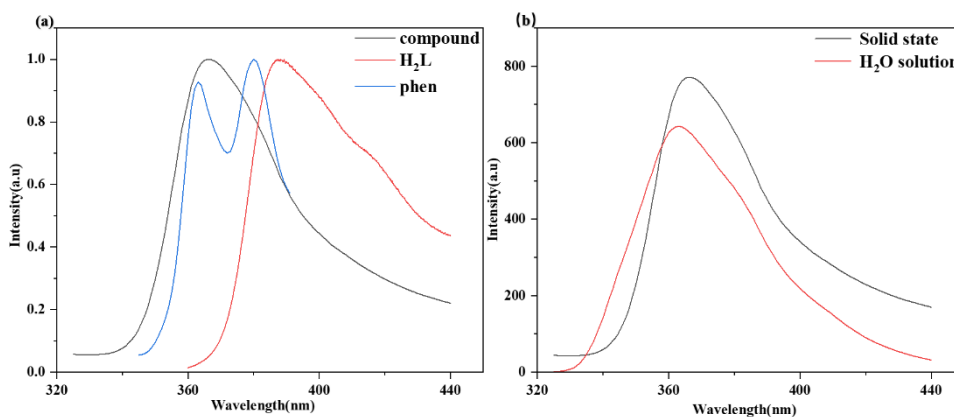
Fig. 6. a) Solid-state emission spectra of the coordination compound, phen and H$_2$L. λ_{ex}: 250 nm for the coordination compound, 248 nm for phen, and 325 nm for H$_2$L; b) the emission spectra of the coordination compound in solid state and H$_2$O solution. λ_{ex}: 250 nm for the coordination compound.

Fluorescence detection of the coordination compound for different cations

14 different metal chloride salts M(Cl)$_x$ (M=Mg^{2+}, Ba^{2+}, Ca^{2+}, Cd^{2+}, K$^+$, Ni^{2+}, Zn^{2+}, Cr^{3+}, Co^{2+}, Mn^{2+}, Nd^{3+}, Cu^{2+}, Na$^+$ and Fe^{3+}) with a concentration of

0.01 mol/L were prepared and used for fluorescence sensing testing. The results showed that the addition of different cationic solutions had different effects on the fluorescence intensity of the coordination compound. In particular, the addition of Fe^{3+} significantly reduced the fluorescence intensity of coordination compound (Fig. 7a). To reveal the effect of Fe^{3+} concentration on the fluorescence intensity of the coordination compound composites, the concentration--dependent change in the luminescence intensity of the coordination compound in solution was detected. As shown in Fig. 7b, with the increase of Fe^{3+} concentration from 0 to 3.8×10^{-4} M, the quenching effect of fluorescence in the suspension can be clearly observed. When the concentration of Fe^{3+} is 3.8×10^{-4} M, the luminescence of the suspension is almost completely quenched, and this phenomenon can be easily observed with the naked eye under a portable ultraviolet lamp (excitation wavelength of 254 nm) (Fig. 7b, inset). The linear relationship is good in the range of 2.5×10^{-5} to 3.8×10^{-4} M, with an R^2 value of 0.98634 (Fig. 7c). In addition, the selectivity of coordination compound for Fe^{3+} is performed by an anti-interference experiment, showing that the presence of other cations does not affect the detection of Fe^{3+} (Fig. 7d). According to the Stern–Volmer equation: $(I_0/I)-1 = K_{sv}[C]$ (I_0 represents the initial fluorescence intensity of the coordination compound without the addition of Fe^{3+}, I represents the fluorescence intensity of the coordination compound after the addition of Fe^{3+}, [C] represents the concentration of Fe^{3+} solution and K_{sv} is the fluorescence quenching constant M^{-1}). *LOD* is determined by the formula $LOD = 3\sigma/K_{sv}$, (σ is the relative standard deviation of the blank solution). Finally, luminescent titration demonstrates the *LOD* of 5.25×10^{-5} M for Fe^{3+}.

Fluorescence detection of the coordination compound for different organic reagents

Based on the excellent luminescent properties of the coordination compound, fluorescence spectroscopic studies were conducted on eight organic reagents including methanol (MeOH), ethanol (EtOH), acetonitrile (MeAN), isopropanol (IPA), acetone (ACE), *N,N*-dimethylformamide (DMF), *N,N*-dimethylacetamide (DMA) and acetylacetone (acac). The results showed that the fluorescence intensity of the coordination compound decreased significantly with the addition of various organic reagents, especially acac (Fig. 8a). To further explore the relationship between the concentration of acac and the fluorescence intensity of the coordination compound, a quantitative experiment was performed. The fluorescence quenching effect of the suspension can be clearly observed with the acac concentration increases from 0 to 8.2×10^{-4} M. When the concentration of acac is 2.5 µM, the luminescence of the suspension almost completely disappears (Fig. 8b). The linear relationship is good in the range of 0.15 to 0.51 mM, with an R^2 value of 0.99837 (Fig. 8c). In addition, the selectivity of the coordination com-
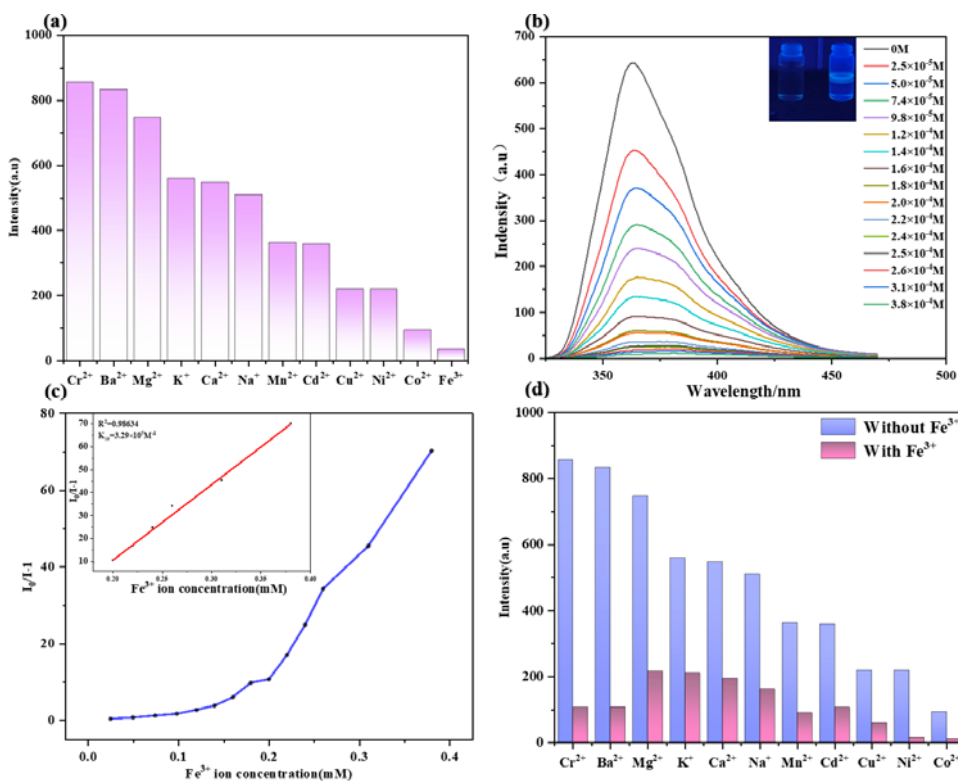
Fig. 7. a) The influence of fluorescence intensity of the coordination compound in the presence of various cationic solutions; b) fluorescence spectra of the coordination compound in aqueous solution with different concentrations of Fe^{3+}; c) fluorescence Stern–Volmer (S–V) equation and the linear relationship of (I_0/I)–1 with Fe^{3+} concentration; d) competitive experiments of the coordination compound in sensing Fe^{3+} with the interference of other metal ions.

pound for acac is performed by an anti-interference experiment, showing that the presence of other cations does not affect the detection of acac (Fig. 8d). Finally, to further evaluate the effect of luminescent titration, the *LOD* was calculated to be 3.4×10^{-5} M by formula $3\sigma/K_{SV}$, verifying the sensitivity of the coordination compound to the detection of acac.

CONCLUSION

In this paper, a new coordination compound was synthesized successfully by solvothermal reaction with Zn^{2+}, 1,10-phenanthroline and 3-carboxy-1-carboxymethyl-2-oxidopyridinium as raw materials and characterized by single crystal X-ray diffraction, TG and PXRD. Single crystal X-ray diffraction shows that the coordination compound further forms 1D by π–π interactions, then 1D layered structure is formed through hydrogen bonds, and 3D supramolecular structure is further accumulated. The experimental results of powder XRD show that the lig-
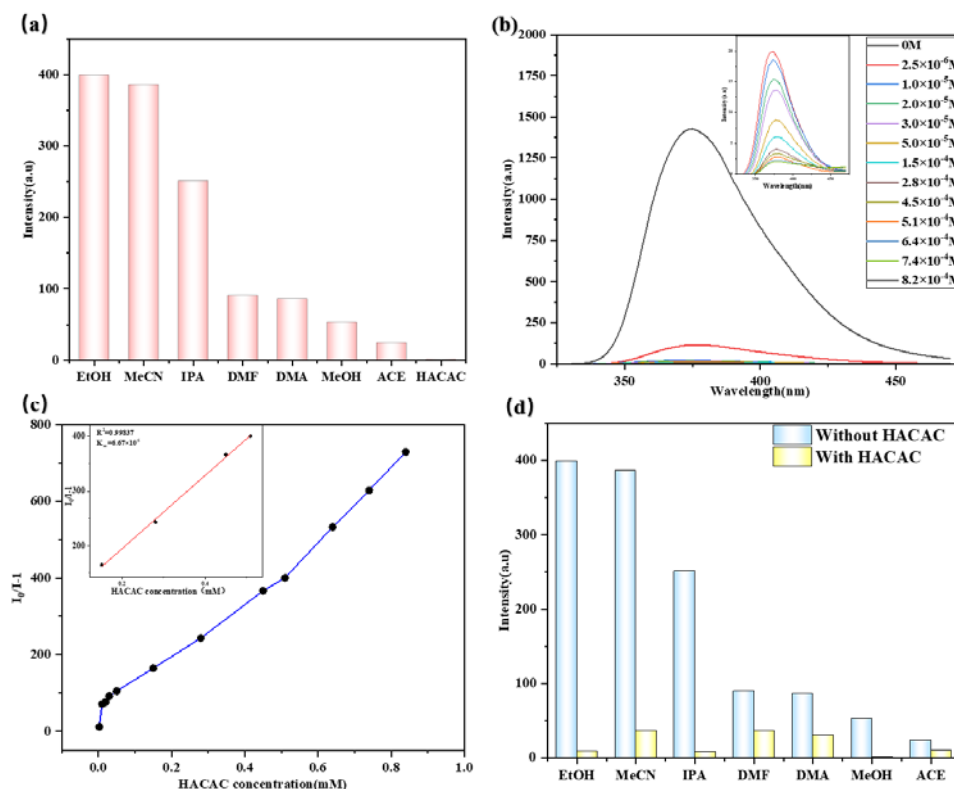
Fig. 8. a) The influence of fluorescence intensity of the coordination compound in the presence of various organic reagents; b) fluorescence spectra of the coordination compound in aqueous solution with different concentrations of acac; c) fluorescence Stern–Volmer (S–V) equation and the linear relationship of (I_0/I)–1 with acac concentration; d) comparison of the luminescence intensity of the coordination compound in the presence of acac- mixed organic reagents.

and has been successfully coordinated. The thermogravimetric test results show that it has thermal stability at a certain temperature.

The results of fluorescence sensing experiments show that the coordination compound have good luminescence sensing properties for Fe^{3+} and acac, with minimum *LOD* values of 5.25×10^{-5} M and 3.4×10^{-5} M. Further research will include the luminescence mechanism and practical applications, and it is expected that will have better prospects for use in the future.

И З В О Д

НОВИ ЦИНК(II) КОМПЛЕКС ЗА СЕЛЕКТИВНУ И ОСЕТЉИВУ ДЕТЕКЦИЈУ Fe^{3+} И АЦЕТИЛАЦЕТОНА

RUI DAI[1,2], YUETONG WANG[1], HUA ZHANG[1] и ZHIGUO KONG[1,2]

^{1}Department of Chemistry, Jilin Normal University, Siping 136000, China и ^{2}Key Laboratory of Preparation and Applications of Environmental Friendly Materials, Jilin Normal University, Ministry of Education, Changchun 130103, China

Деривати пиридина имају изражену способност координације, флексибилне електронске и оптичке особине, као и значајну стабилност као лиганди. Њихова супституциона модификација и проширена конјугација пружају идеалну платформу за изградњу ефикасних флуоресцентних сонди, катализатора и биолошки функционалних материјала. Имајући то у виду, синтетисан је нови $[Zn(phen)(L)(H_2O)]\cdot4H_2O$ комплекс у солвотермалним условима, користећи 1,10-фенантролин (phen), 3-карбокси-1-карбоксиметил-2-оксидопиридинијум (H_2L) и Zn(II). Кристална структура и састав координационог једињења потврђени су методом дифракције X-зрака са монокристала и термогравиметријском анализом. Структурна анализа синтетисаног једињења је потврдила његову јединствену координациону геометрију. Поред тога, једињење испољава значајну луминисценцију, што га чини кандидатом за примену у сензорима. Луминисцентне и сензорске особине синтетисаног координационог једињења детаљно су испитиване. Нађено је да вредности K_{sv} константе за детекцију Fe^{3+} и ацетилацетона (acac) износе $3,29\times10^5$ M^{-1} и $6,67\times10^5$ M^{-1}, што потврђује високу и ефикасну способност детекције синтетисаног сензора.

(Примљено 2. јуна, ревидирано 1. јула, прихваћено 15. септембра 2025)

REFERENCES

1. M. S. Wang, X. T. Liu, B. C. Pan, S. J. Zhang, *Chemosphere* **93** (2013) 2877 (https://doi.org/10.1016/j.chemosphere.2013.08.082)
2. S. Yao, H. Xu, T. Zheng, Y. Li, H. Huang, J. Wang, J. Chen, S. Liu, H. Wen, *Chin. Chem. Lett*. **34.4** (2023) 107532 https://doi.org/10.1016/j.cclet.2022.05.046
3. Y. N. Wang, H. Xu, S. D. Wang, R. Y. Mao, L. M. Wen, S. Y. Wang, L. J. Liu, Y. Sun, S. Q. Liu, F. Wang, Q. F. Yang, *Spectrochim. Acta, A* **286** (2023) 121952 (https://doi.org/10.1016/j.saa.2022.121952)
4. X. Zhang, X. Zhuang, N. Zhang, C. Ge, X. Luo, J. Li, J. Wu, Q. Yang, R. Liu, *CrystEngComm* **21** (2019) 1948 (https://doi.org/10.1039/c9ce00068b)
5. W. Liu, H. Cui, J. Zhou, X. Chen, H. Yang, J. Wang, *J. Mol. Struct.* **1302** (2024) 137468 (https://doi.org/10.1016/j.molstruc.2023.137468)
6. L. L. Liu, H. W. Zhang, J. Y. Ren, L. Wang, Y. Zhang, *Spectrochim. Acta, A* **331** (2025) 125762 (https://doi.org/10.1016/j.saa.2025.125762)
7. Z. ul Nisa, M. Ahmad, H. N. Sheikh, *New J. Chem*. **48** (2024) 3100 (https://doi.org/10.1039/D3NJ05433K)
8. B. Zhao, J. Lu, H. Liu, S. Li, Q. Sun, B. Zhang, *CrystEngComm* **26** (2024) 1319 (https://doi.org/10.1039/D3CE01174G)
9. Á. González-Domínguez, F. M. Visiedo-García, J. Domínguez-Riscart, R. González--Domínguez, R. M. Mateos, A. M. Lechuga-Sancho, *Int. J. Mol. Sci*. **21** (2020) 5529 (https://doi.org/10.3390/ijms21155529)

10. J. B. Araškov, A. Višnjevac, J. Popović, V. Blagojević, H. S. Fernandes, S. F. Sousa, I. Novaković, J. M. Padrón, B. B. Holló, M. Monge, M. Rodríguez-Castill, *CrystEngComm* **24.29** (2022) 5194 (https://doi.org/10.1039/D2CE00443G)
11. C. Bizzarri, E. Spuling, D. M. Knoll, D. Volz, S. Bräse, *Coord. Chem. Rev*. **373** (2018) 49 (https://doi.org/10.1016/j.ccr.2017.09.011)
12. P. Ristić, T. R. Todorovic, V. Blagojević, O. R. Klisuric, I. Marjanovic, B. B. Holló, P. Vulic, M. Gulea, M. Donnard, M. Monge, M. Rodríguez-Castillo, *Cryst. Growth Des.* **20** (2020) 4461 (https://doi.org/10.1021/acs.cgd.0c00287)
13. R. A. Khan, A. AlFawaz, I. Hasan, N. A. AlMuryyi, A. A. Alhamed, S. Laeeq, A. Alsalme, *New J. Chem*. **48** (2024) 1287 (https://doi.org/10.1039/D3NJ04709A)
14. J. Suebphanpho, J. Boonmak, *RSC Adv.* **14** (2024) 9781 (https://doi.org/10.1039/D4RA00500G)
15. G.M. Otero-Fuentes, V. Sánchez-Mendieta, A. Sánchez-Ruiz, R. A. Morales-Luckie, D. Martínez-Otero, J. Jaramillo-García, A. Dorazco-González, *J. Fluoresc.* **35** (2024) 3449 (https://doi.org/10.1007/s10895-024-03754-1)
16. K. X. Ma, Y. Y. Yuan, Y. T. Ren, Y. Yang, H. G. Hao, J. Lu, S. N. Wang, *ACS Appl. Nano Mater.* **7** (2024) 19448 (https://doi.org/10.1021/acsanm.4c03335)
17. M. T. Seuffert, A. E. Sedykh, T. C. Schäfer, J. Becker, K. Müller-Buschbaum, *Dalton Trans.* **54** (2025) 5075 (https://doi.org/10.1039/D4DT03149K)
18. M. C. Burla, R. Caliandro, B. Carrozzini, G. L. Cascarano, C. Cuocci, C. Giacovazzo, G. Polidori, *J. Appl. Crystallogr.* **48** (2025) 306 (https://doi.org/10.1107/S1600576715001132)
19. G. M. Sheldrick, *Cryst. Struct. Chem.* **71** (2015) 3 (https://dx.doi.org/10.1107/S2053229614024218)
20. W. Liu, H. Cui, J. Zhou, X. Chen, H. Yang, J. Wang, *J. Mol. Struct*. **1302** (2024) 137468 (https://doi.org/10.1016/j.molstruc.2023.137468)
21. H. Wang, S. Li, H. Zhang, B. Su, X. Wang, *Main Group Met. Chem*. **48** (2025) 20240029 (https://doi.org/10.1515/mgmc-2024-0029)
22. X. Li, Y. Huang, B. Liu, X. Wang, *Main Group Met. Chem.* **48** (2025) 20240013 (https://doi.org/10.1515/mgmc-2024-0013)
23. Y. Hanifehpour, B. Mirtamizdoust, J. Dadashi, R. Wang, M. Rezaei, M. Abdolmaleki, S. W. Joo, *Crystals* **12** (2022) 113 (https://doi.org/10.3390/cryst12010113)
24. L. Gao, C. Jiao, H. Chai, Y. Ren, G. Zhang, H. Yu, L. Tang, 284 (2020) 121199, *J. Solid State Chem*. **284** (2020) 121199 (https://doi.org/10.1016/j.jssc.2020.121199).

Computational insights into the inhibitory potential of dihydroorotate dehydrogenase by natural compounds in *Artocarpus champeden* as antimalarial agents

PUTRA JIWAMURWA PAMA TJITDA[1]*, FEBRI ODEL NITBANI[2], TUTIK DWI WAHYUNINGSIH[3], YOHANES MAU ABANIT[1] and FAIZAL RIZA SOEHARTO[1]

[1]Department of Pharmacy, Health Polytechnic of Kupang, Indonesia, [2]Department of Chemistry, Faculty of Science and Engineering, Nusa Cendana University, Indonesia and [3]Department of Chemistry, Faculty of Mathematics and Natural Sciences, Universitas Gadjah Mada, Indonesia

Abstract: *Plasmodium falciparum* dihydroorotate dehydrogenase (*Pf*DHODH) is a crucial target for the development of antimalarial drugs, as it plays a significant role in inhibiting the growth of parasites by disrupting the production of pyrimidines in the bloodstream. *Artocarpus champeden* is known to contain prenylated flavonoids with potential antimalarial activity. This study aims to explore the chemical interactions of active compounds found in *A. champeden* through an *in silico* approach. Nine compounds were docked into *Pf*DHODH (PDB ID: 6I55), and their stability was subsequently assessed using molecular dynamics simulations. Molecular docking results indicated that compounds **C1**, **C5** and **C6** emerged as the most promising candidates, exhibiting binding affinities of –37.80, –35.28 and –34.44 kJ/mol, respectively. His185 and Arg265 were found to be key binding residues, interacting with these compounds in a manner similar to DZB, the control ligand. A 50-ns molecular dynamics simulation further confirmed the stability of these compounds throughout the simulation. Moreover, the examination of hydrogen bond occupancy demonstrated that compound **C1** consistently engaged in hydrogen bonding interactions with His185 and Arg265 throughout the simulation.

Keywords: molecular docking; molecular dynamics; *Plasmodium falciparum*; malaria; natural product.

INTRODUCTION

Plasmodium falciparum (*Pf*) is a species of *Plasmodium* that significantly contributes to high malaria-related mortality.[1] Globally, the incidence of malaria remained relatively stable from 2020 to 2022, with a slight increase observed in

---

1317

2023, reaching from 5.86 to 60.4 cases per 1,000 population. The majority of these cases occur in Africa (89.7 %), with the highest numbers reported in Ethiopia (4.5 million cases), Madagascar (2.7 million), Pakistan (1.6 million), Nigeria (1.4 million) and the Republic of Congo (600,000 cases).[2] Concurrently, data from the World Health Organization (WHO) indicate that the Southeast Asian region accounts for approximately 4 million malaria cases, with India and Indonesia significantly contributing to malaria-related mortality and representing 88 % of total cases in the region. In Indonesia, national reports documented 73.5 thousand malaria cases, with approximately 20 deaths reported in 2025.[3]

The development and synthesis of 4-aminoquinoline analogs culminated in the identification of chloroquine as a first-line drug for malaria treatment.[4] Chloroquine had long been established as effective agent in malaria therapy. However, in the early 1960s, resistance to chloroquine was first documented in several malaria-endemic countries.[5] To address this issue, the WHO recommended the use of combination therapies with different mechanisms of action to suppress resistance rates. Artemisinin-based combination therapies (ACTs) demonstrated efficacy in mitigating and reducing malaria cases between 2000 and 2015.[6] Artemisinin and its derivatives – including artemether, artesunate and dihydro artemisinin (DHA) – are commonly combined with piperaquine, mefloquine or amodiaquine, as recommended by the WHO.[7] However, recent data indicate that resistance to ACTs has emerged in several regions of Southeast Asia, particularly in the Greater Mekong subregion.[8] The increasing resistance to existing treatments highlights the urgent need for the discovery and development of new antimalarial compounds.

Artocarpus champeden, known as Cempedak in Indonesia, has been scientifically validated to possess a diverse array of biological activities, including diuretic,[9] antifungal[10] and antidiabetic effects.[11] An *in vitro* study on the dichloromethane extract of its stem bark demonstrated significant antimalarial activity against the Pf 3D7 strain, with an IC_{50} value of 0.99 μg/mL.[12] The methanol extract of the stem bark exhibited the most potent antimalarial efficacy,[13] with IC_{50} values of 4.23 and 16.58 μg/mL against the 3D7 and G-2300 strains, respectively, after 48 h of incubation. Previous studies have explored the active compounds responsible for its antimalarial effects, identifying flavonoid derivatives as contributors to the inhibition of the *Pf* 3D7 strain, with IC_{50} values ranging from 0.001 to 75 μmol/L.[12,14] Heteroflavone C, a prenylated flavonoid, demonstrated potent activity (IC_{50} of 0.001 μmol/L) compared to artoindonesianin E. This non-prenylated flavonoid has an IC_{50} of 75 μmol/L. Despite several studies showing the antimalarial potential of *A. champeden*, the inhibitory mechanism of its active compounds remains inadequately understood. Therefore, comprehensive research is needed to elucidate the molecular mechanisms underlying its antimalarial activity.

The *de novo* biosynthesis of pyrimidine, a precursor for DNA and RNA synthesis, is critical for the survival of *Plasmodium*.[15] As a result, this pathway has emerged as a significant target in antimalarial drug development. Dihydroorotate dehydrogenase (DHODH) is an enzyme that catalyzes the oxidation of dihydroorotate (DHO) to orotate (ORO). Additionally, DHODH is located in the mitochondria, where it operates as part of the electron transport chain *via* cytochrome oxidase.[16] Atovaquone, a naphthoquinone derivative, has been scientifically proven to inhibit DHODH and is widely used as an antimalarial drug. However, its efficacy is constrained by issues of selectivity and specificity related to the lipophilic nature of the DHODH active site.[17] To improve its effectiveness, atovaquone is combined with proguanil, resulting in a synergistic antimalarial therapy.[18]

The presence of prenylated flavonoids in *A. champeden* suggests their potential as a DHODH inhibitor. The prenyl substituent on flavonoid compounds is thought to enhance their hydrophobic properties, thereby increasing interactions with the lipophilic binding site of DHODH. In this study, the potential of prenylated flavonoids in *A. champeden* was evaluated using an *in silico* approach. Molecular docking analysis was performed to assess the binding energy and chemical interactions between active compounds and the DHODH binding site. Furthermore, molecular dynamics simulations were conducted to evaluate the stability of the formed complexes and to identify the most suitable compounds based on prior analyses.

EXPERIMENTAL

Instrumentation

The computational analysis was conducted on a personal computer (PC) operating on Windows 10, equipped with an Intel Core i9-13900H processor. The software used in this study included ChemDraw Professional 16, Chem3D 16, AutoDock Vina with AutoDock tools, Open Babel, Discovery Studio Client 2021 (version 21.1.0.20298) and GROMACS.

Ligand preparation

The prenylated flavonoid compounds found in *Artocarpus champeden* was obtained from a previous study.[12] The 2D structure was drawn using ChemDraw Professional 16 and subsequently converted into a 3D structure using Chem3D 16. Geometry optimization was performed using the MM2 force field, with a minimum RMS gradient of 0.01. Following this optimization, the structure was saved in PDB format. For the preparation of the 3D structure, hydrogen atoms and Gasteiger charges were added using AutoDock Tools before saving it in PDBQT format.

Protein receptor preparation

The structure of *Plasmodium falciparum* dihydroorotate dehydrogenase (*Pf*DHODH) was used as the receptor and retrieved from the RCSB Protein Data Bank (PDB ID: 6I55). Water molecules and the native ligand were removed using Biovia Discovery Studio Client 2021, after which the structure was saved in PDB format. Subsequently, polar hydrogen atoms and Kollman charges were added to the receptor using AutoDock Tools (ADT). The prepared receptor was then saved in PDBQT format.

Molecular docking

Molecular docking is a computational method used to assess the binding energy and chemical interactions between a ligand and a protein receptor. Validating the docking protocol is a crucial step to ensure the reliability of the analysis of the tested compounds. This validation process was carried out by redocking the native ligand with the receptor, followed by superimposition to compare their conformations. The docking protocol is considered reliable if the *RMSD* value is below 2 Å.[19]

Molecular docking was performed at the binding site using a grid center located at (*x*, *y*, *z*) coordinates of 16.083, 22.654 and 35.024, respectively, with a box size of 18 Å in each dimension (*x*, *y*, *z*). After validating the docking protocol, the compounds being tested are docked onto the receptor using the predetermined grid center and box size. The lowest binding energy is indicative of a stable ligand-receptor complex. Additionally, the chemical interactions of the tested compounds are compared to those of the native ligand at the receptor's binding site.

Molecular dynamics

The molecular dynamics simulation was conducted on the three best compounds to evaluate their stability within the ligand-receptor complex. The simulation was performed using GROMACS 2023 software.[20] The protein topology was prepared using the General AMBER99SB force field,[21] while the acpype module with GAFF2 was used to generate the ligand topology.[22] The system was solvated in water molecules using the TIP3P model within a dodecahedron box.[23] To neutralize the system, sodium and chloride ions were added.

Energy minimization was carried out using the steepest descent method, followed by equilibration under NPT conditions for 1000 ps. Subsequently, the equilibrated system was further stabilized under NVT conditions at 300 K for the same duration. A 50-ns production simulation was then performed using the mdrun module. The simulation trajectory was analyzed and visualized using the mgrace package to evaluate *RMSD*, *RMSF*, radius of gyration (*Rg*), solvent-accessible surface area (*SASA*) and hydrogen bonding throughout the simulation.

RESULTS AND DISCUSSION

Molecular docking

Validating the docking protocol is a crucial step to ensure that the method yields valid and reliable data. The validation process involved redocking the DZB compound, which is the native ligand, into the receptor of *Pf*DHODH. The results of validation showed a low *RMSD* value of 0.46 Å, indicating the reliability of the docking procedure. The superimposition of the redocked ligand with the native ligand is presented in Fig. 1.
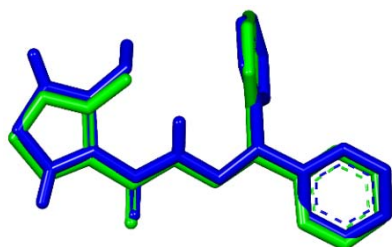
Fig. 1. Superimpose the re-docking ligand (green) onto the native ligand (blue).[24]

The DZB compound, acting as a native ligand, interacted with amino acids at the binding site of *Pf*DHODH (Fig. 2). The hydrophilic interaction of DZB within the binding site was facilitated by the hydroxyl group on the thiadiazole ring, which formed a hydrogen bond with His185. Additionally, the carbonyl group interacted with Arg265. Both of these amino acids are essential as catalytic residues in the oxidation reaction, converting flavin mononucleotide (FMN) to FMNH$_2$.[16] Moreover, the hydrophobic region of *Pf*DHODH, which includes Leu172, Cys175 and Phe188, interacted with the dibenzyl moiety of DZB through π–π stacking and π–alkyl interactions. The hydrophobic residues Cys184 and Val532 in *Pf*DHODH were also involved in interactions with the thiadiazole ring of DZB.
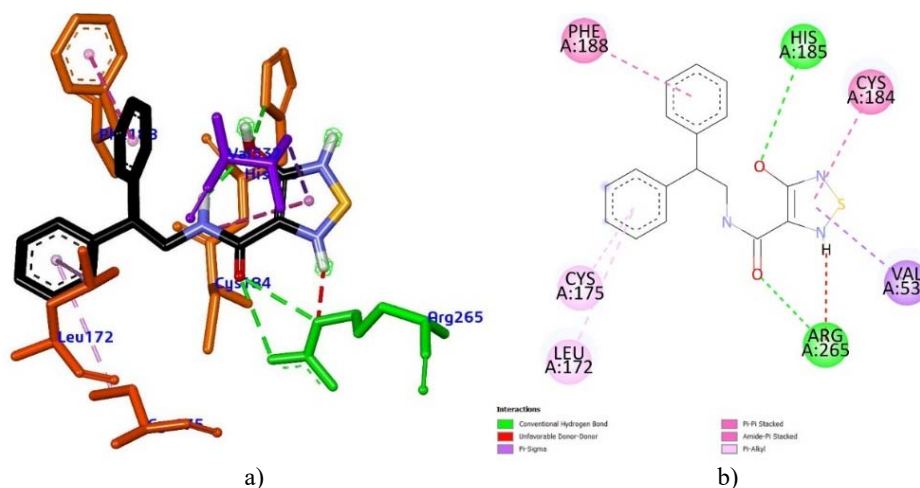
Fig. 2. Chemical interaction of DZB in the binding pocket of *Pf*DHODH (PDB ID: 6i55): a) 3D visualization and b) 2D visualization.

Nine prenylated flavonoid compounds from *Artocarpus champeden* were predicted to have antimalarial activity, particularly as inhibitors of *Pf*DHODH (Fig. 3). The molecular docking results for each compound are presented in Table I. The findings indicate that prenylated flavonoids effectively interact with *Pf*DHODH. Four compounds – **C1**, **C2**, **C5** and **C8** – demonstrated high binding affinities of –37.80, –35.28, –35.28 and –37.38 kJ/mol, respectively. These values indicate stronger interaction compared to that of DZB (–34.44 kJ/mol), suggesting enhanced binding strength. Among these four compounds, hydrophilic interactions with the catalytic residues His185 and Arg265 were observed in **C1**, **C5** and **C8**. These interactions are believed to contribute to their greater binding stability relative to DZB.

Compound **C2** has a binding energy similar to that of compound **C5**; however, it does not establish hydrophilic interactions with the catalytic residues His185 and

Arg265. The stability of the **C2**–*Pf*DHODH complex relies solely on hydrophobic interactions, particularly through π–sigma interactions with Leu172. Therefore, compounds **C1**, **C5** and **C8** were identified as potential inhibitors in this study. Chemical interactions are crucial in determining a compound's efficacy as an inhibitor. The chemical interactions of these three compounds are illustrated in Fig. 4. Compound **C1** exhibited a hydrogen bond interaction with Arg265 *via* the hydroxyl group substituted at the meta position of ring B of the flavonoid, with a binding distance of 2.81 Å, which is shorter than the interaction observed in the DZB compound. Additionally, hydrophobic interactions with residues Leu172, Cys175, Cys184 and Val532 were identified. Furthermore, the presence of a prenyl substituent on ring C of the flavonoid enhanced the π–sigma interactions with Phe188, contributing to increased complex stability.
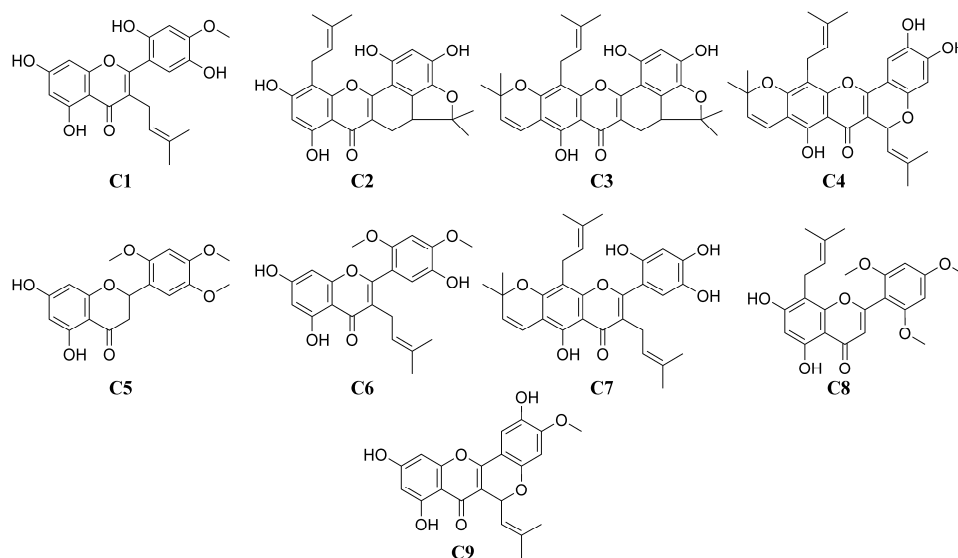
Fig. 3. Prenylated flavonoids in *Artocarpus champeden*.

Compound **C5** forms a hydrogen bond with His185 through a hydroxyl group attached to ring A of the flavonoid. Although the bond distance of 2.80 Å is slightly longer than the interaction observed in the DZB compound, this bond still contributes to the stability of the **C5** complex. Additionally, this stability is further reinforced by hydrophobic interactions between Leu172 and Cys175 with the methoxy group on ring B of the flavonoid. In contrast to compounds **C1** and **C8**, compound **C5** does not interact with Arg265, which explains its slightly lower binding energy compared to these two compounds. Furthermore, an analysis of the influence of the prenyl substituent revealed that compound **C5**, which lacks a prenyl group, was unable to form hydrophobic interactions with Phe188. This

absence of interaction contributes to the differences in complex stability when compared to compounds **C1** and **C8**.

TABLE I. Binding energy and interactions of prenylated flavonoid compounds

ID Compound (ID PubChem)	Binding energy kJ/mol	Interaction		
		Hydrogen bond	Distance, Å	Hydrophobic
DZB	–34.44	His185	2.76	Leu172, Cys175, Cys184, Phe188, Val532
		Arg265	4.39	
C1 (163106267)	–37.80	Tyr168	2.44	Leu172, Cys175, Cys184, Phe188, Phe227, Leu531, Val532, Met536
		His185	3.46	
		Arg265	2.81	
C2 (145950438)	–35.28	Tyr168	2.92	Leu172, Leu187, Leu191, Leu197, Pro198, Met536
		Cys175	3.31	
		Leu531	2.44	
		Gly535	2.55	
C3 (14557102)	–27.72	Val532	2.39	Leu172, Cys175 (pi-sulfur), Ile179, Ile183, Cys184, Phe188, Phe227, Met536 (pi-sulfur)
C4 (5316250)	–27.72	Cys175	4.00	Leu172, Ile179, Ile183, Leu187, Cys184 (pi-sulfur), Met536
C5 (nf)	–35.28	His185	2.80	Tyr168, Phe171, Leu172, Cys175, Cys184, Leu187, Val532, Met536
C6 (5320437)	–34.44	Tyr168	2.73	Leu172, Cys175, Cys184, His185, Phe188, Leu531, Val532, Met536
C7 (14557105)	–33.18			Phe171, Leu172, Cys175, Ile179, Cys184 (pi-sulfur), His185 (van der Waals), Leu187
C8 (not found)	–37.38	Tyr168	3.78	Leu172, Cys175, Cys184, Leu187, Phe188, Leu191, Phe227, Leu531, Val532, Met536
		His185	2.59	
		Arg265	2.72	
C9 (101415464)	–34.02	Cys175	3.31	Tyr168, Phe171, Leu172, Cys184 (pi-sulfur), Leu187, Leu191

Compound **C8** demonstrated an interaction pattern distinct from the previous compounds. While its binding energy is slightly lower than that of compound **C2**, its interaction pattern closely mimics that of the native ligand. The two hydroxyl groups on ring A of the flavonoid are crucial for forming hydrogen bonds with His185 and Arg265, with bond distances of 2.59 and 2.72 Å, respectively. These

distances are shorter than those observed in both DZB and compound **C2**, suggesting a stronger interaction with the active site of *Pf*DHODH.

a)

b)

c)
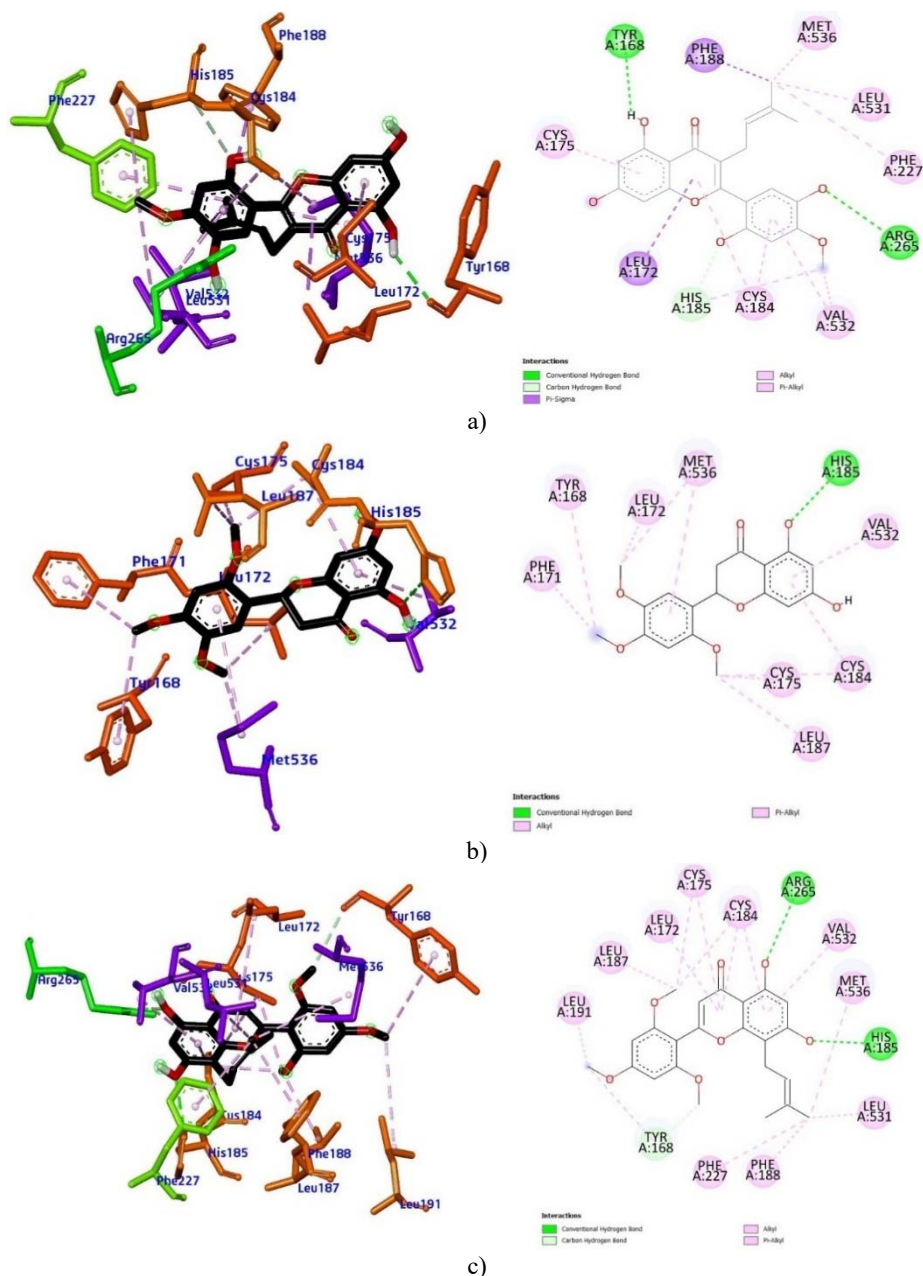
Fig. 4. The 3D and 2D visualization of chemical interaction for the three best compounds:
a) **C1**, b) **C5** and c) **C8**.

In addition to hydrophilic interactions, hydrophobic interactions also contribute to stabilizing the **C8**–*Pf*DHODH complex. The amino acid residues Leu172, Cys184 and Val532 participated in π–alkyl interactions, while Cys175 was further stabilized by alkyl interactions from the methoxy group attached on ring B of the flavonoid. Notably, the presence of a prenyl substituent enhanced additional hydrophobic interactions with Phe188 through alkyl interactions.

The molecular docking analysis of the three selected compounds emphasized the critical role of the prenyl substituent in enhancing hydrophobic interactions with the binding site of *Pf*DHODH. The absence of this substituent was associated with a decline in the binding affinity of the compound to the target protein. Although lower binding energy indicates greater stability of the complex, it is important to note that molecular docking is performed using a rigid protein structure, which necessitates further validation. Therefore, the stability of these complexes should be further analyzed through molecular dynamics simulation.

Molecular dynamics

The three most effective compounds identified through molecular docking were further evaluated for their complex stability using molecular dynamics simulation over a period of 50 ns. To assess the stability of the complexes, the root mean square deviation (*RMSD*) of the protein backbone throughout the simulation was analyzed, as shown in Fig. 5a. The mean *RMSD* values for the protein backbone in complexes **C1**, **C5** and **C8** were 0.132, 0.145 and 0.139 nm, respectively. These low *RMSD* values indicate that the conformational changes in the protein during the simulation, resulting from interactions with the ligand, were minimal.[24] Among the tested compounds, complex **C1** exhibited the highest stability, which is associated with its effective binding at the active site of *Pf*DHODH.

The stability of the tested compounds was also assessed by analyzing the *RMSD* of the ligand relative to the protein, with the results presented in Fig. 5b. All three compounds exhibited an initial increase in *RMSD* at 8 ns, reflecting the ligand adaptation process within the complex at the beginning of the simulation. Following this phase, the *RMSD* patterns for compounds **C1** and **C8** remained stable up to 25 ns, while compound **C5** maintained stability only during the first 10 ns. Throughout the remainder of the simulation, the *RMSD* values of all three compounds fluctuated but generally remained within a normal range, likely due to receptor flexibility. The mean *RMSD* values for the ligand within protein were 0.19, 0.27 and 0.28 nm for compounds **C1**, **C5** and **C8**, respectively. The lower *RMSD* value of compound **C1** indicates that it remained more stable within the binding pocket throughout the simulation.

The flexibility of amino acid residues due to interactions with the ligand was analyzed using the *RMSF* plot (Fig. 5c). Although the *RMSF* plot exhibited a fluc-
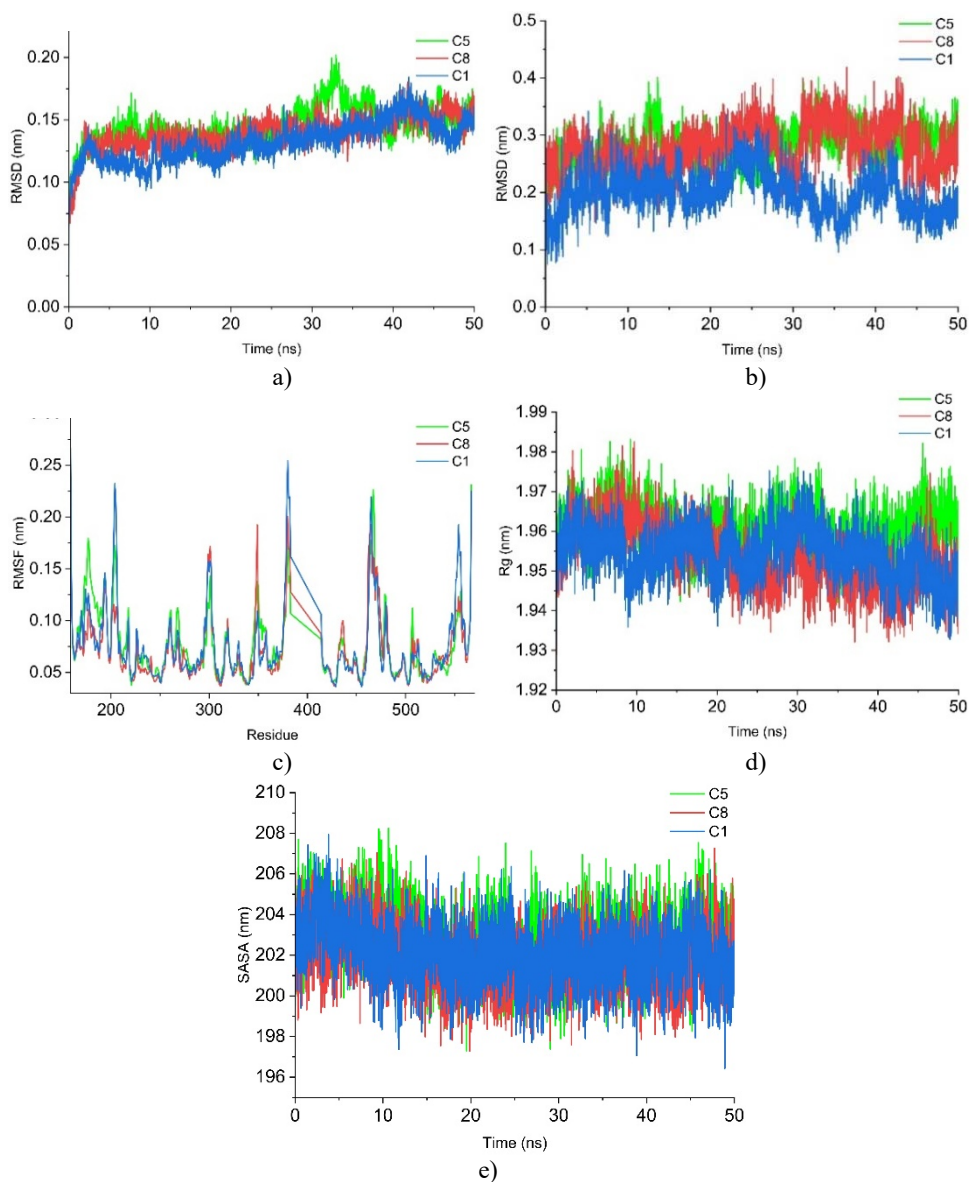
Fig. 5. Molecular dynamic results represented by: a) R*MSD* of the protein backbone,
b) *RMSD* of the ligand fit to protein, c) *RMSF*, d) radius of gyration and e) *SASA* plots.

tuating pattern, key residues such as His185, Phe188, Arg265 and Val532 had low
RMSF values. This indicates that their rigidity plays a significant role in
maintaining stable interactions with the tested compounds.[24,25] To further evaluate
the stability of the complex, we analyzed the compactness of the receptor, as shown

in Fig. 5d. Complex **C1** exhibited a stable trend up to 30 ns, followed by a decrease in the radius of gyration (*Rg*) value until the end of the simulation. This decline in *Rg* suggests a protein folding phenomenon,[25] which aids in the retention of the stability of the complex. The mean *Rg* values for complexes **C1** and **C8** were 1.95 nm, while complex **C5** exhibited a slightly higher *Rg* value of 1.96 nm.

The interaction between the receptor and surrounding water molecules plays a crucial role in stabilizing the complex. This analysis is presented in the *SASA* plot (Fig. 5e). Generally, the *SASA* values for the three complexes show an initial increase during the first 5 ns, which indicates the initial interaction between the solvent and the receptor surface. Afterward, the *SASA* values decrease up to 15 ns, at which point they stabilize for the remainder of the simulation. These stable *SASA* values suggest that the tested compounds have improved access to the receptor's binding site.[26] Additionally, a high number of hydrogen bond interactions between the tested compounds and the binding site during the simulation contributes to maintaining the stability of the complex.[27] However, the mean number of hydrogen bonds for compound **C5** is only one throughout the simulation (Fig. 6). Analysis of hydrogen bond occupancy revealed that compound **C5** formed hydrogen bonds with Arg265 (0.22 %) and Cys175 (0.32 %), Table II, which are the lowest percentages among the tested compounds.
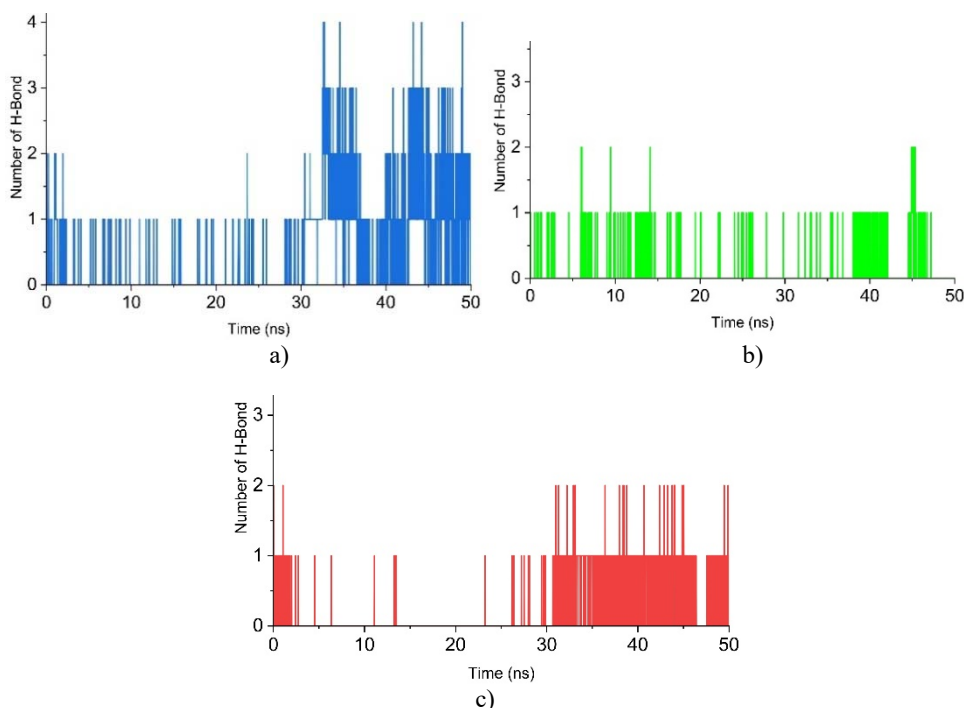
Fig. 6. Number of hydrogen bonds detected in the receptor with: a) **C1**, b) **C5** and c) **C8**.

TABLE II. Hydrogen bond occupancy of prenylated flavonoid compounds

Compound	Donor	Acceptor	Occupancy, %
C1	C1 568-Side	CYS184-Main	0.12
	C1 568-Side	VAL532-Main	0.14
	C1 568-Side	CYS175-Main	1.14
	C1 568-Side	HIS185-Side	5.14
	C1 568-Side	GLY181-Main	0.06
	ARG265-Side	C1 568-Side	4.28
	C1 568-Side	LEU187-Main	0.44
C5	ARG265-Side	C5 568-Side	0.22
	C5 568-Side	GLY181-Main	0.16
	C5 568-Side	CYS175-Main	0.32
C8	C8 568-Side	HIS185-Side	0.12
	C8 568-Side	GLY181-Main	0.30
	ARG265-Side	C8 568-Side	3.12

Compound **C8** temporarily lost its hydrogen bond from 5 ns to 30 ns during the simulation, but it re-established a hydrogen bond, averaging one bond during the final 20 ns. Hydrogen bond occupancy analysis revealed that compound **C8** acted as a hydrogen donor to Arg265 with an occupancy of 3.12 % and as a hydrogen acceptor to Cys185 with an occupancy of 0.12 %. In contrast, compound **C1** consistently maintained hydrogen bond interactions throughout the simulation. Notably, it exhibited an increase in the mean number of hydrogen bonds, rising to three from 35 ns until the end of the simulation. Compound **C1** demonstrated strong interactions both within the binding site and the hydrophobic region through hydrogen bonding. The interactions with Arg265 and His185 had hydrogen bond occupancies of 4.28 and 5.14 %, respectively, which were the highest values among the tested compounds. These findings indicate that compound **C1** exhibits optimal interaction stability with the *Pf*DHODH receptor compared to compounds **C5** and **C8**.

CONCLUSION

The evaluation of nine active compounds from *Artocarpus champeden* as potential *Pf*DHODH inhibitors identified compound **C1** as the most promising candidate. Compound **C1** demonstrated the highest binding energy of –37.8 kJ/mol, indicating a stable interaction with the receptor's binding site. This finding is consistent with molecular dynamics simulations over 50 ns, where the **C1** complex remained stable based on *RMSD* ligand fit protein analysis and sustained hydrogen bond interactions throughout the simulation. Therefore, compound **C1** is recommended for isolation and further validation of its antimalarial activity through *in vitro* assays in a wet laboratory.

ИЗВОД

КОМПЈУТЕРСКО ПРОУЧАВАЊЕ ИНХИБИТОРНОГ ПОТЕНЦИЈАЛА ДИХИДРООРОТАТ-ДЕХИДРОГЕНАЗЕ ПРИРОДНИМ ЈЕДИЊЕЊИМА ИЗ *Artocarpus champeden* У СВОЈСТВУ АНТИМАЛАРИЈСКИХ АГЕНАСА

PUTRA JIWAMURWA PAMA TJITDA[1], FEBRI ODEL NITBANI[2], TUTIK DWI WAHYUNINGSIH[3], YOHANES MAU ABANIT и FAIZAL RIZA SOEHARTO[1]

[1]*Department of Pharmacy, Health Polytechnic of Kupang, Indonesia, [2]Department of Chemistry, Faculty of Science and Engineering, Nusa Cendana University, Indonesia u [3]Department of Chemistry, Faculty of Mathematics and Natural Sciences, Universitas Gadjah Mada, Indonesia*

Диходрооротат-дехидрогеназа из *Plasmodium falciparum* (*Pf*DHODH) је кључна мета у развоју антималаријских лекова, јер има важну улогу у инхибирању раста паразита, ометајући стварање пиримидина у циркулацији. *Artocarpus champeden* садржи пренило-ване флавоноиде са потенцијалном антималаријском активношћу. У овој студији су ис-питане хемијске интеракције активних једињења *A. champeden* применом *in silico* методе. Интеракција девет једињења са *Pf*DHODH (PDB ID: 6I55) је проучавана и њихова стабил-ност испитана применом молекулских динамичких симулација. Молекулско моделовање је указало да су једињења **C1**, **C5** и C6 обећавајући кандидати, са афинитетом везивања од −37,80, −35,28, односно −34,44 kJ/mol. His185 и Arg265 су кључни везујући остаци који интерагују са испитаним једињима на сличан начин као контролни лиганд DZB. 50-ns молекулска динамичка симулација је потврдила стабилност ових једињења. Такође, испитивање интеракције водоника кроз симулације је показало да су у једињењу **C1** присутне водоничне везе са His185 и Arg265.

(Примљено 27. маја, ревидирано 9. јула, прихваћено 31. јула 2025)

REFERENCES

1. T. Abdul-Rahman, O. A. Ajetunmobi, G. B. Bamigbade, I. Ayesiga, M. H. Shah, T. S. Rumide, A. B. Adesina, G. A. Adeshina, O. E. Oni, B. I. N. Christian, A. T. Aborode, A. A. Wireko, H. I. Thaalibi, I. M. Abdalla, S. B. Banimusa, J. N. Jonathan, I. A. Onifade, M. A. Haque, *Int. J. Equity Health* **24** (2025) 22 (https://doi.org/10.1186/s12939-025-02378-6)
2. WHO, *World malaria report 2024*, 2024
3. Kasus Malaria di Indonesia, *Kementerian Kesehatan RI*, https://malaria.kemkes.go.id/case (accessed: March 5, 2025)
4. A. R. Parhizgar, A. Tahghighi, *Iran. J. Med. Sci.* **42** (2017) 115 (https://pmc.ncbi.nlm.nih.gov/articles/PMC5366359/)
5. K. Pal, M. K. Raza, J. Legac, M. A. Rahman, S. Manzoor, P. J. Rosenthal, N. Hoda, *RSC Med. Chem.* **12** (2021) 970 (https://doi.org/10.1039/D1MD00038A)
6. M. Thellier, A. A. J. Gemegah, I. Tantaoui, *J. Clin. Med.* **13** (2024) 1 (https://doi.org/10.3390/JCM13195680)
7. R. W. van der Pluijm, C. Amaratunga, M. Dhorda, A. M. Dondorp, *Trends Parasitol.* **37** (2021) 15 (https://doi.org/10.1016/j.pt.2020.09.011)
8. M. Ouji, J. M. Augereau, L. Paloque, F. Benoit-Vical, *Parasite* **25** (2018) 1 (https://doi.org/10.1051/PARASITE/2018021)
9. Fitrya, A. Amriani, R. P. Novita, R. Gabriella, S. V. Lestari, A. Agustina, *J. Ayurveda Integr. Med.* **14** (2023) 1 (https://doi.org/10.1016/J.JAIM.2023.100746)

10. Q. F. Hu, S. Yao, Y. Y. Ma, R. F. Xiong, G. H. Kong, Y. P. Wu, G. K. Zhao, M. Dong, W. G. Wang, M. Zhou, Y. K. Li, *Chem. Biol. Technol. Agric.* **10** (2023) 94 (https://doi.org/10.1186/s40538-023-00457-w)

11. S. Supandi, M. S. Wulandari, E. Samsul, A. Azminah, R. Y. Purwoko, H. Herman, H. Kuncoro, A. Ibrahim, N. S. S. Ambarwati, R. Rosmalena, R. N. Azizah, S. Paramita, I. Ahmad, *J. Adv. Pharm. Technol. Res.* **13** (2022) 207 (https://doi.org/10.4103/JAPTR.JAPTR_376_22)

12. A. Widyawaruyanti, Subehan, S. K. Kalauni, S. Awale, M. Nindatu, N. C. Zaini, D. Syafruddin, P. B. S. Asih, Y. Tezuka, S. Kadota, *J. Nat. Med.* **61** (2007) 410 (https://doi.org/10.1007/s11418-007-0153-8)

13. M. M. Taek, *MoluccaMedica* **4** (2011) 37 (https://ejournal.unpatti.ac.id/ppr_iteminfo_lnk.php?id=571) *in Indonesian*

14. T. S. Wahyuni, W. Ekasari, A. Widyawaruyanti, Y. Hirasawa, H. Morita, N. C. Zaini, *Heterocycles* **79** (2009) 1121 (https://doi.org/10.3987/COM-08-S(D)72)

15. S. R. Krungkrai, J. Krungkrai, *Asian Pac. J. Trop. Med.* **9** (2016) 525 (https://doi.org/10.1016/J.APJTM.2016.04.012)

16. L. V. Hoelz, F. A. Calil, M. C. Nonato, L. C. Pinheiro, N. Boechat, *Future Med. Chem.* **10** (2018) 1853 (https://doi.org/10.4155/fmc-2017-0250)

17. C. D. Goodman, J. E. Siregar, V. Mollard, J. Vega-Rodríguez, D. Syafruddin, H. Matsuoka, M. Matsuzaki, T. Toyama, A. Sturm, A. Cozijnsen, M. Jacobs-Lorena, K. Kita, S. Marzuki, G. I. McFadden, *Science* **352** (2016) 349 (https://doi.org/10.1126/science.aad9279)

18. A. Blanshard, P. Hine, *Cochrane Database Syst. Rev.* **1** (2021) 1465 (https://doi.org/10.1002/14651858.cd004529.pub3)

19. P. H. M. Torres, A. C. R. Sodero, P. Jofily, F. P. Silva-Jr, *Int. J. Mol. Sci.* **20** (2019) 4574 (https://doi.org/10.3390/ijms20184574)

20. D. Van Der Spoel, E. Lindahl, B. Hess, G. Groenhof, A. E. Mark, H. J. C. Berendsen, *J. Comput. Chem.* **26** (2005) 1701 (https://doi.org/10.1002/jcc.20291)

21. V. Zoete, M. A. Cuendet, A. Grosdidier, O. Michielin, *J. Comput. Chem.* **32** (2011) 2359 (https://doi.org/10.1002/JCC.21816)

22. K. Vanommeslaeghe, E. Hatcher, C. Acharya, S. Kundu, S. Zhong, J. Shim, E. Darian, O. Guvench, P. Lopes, I. Vorobyov, A. D. Mackerell, *J. Comput. Chem.* **31** (2010) 671 (https://doi.org/10.1002/JCC.21367)

23. S. Boonstra, P. R. Onck, E. Van Der Giessen, *J. Phys. Chem., B* **120** (2016) 3692 (https://doi.org/10.1021/acs.jpcb.6b01316)

24. P. J. P. Tjitda, F. O. Nitbani, T. D. Wahyuningsih, R. I. Lerrick, Y. M. Abanit, *ChemistrySelect* **10** (2025) 1 (https://doi.org/10.1002/slct.202404851)

25. P. J. P. Tjitda, F. O. Nıtbanı, A. A. Parıkesıt, M. I. T. Bessı, T. D. Wahyunıngsıh, *Trop. J. Nat. Prod. Res.* **8** (2024) 6208 (https://doi.org/10.26538/TJNPR/V8I2.18)

26. L. P. Hastuti, F. Hermawan, M. R. Iresha, T. Ernawati, Firdayani, *Informatics Med. Unlocked* **47** (2024) 1 (https://doi.org/10.1016/J.IMU.2024.101485)

27. R. L. S. Shrestha, P. Neupane, S. Dhital, N. Parajuli, B. Maharjan, T. Shrestha, S. Bharati, B. P. Marasini, J. A. Subin, *Moroccan J. Chem.* **12** (2024) 1742 (https://doi.org/10.48317/IMIST.PRSM/MORJCHEM-V12I4.48008)

28. V. K. Vyas, T. Shukla, K. Tulsian, M. Sharma, S. Patel, *Comput. Biol. Chem.* **101** (2022) 107787 (https://doi.org/10.1016/J.COMPBIOLCHEM.2022.107787).

Optimisation of the controlled release of valsartan *via* cellulose acetate butyrate and poly(butylene succinate) microspheres: Influence of formulation conditions

AISSA BOUHARAOUA[1], HAOUARIA MERINE[1] and YOUSSEF RAMLI[2]*

[1]Laboratory of Macromolecular Physical and Organic Chemistry, Faculty of Exact Sciences, University of Djillali Liabes, Sidi Bel-Abbes, Algeria and [2]Laboratory of Medicinal Chemistry, Drug Sciences Research Center, Faculty of Medicine and Pharmacy, Mohammed V University, Rabat, Morocco

Abstract: This study investigates the formulation of valsartan-loaded cellulose acetate butyrate (CAB) microspheres, prepared *via* solvent evaporation microencapsulation, to evaluate their *in vitro* release behavior and the influence of formulation parameters. The study examined the effects of stirring speed, stabilizers and matrix materials on particle size and drug release. Increasing stirring speed reduced particle size but also led to higher valsartan loss, reducing encapsulation efficiency. Using the surfactant polylactic acid resulted in smooth, spherical and porous microspheres that enhanced controlled release. In contrast, using Tween 80 led to irregular particles with rough surfaces and larger pores that accelerated drug release. Including poly(butylene succinate) in the matrix resulted in smaller microparticles forming and a significantly higher rate of valsartan release. These findings emphasize the importance of optimizing formulation parameters and excipients to control drug release characteristics and enhance drug delivery system performance.

Keywords: valsartan; microencapsulation; polymer carriers; formulation conditions; controlled release.

INTRODUCTION

Valsartan (Vals), chemically known as (2*S*)-3-methyl-2-[pentanoyl-[[4-[2--(2*H*-tetrazol-5-yl)phenyl]phenyl]methyl]amino]butanoic acid, is a potent and selective competitive antagonist of the AT1 angiotensin II receptors and is widely prescribed for the treatment of hypertension (Scheme.1).[1,2]

By inhibiting angiotensin II, it causes vasodilatation, reduces blood pressure and improves blood flow.[3,4] As a tetrazole derivative, valsartan contains acidic

---

* Corresponding author. E-mail: merine_houaria@yahoo.fr

1331

(pK_a 4.73) and carboxylic (pK_a 3.9) groups that contribute to its pH-dependent solubility. Specifically, its solubility increases by a factor of 1000 when the pH is shifted from 4 to 6. The compound exhibits complete and rapid dissolution in vitro at pH 5.0 or higher, suggesting that its rate of absorption is influenced by the pH of the gastrointestinal tract.[5]
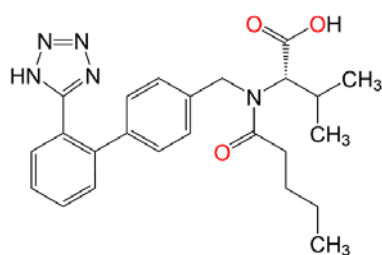
Scheme 1. Chemical structure of valsartan.

Valsartan is poorly soluble in the upper gastrointestinal tract, where most of its absorption occurs. This poor solubility limits absorption, leading to low oral bioavailability (approximately 23 %),[6] despite rapid uptake. To overcome this issue, sustained-release formulations are required. Microencapsulation is being explored as an effective method of controlling drug release and improving therapeutic efficacy.[7]

Solvent evaporation microencapsulation is a widely recognised technique for the production of microparticles, valued for its simplicity of manufacture while maintaining drug efficacy. In studies on valsartan, the preparation of valsartan--loaded microspheres using different matrices such as poly-ε-caprolactone (PCL) and polylactic acid (PLA) showed that PCL provided a more controlled and gradual release of valsartan compared to PLA when tested in vitro in a phosphate--buffered saline solution at pH 6.8. Furthermore, analysis of various factors affecing encapsulation – such as surfactant concentration, PLA amount, aqueous phase volume and stirring speed-showed that increasing surfactant concentration and aqueous phase volume negatively affected the encapsulation rate of valsartan, leading to a decrease in encapsulation efficiency as these parameters were increased.[2]

Previous studies have mainly focused on the formation of inclusion complexes with cyclodextrins,[8,9] the development of solid dispersions using hydrophilic carriers[1,10] and encapsulation within lipids like lecithin and cholesterol.[6,11] These strategies aim to improve the solubility and bioavailability of poorly water-soluble drugs. However, research specifically targeting the encapsulation of valsartan in polymeric matrices remains relatively limited, despite the potential benefits in terms of controlled release and stability. However, some studies have made significant contributions in this area, particularly those investigating the encapsulation of valsartan in gelatin and hydroxypropyl methylcellulose (HPMC)

by spray drying,[12] using gelation techniques with sodium alginate and HPMC,[13] and nanoprecipitation for Eudragit L100.[14] These efforts highlight the growing interest in polymer-based delivery systems for valsartan, although further investigation is needed to optimise these techniques for clinical applications.

In this study, two carrier systems were used to develop rapid release solid formulations: the biodegradable and non-toxic polymeric matrices CAB and PBS, a biodegradable aliphatic polyester. Cellulose acetate has been used extensively in temporary surgical materials (such as sutures, plates and screws) and as a matrix for encapsulating and releasing therapeutic agents in the human body.[15] PBS, with properties similar to polyolefins, offers advantages such as heat resistance and balanced mechanical properties, making it suitable for a wide range of applications.[16]

Our research group recently investigated the preparation of hydrochloro-thiazide (HCTZ)-loaded microspheres using different matrices, such as ethylcellulose, PCL, β-cyclodextrin (β-CD) and poly(methyl methacrylate) (PMMA), synthesised in different fractions, to analyse their influence on encapsulation efficiency and drug release kinetics.[17] In addition, Badis *et al.*[18] continued the study of allopurinol encapsulation using different matrices, including EC, HPMC, β-CD and PCL, using the solvent evaporation method for extended release of this drug. As part of our efforts to develop new drug formulations that allow a gradual release of the active ingredient and overcome the limitations of traditional pharmaceutical forms, in particular to reduce the frequency of administration, we investigated the encapsulation of valsartan using two matrices (CAB and PBS), also using the solvent evaporation method for extended release. This study also focused on characterising the interaction between valsartan and the matrix by evaluating the influence of several factors such as stirring speed, stabiliser effect and the ratio of the dispersed phase to the continuous phase. Micro- and nano-sized particles were characterised using spectroscopic techniques, including Fourier transform infrared (FTIR) spectroscopy and powder X-ray diffraction (PXRD), to study their dissolution behaviour. The main objective of this study was also to evaluate the impact of these factors on the encapsulation efficiency and drug release kinetics in the intestinal tract.

MATERIALS AND METHODS

Chemicals

Valsartan (molar mass: 435.518±0.0231 g mol^{-1}) was generously provided by the Therapeutic Chemistry Laboratory at the Faculty of Medicine and Pharmacy, Mohamed V University in Rabat, Morocco. The micro-encapsulation of solid microspheres was achieved using the solvent evaporation technique, utilizing our synthesized PBS and CAB as matrices, with valsartan as the active agent. CAB, with a viscosity of 0.1 Pa s for a 5 mass % solution in a toluene/ethanol mixture ($\phi r = 4:1$), was sourced from Merck (India), while polyvinyl alcohol (PVA, 87–90 % hydrolysed, molar mass 30000–70000) and Tween 80 were purchased from

Sigma–Aldrich. Dichloromethane (DCM >98 % purity) was used as the internal phase. A phosphate buffer solution at pH 7.4 was prepared by mixing 250 mL of 0.2 M monobasic potassium phosphate (KH_2PO_4) solution with 195.5 mL of 0.1 M sodium hydroxide solution and adjusting the final volume to 1 L with deionized water.

Synthesis and characterization of poly(butylene succinate) (PBS)

The synthesis of PBS was successfully carried out using ring-opening polymerization. A mixture of butan-1,4-diol (0.12 mol) and succinic acid (0.10 mol) was reacted in the presence of 1–2 % titanium isopropoxide as a catalyst. The reaction was refluxed for 2 h at 180 °C with vigorous stirring under a nitrogen atmosphere. To purify the obtained polymer and remove any residual monomers, the product was heated at 200 °C under reduced pressure (maximum of 10^{-3} mm Hg) for three hours.[18,19]

The white PBS powder was characterized; IR, $\bar{v}$ (cm^{-1}): 1710, C=O (ester); 2920–2940 (CH$_2$); 1100–1200 (ester C–O–C); 1310–1330 (C–H); 3429–3552 (terminal O–H). ^{1}H-NMR spectra, Scheme 2: δ_H(CDCl$_3$), ppm: 1.65 (CH$_2$(a)); 1.55 (CH$_2$(a')); 2.55 (CH$_2$(c)); 4.05 (CH$_2$(b)); 3.55 (CH$_2$(d)). ^{13}C-NMR, ppm: 25 (CH$_2$(a)); 25 (CH$_2$(a')); 29 (CH$_2$(c)); 64 (CH$_2$(b)); 62 (CH$_2$(d)); 172 (CO ester).
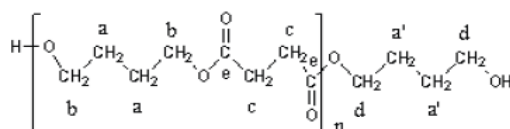
Scheme 2. Chemical structure of poly(butylene succinate) (PBS).

Preparation of solid dispersions

To prepare solid dispersions of valsartan, CAB polymer was combined with valsartan by solvent evaporation in a 2:1 weight ratio (polymer corresponding to 50 % valsartan by weight relative to the polymer). First, valsartan and the polymer were dissolved in dichloromethane (DCM), a water-immiscible organic solvent, in amounts of 66 or 33 g, as required. This organic solution was then poured into 250 g of deionised water, which served as the external phase, containing 1 % PVA or Tween (1 % by mass in water, as specified). Emulsification of the organic phase with the aqueous phase was achieved by mechanical stirring at two speeds (800 or 1200 rpm) in a 600 mL glass reactor (diameter = 80 mm) using a four-bladed turbine impeller (blade length = 50 mm, width = 8 mm; IKA RW20 digital, UK). Valsartan microencapsulation was completed after 3 h at room temperature to allow time for solvent evaporation. The resulting microparticles were collected by vacuum filtration, rinsed several times with deionised water and dried in a desiccator with CaCl$_2$ for at least 48 h. The initial composition of the different microsphere formulations is shown in Table I.

Microsphere characteristics

During the manufacture of microsphere formulations, the drug and polymer may come into close contact, potentially impacting the drug's stability. The evaluation of drug–polymer interactions is essential for the selection of a suitable polymer. Various methods have been used to evaluate the compatibility between valsartan and specific polymers.

Fourier transform infrared spectroscopy (FTIR)

The FTIR spectra of the drug, polymers and microparticles in powdered form were obtained using an Alpha Bruker IR spectrometer, covering the wavelength range of 400 to 4000 cm^{-1}.

TABLE I. Processing conditions for the formulated microspheres

Code	Composition	N / rpm	Emulsifier nature	DCM volume, cm^3
L1	CAB/Vals	800	PVA	50
L2	CAB/Vals	1200	PVA	50
L3	CAB/Vals	800	TWEEN	50
L4	CAB/Vals	1200	TWEEN	50
L5	CAB/Vals	800	PVA	25
L6	CAB/Vals	1200	PVA	25
L7	CAB/PBS/Vals	800	PVA	50
L8	CAB/PBS/Vals	1200	PVA	50

Powder X-ray diffraction (XRD)

XRD patterns of the pure drug, carriers, and microsphere formulations were captured using a Rigaku MiniFlex 600 (MiniFlex acquisition system, λ = 1.541 Å) over a 2θ range from 5 to 70°, and analyzed for comparative purposes.

Particle size analysis

The average diameters and size distribution of the microspheres were determined using optical microscopy (Optika 4083.B1), by counting over 500 microparticles for each preparation. The particle size distribution was calculated from various equations.[20,21] The calculations include the number mean diameter d_{10}, the surface mean diameter d_{32}, the weight mean diameter d_{43} and the size distribution δ. The average diameters and size distribution of the microspheres were assessed using two complementary techniques. Additionally, for formulations prepared at a stirring speed of 1200 rpm (L2, L4, L6 and L8), particle diameters were determined using a Zetasizer Nano ZS (Malvern Instruments, UK). This instrument operates based on dynamic light scattering (DLS), which estimates the hydrodynamic size of particles in suspension by analyzing fluctuations in the intensity of scattered light resulting from Brownian motion:

$$d_{10} = \Sigma n_i d_i / \Sigma n_i \qquad (1)$$

$$d_{32} = \Sigma n_i d_i^3 / \Sigma n_i d_i^2 \qquad (2)$$

$$d_{43} = \Sigma n_i d_i^4 / \Sigma n_i d_i^3 \qquad (3)$$

$$\delta = d_{32} / d_{10} \qquad (4)$$

Scanning electron microscopy of microparticles

The surface characteristics and morphology of valsartan microspheres were examined in detail using a scanning electron microscope (Hitachi TM 1000).

Determination of drug loading and microparticle yield

The valsartan content of the microspheres was assessed by extraction of the drug in absolute ethanol followed by spectrophotometric measurement at 251 nm (ε = 13681 L mol^{-1} cm^{-1}) using a UV spectrophotometer (model Shimadzu UV-2401). For each test, 40 mg of microparticles (prepared with CAB or CAB/PBS mixture, as appropriate) were dispersed in 10 mL of absolute ethanol in a sealed vial for 3 h. After appropriate dilution, the resulting solution was analysed for valsartan content by UV–Vis spectroscopy. The actual drug loading (*DL*), the encapsulation efficiency (*EE*) and yield (*PY*) of microspheres were calculated using the following equations:

$$DL = 100\frac{\text{Vals mass in microsphers}}{\text{mass of microsphers}} \tag{5}$$

$$EE = 100\frac{\text{Vals actual drug load}}{\text{Theoretical drug load}} \tag{6}$$

$$PY = 100\frac{\text{Microspheres recovered (practical mass)}}{\text{Mass of carrier and drug used in the formulation (theoretical mass)}} \tag{7}$$

In vitro *valsartan dissolution studies*

In vitro dissolution testing of valsartan from the prepared formulations was performed using a suitable glass dissolution reactor maintained in a water bath at 37±0.5 °C with a stirring speed of 500±1 rpm. Appropriate quantities of formulations containing 40 mg of valsartan were placed in 1000 mL glass flasks filled with 900 mL of simulated liquid at pH 7.4. At specified time intervals, 5 mL aliquots were removed from the dissolution medium and replaced with an equal volume of prewarmed (37±0.5 °C) fresh dissolution medium. Valsartan concentrations were measured using a Shimadzu UV-2401 UV–Vis spectrophotometer at the drug's maximum absorbance wavelength (λ(max) = 251 nm, ε = 13,105 L·mol^{-1}·cm^{-1}) in a phosphate buffer solution (pH 7.4) that simulated intestinal conditions. The amount of valsartan in each sample was determined spectroscopically and the corresponding drug release profiles were plotted, showing the cumulative percentage drug release (calculated from the total amount of Vals in each formulation) *versus* time. Each batch was tested in duplicate and the mean values were used for calculations. Two mathematical models, the Higuchi and Korsmeyer–Peppas equations, were used to analyse the drug transport mechanisms and predict the kinetics of drug release.[22-25]

RESULTS AND DISCUSSION

Microspheres characterizations

Excipients are an essential component in nearly all pharmaceutical dosage forms. The successful formulation of a stable and effective solid dosage form relies on selecting appropriate excipients, which are added to facilitate drug delivery and protect it from degradation.

In this study, eight microparticles were characterized in terms of shape, surface morphology, drug entrapment and size (mean diameter). The development of eight formulations loaded with valsartan using different polymers *via* solvent evaporation, with varying polymer proportions and experimental conditions, resulted in differences in particle size (mean diameter), surface morphology and drug entrapment. The results for drug loading (*DL*), percentage practical yield (*PY*), encapsulation efficiency (*EE*) and size distribution are presented in Table II.

The operating conditions of the microencapsulation process can influence the drug loading, the percentage of practical yield as well as the mean particle size and its distribution.[26,27]

Optical microscopy analysis of different samples prepared at a stirring speed of 800 rpm showed that the microparticle shapes were spherical with diameters

ranging from 69.7 to 3.5 µm. The particle size dispersion ranged from 1.65 for batch 3 to 1.24 for batch 7 (Fig. 1).

TABLE II. Results of the microencapsulation process for the prepared microspheres

Code	DL / %	PY / %	EE / %	d_{10} / µm	d_{32} / µm	d_{43} / µm	δ (PDI)
L1	33.18	84.96	84.58	45.7	56.2	62.3	1.36
L2	31.64	74.51	70.72		0.5		0.53
L3	23.75	59.77	42.58	48.9	69.7	80.7	1.65
L4	26.47	52	41.30		0.3		0.26
L5	30.182	55	49.76	5.3	6.3	7.0	1.31
L6	31.07	55	51.20		0.7		0.75
L7	32.03	50.09	48.20	3.0	3.5	3.8	1.24
L8	38.97	55.54	65		2.0		1
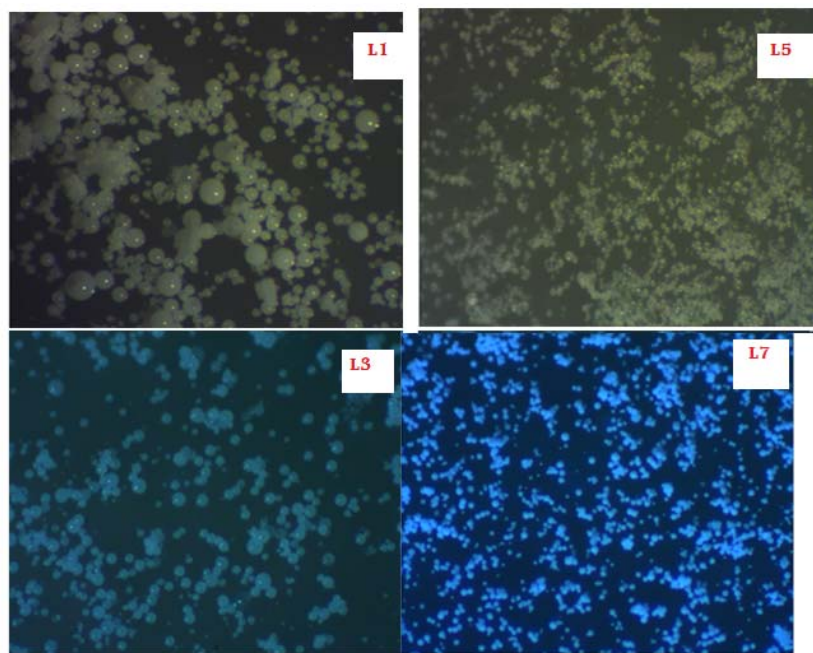
Fig. 1. Optical microscopy images of spherical valsartan-loaded CAB and PBS microparticles (L1, L3, L5 and L7), observed at 100× magnification.

For microparticles prepared at a speed of 1200 rpm (Lots: 2, 4, 6 and 8), the diameter study was carried out using a zetameter and dynamic light scattering (DLS). The rotation speed of 1200 rpm influenced the particle size and distribution, allowing optimal homogeneity in the formulation. The results showed that the microparticle diameter was in the range of 40 to 200 nm (Table II). This relatively small and well-defined size is particularly favourable for pharmaceutical

applications, ensuring better bioavailability and efficient diffusion of the drug into the target tissues. In addition, the narrow size distribution obtained is beneficial for controlling the release of the drug and maximising its therapeutic efficacy.[28]

The surface and morphology of the microspheres were also studied using scanning electron microscopy (SEM). The photographs of formulations 1 and 2, Fig. 2, show that the microparticles composed exclusively of cellulose butyrate acetate are individualised, spherical and have a rough surface.
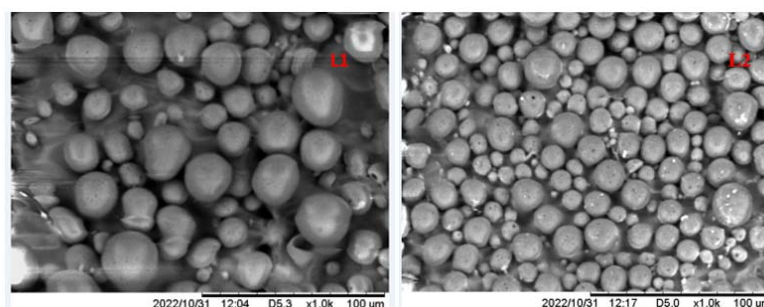
Fig. 2. SEM images showing the surface and morphology of Vals-loaded microspheres.

In all formulations the drug content ranged from 23.75 to 38.97 %, while the practical yield varied from 50.10 to 84.96 %. Formulation batch 3 had the lowest drug content while batch 8 had the highest. Furthermore, batch 1 had the highest yield while batch 7 had the lowest.

Various factors affect the content, yield, size and morphology of microparticles. In this study, we investigated how formulation parameters such as stirring speed, surfactant type, organic/aqueous phase fraction, as well as matrix composition and nature, have influence on microparticle characteristics.

Effect of stirring speed and shear

Agitation is a key parameter influencing microsphere size. The most common model for describing particle size variation with agitation is based on Kolmogorov's theory.[29]

In most studies, experimental results were in agreement with theoretical predictions. It has been observed that, under identical operating conditions, an increase in stirring speed affects the microsphere characteristics, in particular the size of the microspheres and the drug content.[18,30,31]

All formulations (L1–L8) exhibited well-defined, perfectly individualized spherical shapes (Fig. 1). The particle size distributions, determined by light microscopy and zeta analysis, showed a clear trend of decreasing particle size as the stirring speed increased from 800 to 1200 rpm. Specifically, the average particle size decreased from 56.2 µm in L1 to 0.5 µm in L2 and from 69.7 µm in L3 to 0.3

μm in L4. Furthermore, the size distribution (δ) improved from 1.52 to 1.31 under these conditions.

This reduction in particle size can be attributed to the higher energy input during emulsification at elevated stirring speeds (1200 rpm), which facilitates the efficient breakup of the organic phase into smaller, well-dispersed droplets.[32]

However, an inverse relationship was observed between stirring speed and drug loading. Formulations prepared with PVA as the emulsifier demonstrated this effect clearly. The drug loading, expressed as the percentage of the actual valsartan content in the microspheres relative to their mass, decreased from 33.18 in L1 to 31.64 % in L2 and from 49.76 % in L5 to 31.07 % in L6.

Many studies, including those by Mouffok *et al.*,[30] Badis *et al.*[18] and Merdoud *et al.*[31] have shown that higher stirring speeds typically result in smaller microparticle sizes and reduced encapsulation efficiency of the active ingredient. This effect is likely attributed to increased shear forces that interfere with the encapsulation process.

Effect of stabilising agents

Stabilizing agents are essential for maintaining emulsion stability, as they lower the interfacial tension between the continuous and dispersed phases. They also inhibit the coalescence and aggregation of emulsion droplets, especially in the early stages of solvent evaporation.[32,33]

The effect of PVA and Tween 80 surfactants on microspheres prepared under identical operating conditions (Vals ratio 1:2, stirring speed 800 rpm) is shown in Fig. 1. Microspheres stabilised with PVA (Fig. 1: L1) were spherical and smaller in size ($d_{32} = 56.2$ μm) compared to those stabilised with Tween 80 ($d_{32} = 69.7$ μm), which had a rough and porous surface (Fig. 1: L3).

Table II compares the effects of PVA and Tween 80 on key parameters including drug loading (DL), encapsulation efficiency (EE), yield, Sauter mean diameter (d_{32}) and size distribution (δ). Smaller microspheres were consistently obtained with PVA, consistent with results reported in the literature.[34]

PVA was more effective than Tween 80 in reducing the interfacial tension, thus limiting droplet coalescence during emulsification. Higher concentrations of PVA further improved drug loading and encapsulation efficiency while reducing mean particle size (d_{32}) and size distribution (δ). In particular, PVA achieved a higher encapsulation efficiency (*EE* = 84.58 % for L1) compared to Tween 80. This can be attributed to the properties of the polymer, the controlled stirring speed of 800 rpm and the smoother microsphere surfaces produced with PVA.

In contrast, microspheres prepared with Tween 80 exhibited significant surface porosity, resulting in significant loss of valsartan, which negatively affected both *DL* and *EE*. These observations are consistent with the findings of Mouffok

et al.,[30] who also highlighted the detrimental effect of surface porosity on drug encapsulation efficiency.

Effect of dispersed phase on continuous phase

The dispersed phase to continuous phase (D/C) ratio is a critical parameter in solvent evaporation microencapsulation as it significantly influences the properties of the resulting microparticles. Optimisation of this ratio is essential to achieve desired particle characteristics such as size, homogeneity, morphology and encapsulation efficiency. Experimental adjustments are often required to tailor the D/C ratio to the specific properties of the phases involved and the process objectives.[32,35,36]

A low D/C ratio generally results in better size homogeneity and smaller microparticles, as each droplet of dispersed phase contains less material and droplet formation is more controlled. In addition, low D/C ratios promote the formation of microspheres with smoother surfaces, probably due to the faster solidification rate. The higher water content in the continuous phase accelerates polymer precipitation, resulting in less porous microspheres.[36,37] Notably, a reduction in the D/C ratio was associated with a significant increase in encapsulation efficiency.[38]

Our results are consistent with previous findings. For example, a significant improvement in encapsulation efficiency (DL = 49.76 %) was observed in batch 5 (D/C ratio of 0.1) compared to batch 1 (DL = 33.18 % for D/C ratio of 0.2). As shown in Fig. 1, L5, with a lower D/C ratio, produced smaller microparticles (d_{32} = 6.3 μm) with a compact and well-formed surface. In contrast, L1, with a higher D/C ratio, produced larger microparticles (d_{32} = 56.2 μm) with a porous surface.

The influence of the D/C ratio was particularly evident in batches prepared at a stirring speed of 800 rpm, where differences in particle morphology and size were pronounced. However, for batches 2 and 6, prepared at a higher stirring speed of 1200 rpm, the effect of the D/C ratio was less pronounced as the increased stirring speed dominated the characteristics of the microparticles.

Impact of polymer properties

The properties of the polymer used play a critical role in determining encapsulation efficiency, particle size and drug release rate, as has been extensively discussed in the literature.[30,39–41] Two key parameters that influence the organic phase and consequently the encapsulation rate are polymer concentration and molar mass.

An increase in polymer mass or molar mass increases the viscosity of the organic phase, thereby limiting drug migration into the external aqueous phase.[42] This effect, which is attributed to faster precipitation of the polymer in the droplets, results in higher encapsulation efficiency.[39,43]

Similarly, polymer concentration and molar mass have a significant effect on particle size by modifying the viscosity of the organic phase, which in turn influences droplet rupture behaviour. Both theoretical and experimental studies[17,18,31,40,42,43] have shown that reducing the molar mass of the polymer at a constant solvent volume reduces the viscosity of the organic phase, facilitating the formation of smaller microparticles.

The inclusion of PBS in the formulations (L7 and 8) slightly improved drug entrapment compared to L1 and 2, which were prepared using the same solvent conditions, PVA concentrations and stirring speeds. L1 achieved a high yield of 84.58 %, reflecting minimal loss of microspheres during preparation and recovery. In contrast, L7 showed a lower yield of 49 %, which was influenced by polymer agglomeration and adhesion to the stirrer blades and beaker walls during microsphere formation. In addition, migration of small microparticles during filtration further reduced the yield for L7 (d_{32} = 3.5 µm).

The particle size distribution in batch 7 was narrower (δ = 1.24), probably due to the reduced viscosity in the dispersed medium caused by the lower molar mass of PBS. These results are consistent with previous studies reported in the literature.[17,18,31]

Microsphere spectroscopy

FTIR spectroscopy confirmed the actual presence of valsartan in the microspheres (Fig. 3) and highlighted the chemical stability of the drug. The FTIR spectra of the valsartan loaded microspheres were compared with those of pure valsartan and the CAB and PBS polymer matrices (Fig. 3).

The FTIR spectrum of pure valsartan (Fig.3a) is characterised by a broad band at 3444.86 cm^{-1}, corresponding to the stretching of the N–H bond as mentioned by Islas *et al*.[43] A band at 2961.67 cm^{-1} is observed, attributed to the extension of the –CH bond in the methyl group (CH$_3$). Two intense carbonyl bands are detected at 1730.38 and 1597.43 cm^{-1}, corresponding to the elongation of the C=O of the carboxyl group and the C=O of the amide function, respectively.

A band located at 755.83 cm^{-1} is associated with the out-of-plane deformations of the N–H bond in the primary amine. Finally, a band at 1409.56 cm^{-1} is observed, which is attributed to the stretching of the N=N bond.

The FTIR spectrum of CAB alone (Fig. 3b) showed a strong stretching vibration band at 1733.59 cm^{-1}, attributed to the C=O bond originating from the acetate and butyrate groups in the polymer. A series of characteristic absorption peaks for the CAB polymer were observed at 2961.82, 2935.20 and 2873.31 cm^{-1}, corresponding to the asymmetric and symmetric stretching vibrations of the CH$_3$ and CH$_2$ groups. The region between 1235 and 1050 cm^{-1} is associated with the stretching vibrations of the C–O bonds in the ester groups (acetate and butyrate).
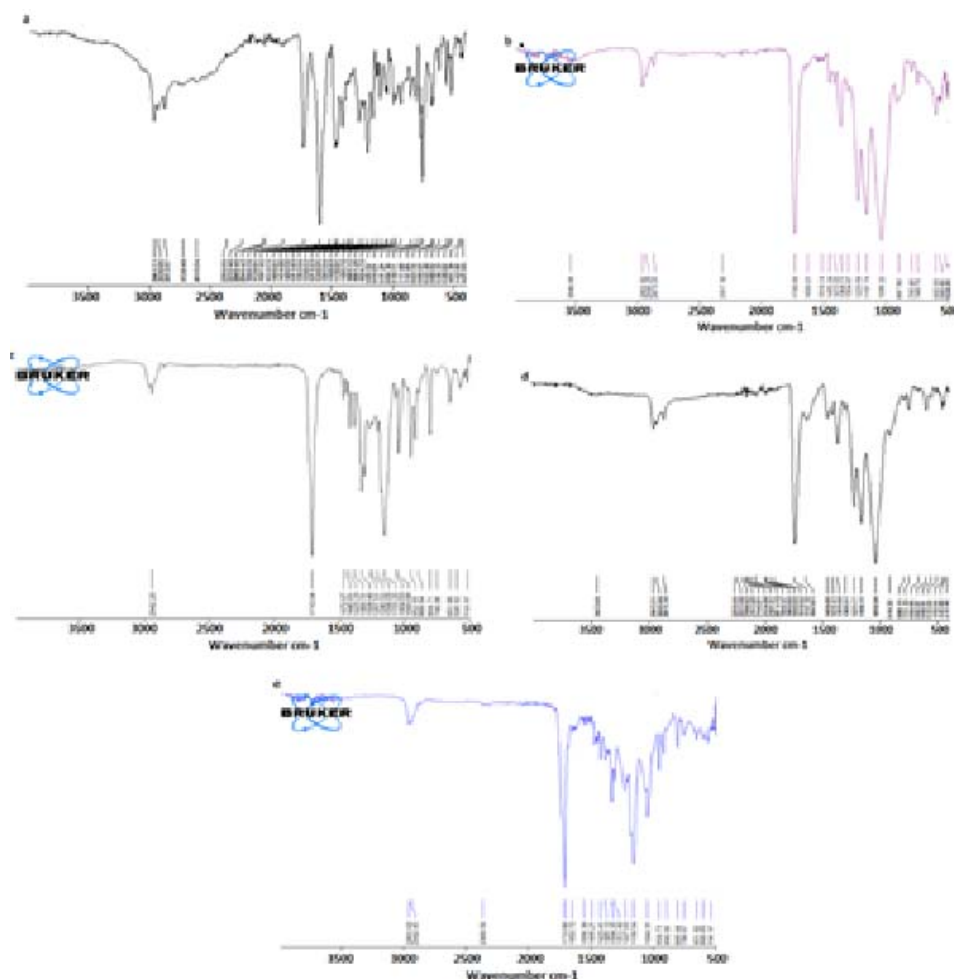
Fig. 3. FTIR patterns of: a) valsartan, b) CAB,(c) PBS, d) L1 and e) L7.

The infrared spectra of the microspheres (Fig. 3d) show characteristic bands similar to those of valsartan and CAB matrix, indicating the intact presence of the drug and polymer. In addition, a broad peak observed at the same positions as in the spectra of pure valsartan and CAB, without the appearance of new bands, suggests the absence of physical interaction between the drug and the polymers. The transmittance variations are explained by the concentration differences between the components.

The FTIR spectrum of batch 7 (Fig. 3e), derived from the combination of the two matrices CAB and PBS with valsartan, showed the characteristic stretching bands of the carbonyl group at 1711 cm^{-1} for the ester function of PBS and at 1650

cm^{-1} for valsartan. These results confirm the successful incorporation of both PBS (Fig. 3c) and valsartan (Fig. 3a) into the microspheres.

Finally, by comparing the IR-TF spectrum of pure valsartan with that of microspheres from batches 1 to 8, it is observed that the C=O band of the amide function (around 1597.43 cm^{-1}) has shifted to higher wave numbers. This shift can be attributed to the disruption of intermolecular and/or intramolecular hydrogen bonds in valsartan during its microencapsulation with CAB and PBS.[44]

The XRD spectrum of pure valsartan is shown in Fig. 4a. The XRD shows the absence of distinct peaks, indicating that valsartan is in amorphous form. Other studies such as Wang *et al.*[45] and Youn *et al.*,[46] have also observed an amorphous structure for pure valsartan.

Examining the XRD of the CAB polymer (Fig. 4b), it is noted that it does not show any crystalline peaks, suggesting an amorphous structure. This results in an amorphous combination when valsartan and CAB are physically mixed in microspheres (batches 1–6) as shown in the XRDs of batches 1, 3 and 5 (Fig. 4d–f).

In contrast, the X-ray diffractogram of the PBS polymer (Fig. 4c) shows a partially crystalline phase with two distinct peaks at 2θ equal to 19.67 and 22.72°, characterising a semi-crystalline structure.

A comparison of the X-ray diffraction patterns of valsartan, CAB and PBS with those of formulation L7 (see Fig. 4g) shows that the crystalline state of valsartan increases significantly in the solid dispersion while the characteristic peaks of PBS are maintained. Pure valsartan exhibited a broad amorphous halo in the 2θ range of 13.8–15.0°, but this was no longer observed in the L7 formulation. This suggests that valsartan underwent a partial structural reorganization into a semi-crystalline form.

Drug dissolution of valsartan

Valsartan, a tetrazole derivative, contains acidic (pK_a 4.73) and carboxylic groups (pK_a 3.9) that significantly affect its solubility, especially within the neutral pH range.[47] At physiological pH, it exists as undissociated acid, mono-anion or di-anion. Its solubility markedly increases between pH 4 and 6, favoring the anionic form but reducing lipophilicity, which in turn influences its gastrointestinal absorption. Dissolution becomes rapid and complete at pH 5.0 or higher.[48]

At 25 °C, valsartan's solubility in water is 0.18 g/L but rises substantially in buffered solutions, reaching 16.8 g/L in a phosphate buffer at pH 8.0. These properties are crucial for optimizing its formulation and therapeutic use.[3,5]

In this study, cellulose-based microparticles loaded with valsartan were developed and evaluated for controlled drug release. The release of the encapsulated drug was studied *in vivo* using simulated intestinal (colon) environment at 37 °C and compared with pure drug dissolution.
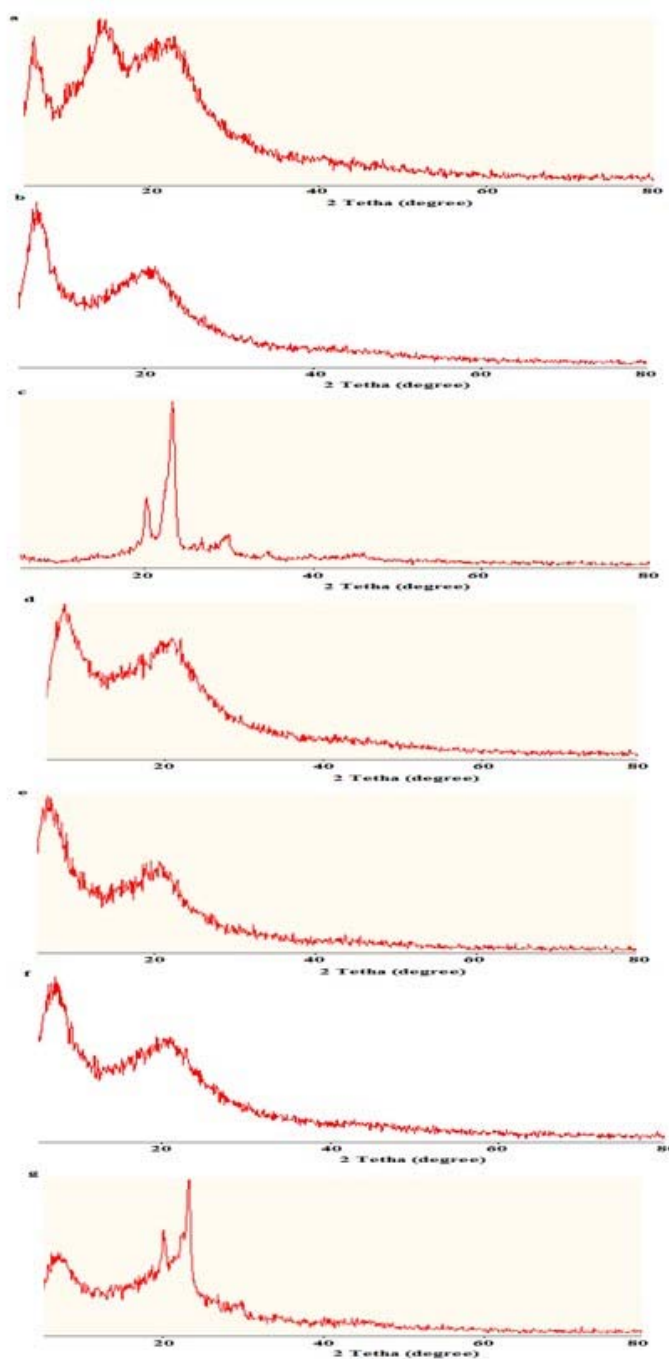
Fig. 4. XRD patterns of: a) valsartan, b) CAB, c) PBS, d) L1, e) L3, f) L5 and g) L7.

Various parameters were adjusted during the preparation process and their effect on drug release is analysed in this work. As highlighted earlier, the characteristics of the microparticles obtained, such as size, morphology and structure, were strongly influenced by the process variables and formulation conditions. These characteristics also influence the mass transfer mechanisms, potentially altering the release profiles.

The pure drug and the eight formulations were subjected to *in vitro* dissolution studies in simulated intestinal fluid (pH 7.4). Samples were collected at different time intervals, filtered and analysed at 251 nm. The dissolution profiles of the pure drug and the binary drug carrier system are shown in Figs. 5–7, and the *in vitro* release results of pure valsartan and all the formulations from L1 to F8 are shown in Table III. Furthermore, the release kinetics of Vals from these formulations were analyzed using the following models during the initial phase, up to 65 % drug release.
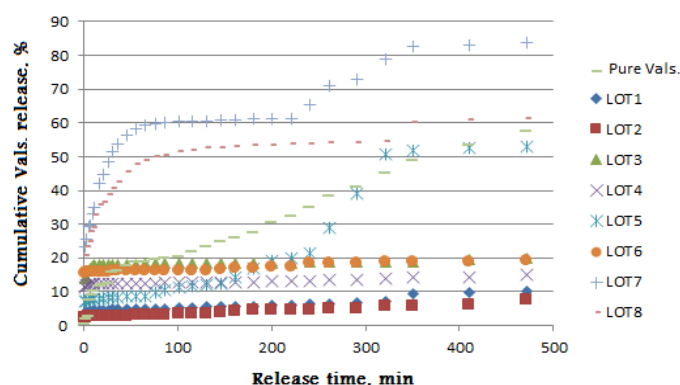
Fig. 5. Percent cumulative drug (Vals.) release *vs*. time in simulated intestinal fluid (pH 7.4).

For a clearer presentation of the results, discussion and to highlight the effects of the formulation parameters, we chose to directly and graphically compare the valsartan release profiles of the microparticle batches, varying each parameter individually.

It should be noted that CAB was used as the primary matrix in batches L1––L6. In addition, the effects of stirring speed, type of stabiliser and ratio of discontinuous to continuous phase were specifically investigated for CAB microspheres. Conversely, the influence of PBS polymer as a secondary matrix was evaluated in batches L7 and L8.

Firstly, the data presented in the table above indicate that valsartan exhibits a gradual but steady dissolution in the intestinal environment (pH 7). The release is initially limited but gradually increases, reaching about 60 % after 8 h.
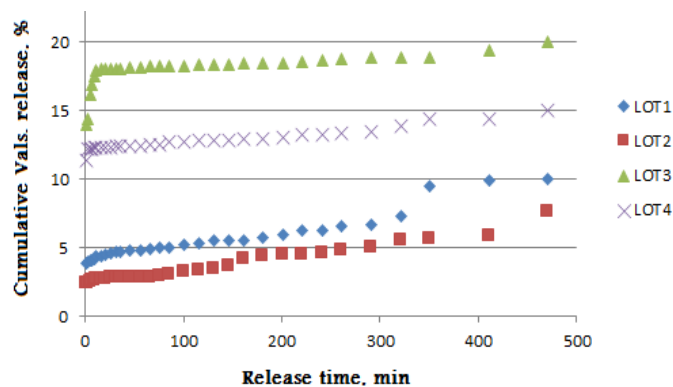
Fig. 6. Effect of stabilising agents in dissolution of valsartan from solid dispersions in simulated intestinal fluid (pH 7.4).
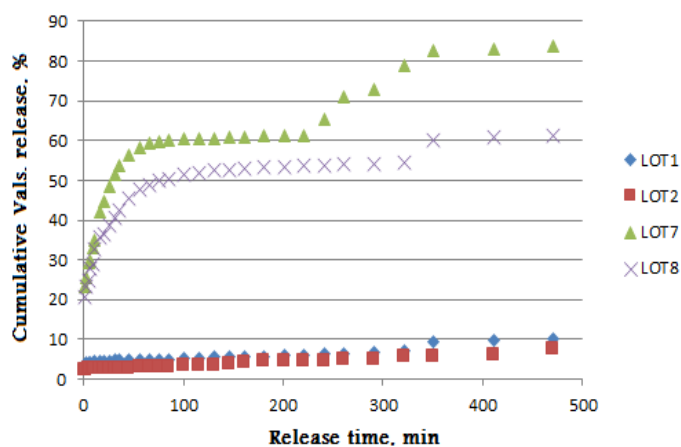
Fig. 7. Effect of PBS matrix in dissolution of valsartan from solid dispersions in simulated intestinal fluid (pH 7.4).

TABLE III. Percentage release data for Vals measured at 30 min and 1, 2 and 8 h

Code	Time			
	30 min	1 h	2 h	8 h
Pure Vals	15.70	18.72	22.50	57.40
L1	4.72	4.86	8.35	10.07
L2	2.80	2.86	3.35	7.64
L3	18.08	18.16	18.34	20.10
L4	12.36	12.44	12.81	15.10
L5	8.36	8.75	11.60	53.04
L6	16.01	16.05	16.20	19.32
L7	50.86	58.80	60.53	83.81
L8	40.61	47.65	51.85	61.17

The encapsulation of valsartan with cellulose acetate butyrate (CAB) significantly reduces its release in a medium at pH 7.4 (Fig. 5). This is likely due to the encapsulating effect of the polymer matrix and its hydrophobic nature, which limit water diffusion and drug release. This is supported by previous studies.[49] These properties slow down the disaggregation and diffusion of the drug while modifying its microstructural environment. These observations, which are consistent with the work of Merdoud et al.[31] who showed a slower release with CAB compared to ethyl cellulose (EC), suggest that CAB is a promising polymer for controlled release formulations.

The decrease in valsartan microparticle size results in a slight decrease in valsartan release, despite the literature linking rapid agitation during microencapsulation with improved release. This observation can be explained by several factors. Firstly, the agitation speeds used (800 and 1200 rpm) remain relatively high, producing microparticles of similar size, thus reducing significant differences in behaviour. Secondly, very small microparticles tend to agglomerate due to interparticle forces, reducing the effective surface area available for dissolution. In addition, the CAB (cellulose acetate butyrate) coating matrix could slow drug release by limiting diffusion from small particles due to physical and chemical barriers. These combined elements explain the slightly reduced release from very fine particles.

Fig. 6 shows that the cumulative release of microspheres prepared with Tween 80 (batches 3 and 4) was faster than that of those containing PVA (batches 1 and 2) due to their porosity and surface morphology (Fig. 6). These findings are consistent with those of Mouffok et al.,[30] who also emphasised the negative impact of surface porosity on drug release. Finally, the introduction of another matrix, such as low molecular weight PBS, also leads to a rapid release of valsartan, as observed in batches 7 and 8 compared to batches 1 and 2 (Fig. 7).

Release mechanisms and mathematical analysis

Mathematical evaluation of *in* vitro drug release was performed using two diffusion models: Higuchi and Korsmeyer models.[24,25] The correlation coefficient (r^2) obtained by plotting the experimental data according to the equations of these models allowed the Higuchi model to be identified as the most appropriate:

$$Q_t = K_H t_2^n \tag{8}$$

or Korsmeyer–Peppas:

$$\frac{M_t}{M_\infty} = K_K t^n \tag{9}$$

where M_t/M_∞ represents the fractional drug release, K_H and K_K are the release constants for the Higuchi and Korsmeyer models, respectively, and n is the release

exponent defining the release mechanism. The Higuchi model describes the release of water-soluble or poorly water-soluble drugs from semi-solid or solid matrix systems.[24] Meanwhile, the exponent n, as defined by Peppas,[50] distinguishes different release mechanisms: Fickian diffusion occurs when $n = 0.5$ and is time-dependent, whereas non-Fickian diffusion is observed when n ranges between 0.5 and 1.0. Case II transport corresponds to $n = 1.0$, while super Case II transport occurs when $n > 1$. When $n < 0.5$, the diffusion mechanism is associated with the quasi-Fickian model. The results of the data analysis are summarised in Table IV.

TABLE IV. Coefficients of correlation and dissolution rate constants of Vals from microspheres in simulated intestinal fluid

Code	K_H	R^2	$\ln K_K$	K_K	n	R^2
L1	0 .481	0.927	1.242	3.463	0.086	0.972
L2	0.344	0.973	0.864	2.373	0.050	0.993
L3	2.281	0.982	2.571	13.080	0.132	0.999
L4	1.592	0.969	2.478	11.917	0.013	0.929
L5	1.013	0.973	1.959	7.092	0.043	0.999
L6	2.045	0.968	2.733	15.379	0.011	0.986
L7	4.237	0.996	2.578	13.171	0.415	0.992
L8	3.708	0.983	2.746	15.580	0.301	0.977

The correlation coefficients and dissolution rate constants of valsartan released from microspheres, based on the investigated models in an intestinal medium, are summarised in Table IV. Overall, according to the coefficient of determination (R^2) values presented in Table IV, the Korsmeyer–Peppas model provided the best fit, with R^2 greater than 0.97 for all formulations except L1 in the Higuchi model ($R^2 = 0.927$) and L4 in the Korsmeyer–Peppas model ($R^2 = 0.929$). These strong correlations suggest that the drug release is predominantly governed by diffusion mechanisms.

The dissolution rate constants of the drug in the simulated intestinal medium (pH 7.4), derived from the Higuchi's equation plots, ranged from 4.237 min$^{-1/2}$ for L7; 3.708 min$^{-1/2}$ for L8; 2.281min$^{-1/2}$ for L3; 2.045 min$^{-1/2}$ for L6; 1.592 min$^{-1/2}$ for L4; 1.013 min$^{-1/2}$ for L5 ; 0.481 min$^{-1/2}$ for L1 to 0.344 min^{-1} for L2. These values, reflect relatively low dissolution constants in the intestinal medium (see Table IV) and are consistent with the results of previous experiments.

Furthermore, the lower n values (0.011–0.415) obtained from the Korsmeyer–Peppas equation (Table IV) suggest a quasi-Fickian release mechanism, ruling out matrix erosion or solubilisation as the dominant release processes.[25,47,48,50,51]

CONCLUSION

This study investigated the effect of valsartan microencapsulation on its release profile. A significant sustained release effect was observed when valsartan was encapsulated with CAB polymer, reaching up to 7.67 % in batch L2. Fur-

thermore, the influence of formulation parameters on the properties and *in vitro* release behaviour of valsartan-loaded CAB microspheres prepared by solvent-evaporation microencapsulation was evaluated. The results showed that increasing the stirring speed during microsphere preparation generally led to a reduction in microparticle size, but could also result in increased valsartan loss, thereby reducing the amount of encapsulated drug. In addition, the use of PVA produced spherical microspheres with smooth, porous surfaces, which facilitated controlled drug release. In contrast, the incorporation of Tween 80 resulted in irregularly shaped microspheres with rough surfaces and larger pores, which accelerated valsartan release. Finally, the inclusion of an additional matrix, such as PBS, resulted in the formation of particularly small microparticles, which were associated with more pronounced valsartan release. These findings highlight the importance of selecting formulation parameters and excipients to modulate the release characteristics of microspheres and optimise the efficacy of drug delivery systems.

In summary, the characteristics of the microspheres were strongly influenced by both the process and the formulation parameters. Higher stirring speeds reduced particle size and improved homogeneity, though they lowered drug loading. PVA produced smaller, smoother particles with a higher encapsulation efficiency than Tween 80 did. Using a lower D/C ratio further enhanced size uniformity and drug entrapment. Polymer properties such as molar mass and viscosity also modulated particle size and loading.

ИЗВОД

ОПТИМИЗАЦИЈА КОНТРОЛИСАНОГ ОСЛОБАЂАЊА ВАЛСАРТАНА ПРЕКО ЦЕЛУЛОЗНОГ АЦЕТАТА-БУТИРАТА И МИКРОСФЕРА ПОЛИ (БУТИЛЕН-СУКЦИНАТА): УТИЦАЈ УСЛОВА ФОРМУЛАЦИЈЕ

AISSA BOUHARAOUA[1], HAOUARIA MERINE[1] и YOUSSEF RAMLI[2]

[1]Laboratory of Macromolecular Physical and Organic Chemistry, Faculty of Exact Sciences, University of Djillali Liabes, Sidi Bel-Abbes, Algeria u [2]Laboratory of Medicinal Chemistry, Drug Sciences Research Center, Faculty of Medicine and Pharmacy, Mohammed V University, Rabat, Morocco

Ова студија истражује формулацију микросфера целулозног ацетата-бутирата (САВ) напуњених валсартаном, припремљених микроенкапсулацијом испаравањем растварача, како би се проценило њихово *ин витро* понашање ослобађања и утицај параметара формулације. Студија је испитала ефекте брзине мешања, стабилизатора и матричних материјала на величину честица и ослобађање лека. Повећање брзине мешања смањило је величину честица, али је такође довело до већег губитка валсартана, смањујући ефикасност енкапсулације. Коришћење сурфактанта полимлечна киселина резултирало је глатким, сферним и порозним микросферама које су побољшале контролисано ослобађање. Насупрот томе, коришћење Tween 80 довело је до неправилних честица са

грубим површинама и већим порама које су убрзале ослобађање лека. Укључивање поли(бутилен-сукцината) у матрицу резултирало је формирањем мањих микрочестица и значајно већом стопом ослобађања валсартана. Ови налази наглашавају важност оптимизације параметара формулације и помоћних материја за контролу карак-теристика ослобађања лекова и побољшање перформанси система за испоруку лекова.

REFERENCES

1. Y. D. Yan, J. H.Sung, K. K. Kim, D. W.Kim, J. O.Kim, B.-J.Lee, C. S.Yong, H.-G. Choi, *Int. J. Pharm.* **422** (2012) 202 (https://doi.org/10.1016/j.ijpharm.2011.10.053)
2. O. Sadoun, F. Rezgui, C. G'Sell, *Mat. Sci. Eng., C* **90** (2018) 189 (https://doi.org/10.1016/j.msec.2018.04.041)
3. M. C Michel, H. R Brunner, C. Fosterd, Y. Huo, *Pharm. Ther.* **164** (2016) 1 (https://doi.org/10.1016/j.pharmthera.2016.03.019)
4. Z. Ma, Z. Fu, N. Li, S. Huang, L. Chi, *BMJ Open* **14** (2024) e088744 (https://doi.org/10.1136/bmjopen-2024-088744)
5. N. Siddiqui, A. Husain, L. Chaudhry, M.S. Alam, M. Mitra, P.S. Bhasin, *J. App. Pharm. Sci.* **01** (2011) 12 (https://japsonline.com/admin/php/uploads/54_pdf.pdf)
6. J.-B Park, C. Park, Z. Z. Piao, H. H. Amin, N. M. Meghani, P. H. L. Tran, T. T. D. Tran, J.-H Cui, Q.-R. Cao, E. Oh, B.-J. Lee, *J. Drug Delivery Sci. Techn.* **46** (2018) 365 (https://doi.org/10.1016/j.jddst.2018.05.031)
7. K. P. Dwivedi, S. Jaiswal, A. K. Srivastava, S. K., Tiwari, P. Singh, S. maddhesiya, N. K. Verma, *Int. J. Med. Pharm. Res.* **4** (2023) 76 (https://doi.org/10.5281/zenodo.8201865)
8. B. Cappello, C. di Maio, M. Iervolino, A. Miro, *J. Incl. Phenom. Macrocycl. Chem.* **54** (2006) 289 (https://doi.org/10.1007/s10847-005-9004-y)
9. C. E. De Matos Jensen, R. A. S. Dos Santos, A. M. L. Denadai, C. F. F. Santos, A. N. G. Braga, R. D. Sinisterra, *Molecules* **15** (2010) 4067 (https://doi.org/10.3390/molecules15064067)
10. B. N. Nalluri, K. P. R. Chowdary, K. V. R. Murthy, G. Becket, P. A. Crooks, *AAPS PharmSciTech* **8** (2007) E1 (https://doi.org/10.1208/pt0802036)
11. B. Parmar, S. Mandal, K. C. Petkar, L. D. Patel, K. K. Sawant, *Int. J. Pharm. Sci. Nanotechol.* **4** (2011)1483 (https://doi.org/10.1016/j.ijpharm.2010.09.007)
12. D. X. Li, Y. D. Yan, D. Hoon Oh, K. Y. Yang, Y. G. Seo, J. O. Kim, Y. I. Kim, C. S. Yong, H. G. Choi, *Drug Deliv.* **17** (2010) 322 (https://doi.org/10.3109/10717541003717031)
13. G. Verreck, I. Chun, J. Peeters, J. Rosenblatt, M. E Brewster, *Pharm. Res.* **20** (2003)10 (https://doi.org/10.1023/a:1023450006281)
14. E. Hajba-Horváth, A. Fodor-Kardos, N. Shah, G. M. Wacker, T. Feczkó, *Int. J. Mol. Sci.* **22** (2021) 13069 (https://doi.org/10.3390/ijms222313069)
15. , *Handbook of Pharmaceutical Excipients*, 5th ed., R. C. Rowe, P. J. Sheskey, S. C. Owen, Eds., American Pharmacists Association, Washington, DC, 2006
16. T. Mahmood, R. M. Sarfraz, A. Ismail, M. Ali, A. Khan, *ASSAY Drug Dev. Technol.* **21** (2023) 65 (https://doi.org/10.1089/adt.2022.119)
17. O. C. Larbi, H. Merine, Y. Ramli, F. B. Toumi, K. Guemra, A. Dehbi, *J. Serb. Chem. Soc.* **83** (2018) 1243 (https://doi.org/10.2298/JSC171112065L)

18. K. Badis, H. Merine, Y. Ramli, O. C. Larbi, C. H. Memou, *J. Mexican Chem. Soc.* **66** (2022) 17 (https://doi.org/10.29356/jmcs.v66i1.1583)

19. S. Chirani, M.O. Lebig, S. Bouameur, M. Mouffok, N. Chirani, N. Chafi, K. Guemra, *Indian J. Pharm. Educ. Res.* **51** (2017) 79 (https://doi.org/10.5530/ijper.50.4.21)

20. K. Kaczmarski, J. C. Bellot, *Acta Chromatogr.* **13** (2003) 22 (https://www.researchgate.net/publication/237326465)

21. C. Jégat, J. L. Taverdet, *Polym. Bull.* **44** (2000) 345 (https://doi.org/10.1007/s002890050612)

22. J. G. Wagner, *J. Pharm. Sci.* **58** (1969) 1253 (https://doi.org/10.1002/jps.2600581021)

23. M. Gibaldi, S. Feldman, *J. Pharm. Sci.* **56** (1967) 1238 (https://doi.org/10.1002/jps.2600561005)

24. T. Higuchi, *J. Pharm. Sci.* **52** (1963) 1145 (https://doi.org/10.1002/jps.2600521210)

25. R. W. Korsmeyer, R. Gurny, E. Doelker, P. Buri, N. A. Peppas, *Int. J. Pharm.* **15** (1983) 25 (https://doi.org/10.1016/0378-5173(83)90064-9)

26. A. André-Abrant, J. L. Taverdet, J. Jay, *Eur. Polym. J.* **37** (2001) 955 (https://doi.org/10.1016/S0014-3057(00)00197-X)

27. E. Schlicher, N. S. Postma, J. Zuidema, H. Talsma, W. Hennink, *Int. J. Pharm.* **153** (1997) 235 (https://doi.org/10.1016/S0378-5173(97)00116-6)

28. C. Prieto, Z. Evtoski, M.Pardo-Figuerez, J. Hrakovsky, J. M. Lagaron, Mol. Pharmaceutics **18** (2021) 2947 (https://doi.org/10.1021/acs.molpharmaceut.1c00098)

29. J.O. Hinze, *AIChE J.* **1** (1955) 289 (https://doi.org/10.1002/aic.690010303)

30. M. Mouffok, A. Mesli, I. Abdelmalek, E. Gontier, *J. Serb. Chem. Soc.* **81** (2016) 1183 (https://doi.org/10.2298/JSC160308068M)

31. A. Merdoud, M. Mouffok, A. Mesli, N. Chafi, M. Chaib, *J. Serb. Chem. Soc.* **85** (2020) 531 (https://doi.org/10.2298/JSC190326132M)

32. P. Sansdrap, A. J. Moes, *Int. J. Pharm.* **98** (1993) 157 (https://doi.org/10.1016/0378-5173(93)90052-H)

33. R. Brahmi, K. Diaf, Z. ELBahri, M. Baitiche, *J. Serb. Chem. Soc.* **89** (2024) 91 (https://doi.org/10.2298/JSC230501088B)

34. C. Grandfils, P. Flandroy, N. Nihant, S. Barbette, R. Jerome, P. Teyssie, A. Thibaut, *J. Biomed. Mater. Res.* **26** (1992) 467 (https://doi.org/10.1002/jbm.820260405)

35. R. Jeyanthi, R. C. Mehta, B. C. Thanoo, P. P. De Luca, *J. Microencapsul.* **14** (1997) 163 (https://doi.org/10.3109/02652049709015330)

36. W. I. Li, K. W. Anderson, P. P. Deluca, *J. Cont. Rel.* **37** (1995) 187 (https://doi.org/10.1016/0168-3659(95)00077-1)

37. Q. Yang, G. Owusu-Ababio, *Drug Dev. Ind. Pharm.* **26** (2000) 61 (https://doi.org/10.1081/DDC-100100328)

38. S. Mao, Y. Shi, L. Li, J. Xu, A. Schaper, T. Kissel, *Eur. J. Pharm. Biopharm.* **68** (2008) 214 (https://doi.org/10.1016/j.ejpb.2007.06.008)

39. B. K. Kim, S. J. Hwang, J. B. Park, H. J. Park, *J. Microencapsul.* **22** (2005) 193 (https://doi.org/10.1080/02652040400015346)

40. M. A. Benoit, B. Baras, J. Gillbard, *Int. J. Pharm.* **184** (1999) 73 (https://doi.org/10.1016/s0378-5173(99)00109-x)

41. P. Le Corre, P. Le Guevello, V. Gajan, F. Chevanne, R. Le Verge, *Int. J. Pharm.* **107** (1994) 41 (https://doi.org/10.1016/0378-5173(94)90300-X)

42. J.C. Jeong, J. Lee, K. Cho, *J. Control. Rel.* **92** (2003) 249 (https://doi.org/10.1016/S0168-3659(03)00367-5)

43. C. Y. Yang, S. Y. Tsay, R. C. C. Tsiang, *J. Microencapsul.* **17** (2000) 269 (https://doi.org/10.1080/026520400288256)

44. M. S. Islas, C. A. Franca, S. B. Etcheverry, E. G. Ferrer, P. A. M. Williams, *Vib. Spectrosc*. **62** (2012) 143 (https://doi.org/10.1016/j.vibspec.2012.04.009)

45. L. Wang, C. Du, Y. Yang, P. Zhang, S. Yuan, *Molecules* **29 (**2024) 5467 (https://doi.org/10.3390/molecules29225467)

46. Y.-S. Youn, J. H. Oh, K. H. Ahn, M. Kim, J. Kim, Y.-W. Lee, *J. Supercrit. Fluids* **59** (2011) 117 (https://doi.org/10.1016/j.supflu.2011.07.008)

47. G. Flesch, P. Muller, P. Lloyd, *Eur. J. Clin. Pharmcol*. **52** (1997) 115 (https://doi.org/10.1007/s002280050259)

48. M. Saydam, S. Takkaj, *FABAD J. Pharm. Sci.* **32** (2007) 185 (https://www.dergi.fabad.org.tr/pdf/volum32/issue4/185-196.pdf)

49. S. Milovanovic, J. Djuris, A. Dapčević, M. L. Skoric, D. Medarevic, S. M. Pavlovic, S. Ibric, *J. Polym. Res.* **28** (2021) 74 (https://doi.org/10.1007/s10965-021-02440-1)

50. P. L. Ritger, N. A. Peppas, *J. Control. Rel.* **5** (1987) 37 (http://dx.doi.org/10.1016/0168-3659(87)90034-4)

51. K. S. Soppimath, A. R. Kulkarni, T. M. Aminabhavi, *J. Microencapsulation* **18** (2001) 397 (https://doi.org/10.1080/02652040010018083).

Comparative study of micellization and surface properties of cationic and anionic surfactants in acetonitrile–water mixed media

SUJIT KUMAR SHAH, SANDESH KARKI and AJAYA BHATTARAI*

Department of Chemistry, Mahendra Morang Adarsh Multiple Campus, Tribhuvan University, Biratnagar, Nepal

Abstract: A comparative study was conducted to investigate the micellization behaviour, surface properties and wettability of the cationic surfactant cetyltrimethylammonium bromide (CTAB) and the anionic surfactant sodium dodecyl sulfate (SDS) in acetonitrile–water (ACN–water) mixed media. Surface tension and contact angle measurements were performed in pure water and ACN–water mixtures (0.10, 0.20 and 0.40 volume fractions of ACN) at 298.15 K to determine the critical micelle concentration (*CMC*), surface excess concentration (Γ_{max}), minimum surface area per molecule (A_{min}), micellar surface pressure (π_{CMC}) and packing parameter (*P*). Contact angle measurements were used to assess wettability on borosilicate glass surfaces. Results indicate that increasing ACN content leads to an increase in *CMC*, suggesting reduced micellization feasibility in less polar media. Surface excess concentration decreases with higher ACN fractions, while minimum surface area per molecule increases, indicating looser molecular packing at the air/solution interface. Contact angle measurements reveal a decrease in wettability with higher ACN content, demonstrating enhanced surfactant adsorption at the solid-liquid interface. Additionally, micellar surface pressure and packing parameter decline with increasing ACN concentration. These findings underscore the critical role of solvent composition in modifying surfactant aggregation and interfacial behaviour.

Keywords: surface tension; surfactant; contact angle; acetonitrile.

INTRODUCTION

Surfactants, a class of amphiphilic organic compounds, play a critical role in various industrial and scientific applications due to their ability to form micelles in solution, which significantly alter the properties of the medium. Amphiphilicity is a property of an organic molecule that possesses both hydrophilic, identified as head and hydrophobic, identified as tail. This dual nature allows them to interact

1353

with both polar (aqueous) and non-polar (organic) environments, making them crucial in a variety of chemical and biological processes. Surfactants exhibit unique behaviour when dissolved in a solvent, especially in aqueous media. At low concentrations, these molecules tend to arrange themselves at the interface between water and air, reducing the surface tension. However, when their concentration exceeds a critical threshold, known as the critical micelle concentration (*CMC*), these molecules spontaneously form micelles.[1] In these micelles, the hydrophobic tails aggregate inward to avoid water (being hydrophobic), while hydrophilic heads face outward, interacting with the aqueous environment. This self-assembly process is driven by the system's tendency to minimize free energy and is fundamental to many industrial and biological applications.[2–6]

Aqueous–organic mixed solvents play a crucial role in influencing the micellization behaviour of surfactants due to the unique interplay of polar and non--polar interactions in these media. In such systems, the combination of water- and water-soluble organic solvents like alcohol, acetone creates a versatile environment where the solvation properties, hydrophobic effects and surfactant aggregation dynamics can be finely tuned.[7–11]

Ionescu *et al.*[12] studied the development of micelles of CTAB in water––dimethyl sulfoxide (DMSO) mixtures, observing that DMSO has a variable effect on CTAB micellization. Shah *et al.*[10] investigated the influence of methanol on the micellar properties of dodecyltrimethylammonium bromide (DTAB) and found that *CMC* increased with increasing methanol content, suggesting that the addition of organic co-solvents disrupts micelle formation. Niraula *et al.*[13] similarly showed that the *CMC* of SDS rises with methanol content, supporting the general observation that polar organic solvents reduce the feasibility of micelle formation. Bielawska *et al.*[14] explored the effect of short-chain alcohol on CTAB micellization and observed that alcohols significantly alter *CMC* values. Das *et al.*[15] reported that the presence of cosolvents increases the *CMC* and decreases the aggregation number for cationic, anionic and nonionic surfactants.

In the context of acetonitrile (ACN), Misra *et al.*[16] examined CTAB and SDS micellization in ACN–water and tetrahydrofuran (THF)–water mixtures and observed a consistent increase in *CMC* with rising ACN mole fraction. The increase was more pronounced for CTAB than for SDS, indicating stronger disruption of cationic surfactant self-assembly by ACN. Šteflová *et al.*[17] found that low ACN concentration (up to 0.10 by volume fraction) reduces *CMC* of SDS, whereas higher ACN volume fraction increases it, indicating a biphasic effect. Jalali and Gerandaneh[18] observed that the *CMC* of CTAB increases linearly with ACN content due to weakened solvophobic effects in the medium. Ležaić *et al.*[19] further reported a simultaneous rise in *CMC* and decline in aggregation number for CTAB in ACN–water, reflecting reduced micellar stability. Banjare *et al.*[20] confirmed

these trends and showed decreased surface excess and increased minimum area per molecule (A_{min}) in CTAB–ACN–water systems.

These findings are further supported by our recent study[21] that compared the effects of 10 % by volume of DMSO, ACN and 1-propanol on SDS, DTAB and CPC. The data showed that ACN significantly increases the *CMC* and decreases the aggregation number and surface excess concentration (Γ_{max}), indicating reduced micellar compactness and lower interfacial adsorption. The overall trend of co-solvent strength was found to be: 1-propanol > ACN > DMSO in terms of disrupting micellization.

Overall, these studies underscore the pivotal role of solvent polarity and specific interactions in modulating micelle formation and interfacial behaviour of ionic surfactants. In particular, ACN emerges as a moderately polar aprotic solvent that weakens hydrophobic interactions and reduces surfactant packing, thus significantly altering micellization and adsorption dynamics.

Studying both SDS (anionic) and CTAB (cationic) surfactants in ACN––water mixtures is particularly relevant due to their contrasting ionic head groups, which interact differently with polar aprotic co-solvents like acetonitrile. SDS carries a negatively charged sulfate group, while CTAB contains a positively charged quaternary ammonium head. These differences influence not only micelle formation and *CMC* values but also interfacial adsorption, counterion binding and solvation dynamics in mixed solvent environments. A comparative analysis provides insights into how solvent polarity modulates electrostatic and hydrophobic contributions to micellization, enabling a broader understanding of surfactant behaviour in non-aqueous or mixed-phase systems relevant to colloidal formulation, extraction and drug delivery applications.

The wetting behaviour of surfactants is significantly influenced by the composition of the solvent system,[22] as the balance between hydrophilic and hydrophobic interactions dictates surfactant adsorption at interfaces. In mixed solvent systems, such as water–organic mixtures, the presence of co-solvents alters surface tension, interfacial interactions and contact angle, thereby modifying wettability. Polar solvents like short-chain alcohols disrupt the structured hydrogen--bonding network, weakening surfactant adsorption at the solid–liquid interface and increasing the contact angle, leading to reduced spreading.[23]

The objective of this study is to investigate the micellization and surface properties of CTAB and SDS in ACN–water mixed media, focusing on their surface properties and wetting behaviour. By analysing *CMC*, surface tension, contact angle and related parameters, this work aims to provide an understanding of how solvent composition influences surfactant aggregation and wettability. While several earlier studies have examined the micellization behaviour of ionic surfactants in ACN–water mixed solvent systems, including CTAB[16] and SDS,[17] most have focused primarily on micellization behaviour in the bulk phase using

classical techniques such as conductometry or fluorescence. In contrast, the present study incorporates surface and wetting property analysis – especially surface tension and contact angle measurements evaluate the interfacial behaviour of both cationic (CTAB) and anionic (SDS) surfactants in ACN–water mixtures. This dual focus enables the exploration of how co-solvent-modified polarity affects not only micelle formation but also surfactant adsorption and spreading behaviour on a solid surface.

EXPERIMENTAL

Materials

CTAB (99.0 % pure) and SDS (99.0 % pure) were purchased from Loba Chemie Pvt. Ltd., Mumbai, India. These surfactants were used without further purification. They were heated in an oven at 100 °C for 1 h prior to use. Acetonitrile (ACN, 99.0 % pure) was obtained from E. Merk, India. All the solvent mixtures and solutions were prepared in double--distilled water (specific conductance < 0.6 μS cm^{-1} at 298.15 K).

Methods

The surface tension of a freshly prepared solution was measured by an Easydyne K20 force tensiometer (Kruss, Germany) equipped with a du Nouy's ring. The ring was cleaned by dipping it in ethyl alcohol and then heated until red-hot in the blue flame of a Bunsen burner. Double-distilled water was used to calibrate; the value obtained was 72.30 mN m^{-1} at 298.15 K. The temperature was controlled by a circulatory water bath (Orbit, RS10S) with an accuracy of ±0.1 K.

Surface tension measurements and *CMC* determination were conducted for SDS and CTAB solutions. For SDS (0.0004–0.08 M) in distilled water and ACN–water mixtures (0.10, 0.20, 0.40 volume fractions of ACN), a 50 mL vessel was filled with 30 mL of solution. Surface tension was measured using a platinum ring and a tensiometer after stirring and resting for 2 min. Similarly, CTAB (0.0006–0.001 M) solutions were analysed following the same procedure.

The *CMC* was determined from a surface tension (*γ*) *versus* logarithm of surfactant concentration (log *C/M*) plot. The data were fitted with linear regression corresponding to the premicellar region. In the premicellar region, *γ* decreases linearly with increasing log *C/M* as surfactant molecules accumulate at the air/solution interface. Beyond *CMC*, *γ* remains almost constant or changes very slightly. The interaction point of these pre- and post-micellar regions is commonly depicted as CMC.[24]

Contact angles of freshly prepared solutions were measured using a drop shape analyzer (DSA25E, Kruss, Germany) by the sessile drop method on a borosilicate glass surface. For SDS (0.08–0.0004 M) in distilled water and ACN–water mixtures (0.10, 0.20, 0.40 volume fractions of ACN), a 3μL drop was placed at 2.57μL/s and contact angles were recorded from both sides, averaging thirty replicates. The syringe was calibrated and cleaned before use. Similarly, CTAB (0.0006–0.001 M) solutions were analysed following the same procedure. Eight readings were recorded for each case.

RESULTS AND DISCUSSION

Surface tension and surface properties

Surface tension (*γ*) of CTAB and SDS solutions was measured in water, 0.10, 0.20 and 0.40 volume fractions of ACN–water mixed solvent media at 298.15 K.

A graph is plotted between γ and the logarithm of concentration (log C) for each solution, as shown in Fig. 1. The break point of the graph represents *CMC*. The slope of the graph $\partial\gamma/\partial(\log C)$ is utilized to calculate surface properties. One of the surface properties is the maximum surface excess concentration (Γ_{max}) given as:[25]

$$\Gamma_{max} = -\frac{1}{2.303nRT}(\frac{\partial\gamma}{\partial\log C})_{T,p} \tag{1}$$

R (8.314 J mol^{-1} K^{-1}) denotes the gas constant, T indicates the absolute temperature and C indicates the concentration of surfactant. The value of n taken as the constant pre-factor, is assumed to be 2 for the normal ionic surfactant. T is the absolute temperature, C is the concentration of surfactant, ($\partial\gamma/\partial\log C$) is the slope of the γ *versus* log (C/M) plot just below the *CMC* at constant temperature.
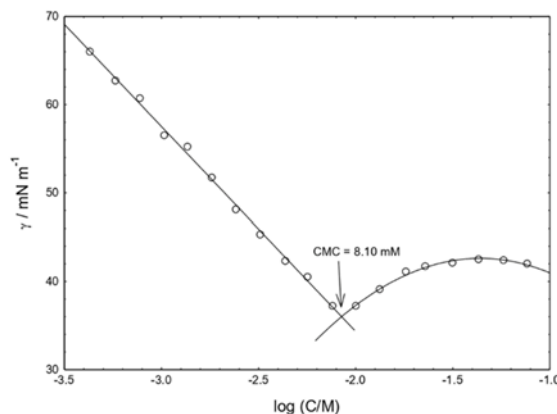
Fig. 1. Plot of surface tension (γ) against the logarithm of SDS concentration (log C/M) in water at 298.15 K; the critical micelle concentration (*CMC*) is indicated by an arrow.

The minimum area per molecule (A_{min}) of surfactant at the air–water interface, *i.e.*, the area. covered by a surfactant molecule on the solution/air interface, is given as:

$$A_{min} = \frac{1}{N_A\Gamma_{max}} \tag{2}$$

where N_A denotes Avogadro number (6.022×10^{23} mol^{-1}).

The surface pressure (π_{CMC}) is a measure of how efficiently a surfactant lowers the surface tension of a solution at *CMC*. It can be calculated using:

$$\pi_{CMC} = \gamma_0 - \gamma_{CMC} \tag{3}$$

where γ_0 and γ_{CMC} are surface tensions (in mN m^{-1}) of solvent and *CMC*, respectively.

A_{min} can be utilized to calculate the packing parameter (P) that predicts the shape of aggregated micelle:[26]

$$P = \frac{V_0}{A_{min} l_C} \quad (4)$$

where V_0 denotes the volume of exclusion per monomer during aggregation, as explained in Tanford's formula:[27] $V_0 = (27.4 + 26.9 n_C)$ Å³ and $l_C = (1.54 + 1.26 n_c)$ Å shows the maximum chain length and n_C denotes the total number of carbon atoms present in the alkyl chain.

Effect of ACN on CMC

The *CMC*, which is the concentration of surfactants at which micelles start to form, is extremely sensitive to solvent composition. In purely aqueous solutions, the hydrophobic effect is the primary driving force for micelle formation, with water molecules tending to "squeeze out" the non-polar tails of surfactants, forcing them to aggregate into micelles to minimize free energy. As ACN is added to water, the solvent becomes less polar and the hydrophobic effect is weakened. This means that surfactants require a higher concentration to reach the point where micelles can form. The *CMC* thus increases with ACN content. This effect is seen in both SDS and CTAB cases, where the *CMC* of SDS and CTAB increases with the increase in volume fraction of ACN.

The effect of ACN addition on the micellization of CTAB has been reported by several studies at 298.15 K, using different analytical techniques. Across all reports, the *CMC* increases with rising ACN content, attributed to the reduced polarity and weakened hydrophobic interactions in the solvent mixture. Misra *et al.*[16] employed spectroscopic and conductometric methods to determine the *CMC* of CTAB in ACN–water mixtures at 298.15 K. The *CMC* increased from 0.42 mM in pure water to 0.78 mM at an ACN mole fraction of 0.141. Jalali and Gerandaneh[18] used conductivity measurements and found the *CMC* to rise from 0.96 mM in water to 1.63 mM at 0.20 volume fraction of ACN and further to 3.19 mM at 0.40 volume fraction of ACN, all measured at 298.15 K. Ležaić *et al.*[19] determined the *CMC* using conductometry and fluorescence techniques, reporting a value of 0.98 mM in pure water and 3.50 mM at 0.40 volume fraction of ACN at 298.15 K. Banjare *et al.*[20] applied surface tension measurements, reporting *CMC* values increasing from 1.0 mM in water to 1.5 mM at 0.005 volume fraction of ACN, 2.5 mM at 0.01 volume fraction of ACN and 3.0 mM at 0.03 volume fraction of ACN. This indicates that the presence of ACN affects the micellization behaviour of CTAB. Similarly, Šteflová *et al.*[17] observed that the *CMC* of SDS increases progressively with higher ACN content, from 4.8 mM at no ACN to 22 mM at 0.35 volume fraction of ACN, indicating reduced micelle stability in ACN-rich environments.

Effect of ACN on surface properties

Figs. 2 and 3 represent combined plots of γ and log C for SDS and CTAB in different volume fractions of ACN–water mixed solvent media at 298.15 K. The regression analysis is provided in Table I. The fits demonstrate good linearity ($r^2 \geq 0.90$), confirming the reliability of the surface tension data. The premicellar slopes derived from the plot of γ against the logarithm of SDS concentration (log C/M) (Table I) provide insight into the efficiency of surfactant adsorption at the air/solution interface prior to micelle formation. In both SDS and CTAB systems, the magnitude of the slope decreased (became less negative) with increasing ACN content. This trend suggests that the presence of ACN reduces the surface activity of the surfactants in the premicellar region, likely due to weaker hydrophobic interactions and decreased interfacial packing efficiency. The steeper slope in pure water indicates stronger adsorption, consistent with the structured hydrogen-bonding network of water supporting micellization. Our group has previously reported similar trends in mixed solvent systems. In a recent study,[24] we demonstrated that the premicellar slope of TX100 decreased systematically with increasing concentrations of methanol, ethanol and 1-propanol, highlighting the weakening of surfactant adsorption and interfacial cohesion in less polar media. *CMC* and surface properties (Γ_{max}, A_{min}, π_{CMC} and P) of SDS and CTAB solutions in water and in 0.10, 0.20 and 0.40 volume fractions of ACN are presented in Tables II and III, respectively.
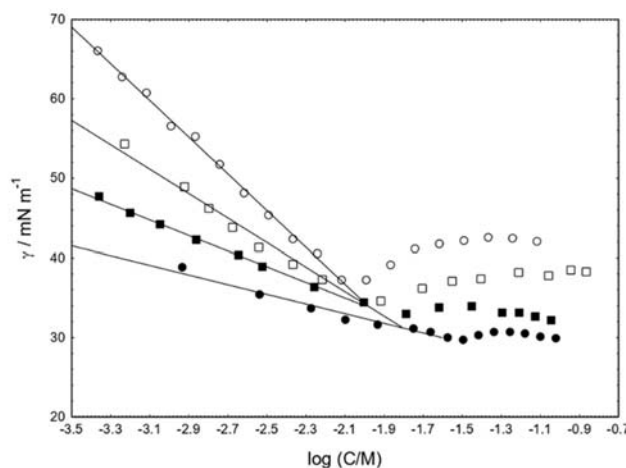
Fig. 2. Plot of surface tension (γ) against the logarithm of SDS concentration (log C/M) in 0.10 (□), 0.20 (■) and 0.40 (●) ACN volume fractions in ACN–water mixtures at 298.15 K.

Surface excess concentration (Γ_{max}) is a measure of how much surfactant accumulates at the surface compared to the bulk solution. In an aqueous solution, surfactants migrate to the air/water interface to minimise the system's free energy.

The surfactant molecules arrange themselves such that the hydrophobic tails are oriented away from the water, while the hydrophilic heads remain in contact with it. The addition of a polar organic solvent into aqueous solutions of surfactants significantly alters the surface and interfacial properties, including Γ_{max}, A_{min}, π_{CMC} and P. The effect primarily arises from its ability to reduce the overall polarity of the solvent and disrupt the structured hydrogen-bonding network of water.
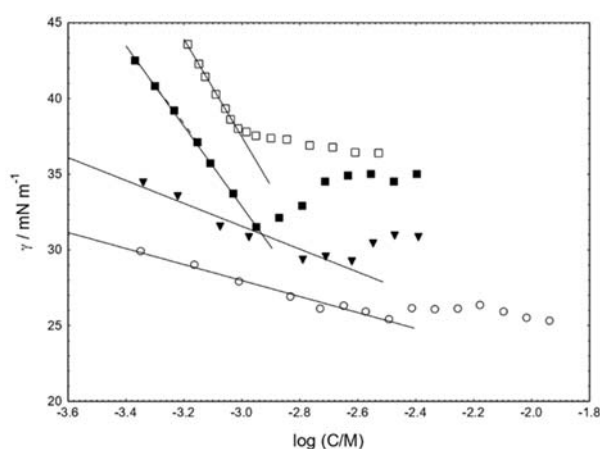
Fig. 3. Plot of surface tension (γ) against the logarithm of CTAB concentration (log C/M) in water (□) and 0.10 (■), 0.20 (▼) and 0.40 (o) ACN volume fractions in ACN–water mixtures at 298.15 K.

TABLE I. Regression summary of the plot of surface tension (γ) against the logarithm of concentration (log C/M) related to Figs. 2 and 3

Volume fraction of ACN	$(\partial\gamma/\partial\log C)$	r^2
SDS		
0.00	-23.2	0.99
0.10	-15.4	0.97
0.20	-9.79	0.99
CTAB		
0.00	-32.3	0.99
0.10	-26.5	0.99
0.20	-7.56	0.94
0.40	-5.29	0.98
0.00	-32.3	0.99

ACN, being less polar than water, interacts more favourably with the hydrophobic tails of surfactants, reducing the driving force for their accumulation at the interface. This weakens the hydrophobic effect, resulting in fewer surfactant

TABLE II. CMC by surface tension (ST) and contact angle (CA) methods; Γ_{max}, A_{min}, π_{CMC} and P of SDS in different volume fractions of ACN at 298.15 K

Volume fraction of ACN	CMC (mM)		$\Gamma_{max} \times 10^6$ mol m^{-2}	A_{min} Å molecule^{-1}	π_{CMC} mN m^{-1}	P
	ST	CA				
0.00	8.10	7.90	2.02	82.07	33.97	0.26
0.10	12.09	12.12	1.34	123.11	25.50	0.17
0.20	16.32	15.33	0.85	193.66	15.20	0.10
0.40	31.99	32.42	0.53	312.31	8.30	0.07

TABLE III. CMC by surface tension (ST) and contact angle (CA) methods, Γ_{max}, A_{min}, π_{CMC} and P of CTAB in different volume fractions of ACN at 298.15 K

Volume fraction of ACN	CMC (mM)		$\Gamma_{max} \times 10^6$ mol m^{-2}	A_{min} Å molecule^{-1}	π_{CMC} mN m^{-1}	P
	ST	CA				
0.00	0.96	0.89	2.82	58.69	37.02	0.35
0.10	1.12	1.01	2.32	71.74	34.60	0.29
0.20	1.63	1.72	0.66	250.78	32.96	0.08
0.40	3.19	3.22	0.46	358.40	29.68	0.05

molecules migrating to the interface. Consequently, the surface excess concentration decreases as the ACN content increases. As the ACN content in the solution increases, the interactions between surfactant head groups and the solvent become weaker. ACN's lower polarity compared to water reduces the effectiveness of the hydrophilic head group's interaction with the surrounding solvent molecules. This leads to less efficient packing of surfactant molecules at the surface, resulting in a larger minimum area per molecule A_{min}. The larger value of A_{min} indicates that surfactant molecules are spaced farther apart at the interface in ACN-rich mixtures than in purely aqueous solutions. Surface pressure (π_{CMC}) represents the pressure exerted by surfactants at the interface once micelles start forming in the bulk solution. A higher π_{CMC} value indicates stronger surface activity of the surfactant because it means that the surfactant has significantly reduced the surface tension. It is seen from the data (Tables II and III) that the presence of ACN decreases π_{CMC} values for both SDS and CTAB. The packing parameter (P) describes the morphology of micelles. $P \approx 1/3$ corresponds to spherical micelles. The lower values of P in the presence of ACN indicate that the size of the micelles changes from spherical to worm-like structures. To contextualize the present findings, surface properties such as Γ_{max} and A_{min} for CTAB and SDS were compared with literature values in binary solvent systems. Recently, our group observed that the addition of co-solvents (DMSO, ACN, 1-propanol) to surfactants SDS, DTAB and CPC reduced adsorption (lower Γ_{max}), increased molecular packing area (A_{min}) and decreased surface pressure (π_{CMC}). 1-Propanol showed the strongest impact due to its amphiphilic nature and its disruption of water's hydrogen bonding network.[21] The surface properties of Triton X-100 (TX100) change significantly with increasing alcohol volume

fractions. π_{CMC} decreases, Γ_{max} declines and A_{min} increases, reflecting reduced adsorption efficiency and disrupted surfactant packing due to alcohol–surfactant interactions and weakened hydrophobic effects.[24] The study reveals that adding 2-propanol to surfactant solutions significantly reduces γ, increases the *CMC* and alters adsorption properties by decreasing Γ_{max} while increasing A_{min}.[23] The surface properties of sodium dodecyl sulfate (SDS) in water–acetamide mixtures show that the limiting surface tension at the *CMC* remains constant regardless of acetamide concentration. Γ_{max} decreases with increasing acetamide content, stabilizing beyond 30 % acetamide due to changes in solvophobicity and mixed water–acetamide structures.[28]

Contact angle

The spreading of a liquid on a solid surface is known as wettability, which is quantitatively measured by the contact angle (θ). Geometrically, contact angle (θ) is defined as the angle formed between the liquid drop and the solid surface where the solid, liquid and gas phases intersect each other. The Young's equation is commonly used to establish the relationship between θ and γ:

$$\cos\theta = \frac{\gamma_{S-V} - \gamma_{S-L}}{\gamma_{L-V}} \quad (5)$$

where γ_{S-V} is the solid/vapor interfacial tension, γ_{S-L} is the solid/liquid interfacial tension and γ_{L-V} is the liquid/vapor interfacial tension.

The contact angle (θ) *versus* concentration of SDS and CTAB in different volume fractions of ACN–water mixtures at 298.15 K is represented in Figs. 4 and 5. The obtained results showed that θ increases with an increase in surfactant concentration (for surfactant concentrations smaller than *CMC*) and then decreases
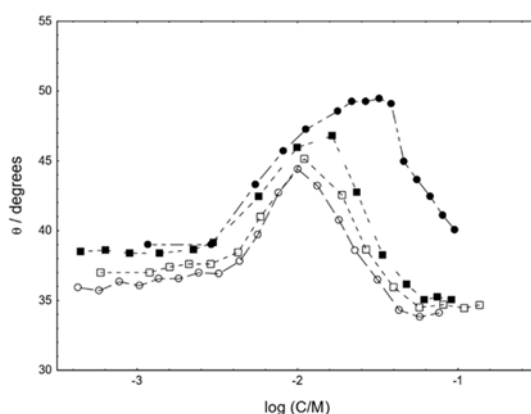
Fig. 4. Plot of contact angle (θ) against the logarithm of SDS concentration (log *C/M*) in water (o) and 0.10 (□), 0.20 (■) and 0.40 (●) ACN volume fractions of ACN–water mixtures at 298.15 K.

(for surfactant concentrations higher than *CMC*), forming one maximum (peak); this maximum corresponds to the value of the *CMC*.
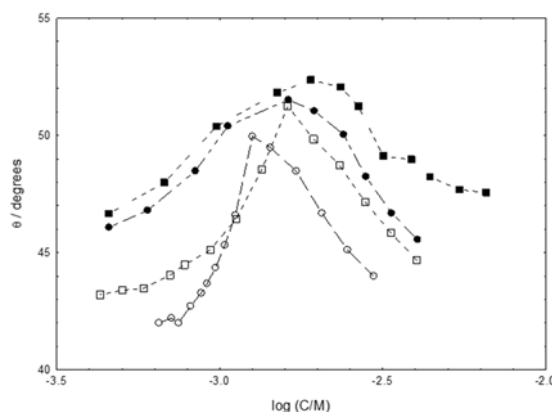
Fig. 5. Plot of contact angle (θ) against the logarithm of CTAB concentration (log *C/M*) in water (o) and 0.10 (□), 0.20 (■) and 0.40 (●) ACN volume fractions of ACN–water mixtures at 298.15 K.

The Lucassen–Reynolds[29] equation describes the relationship between surface excess concentrations at three interfaces and their respective interfacial tensions, expressed as:

$$\frac{\Gamma_{S-V} - \Gamma_{S-L}}{\Gamma_{L-V}} = \frac{d(\gamma_{S-V} - \gamma_{S-L})}{d\gamma_{L-V}} = \frac{d\gamma_{S-G} \cos\theta}{d\gamma_{L-G}} \tag{6}$$

Assuming $\Gamma_{S-V} = 0$, the ratio of Γ_{S-L} to Γ_{L-V} can be determined from the slope of a plot of $d\gamma_{L-G} \cos\theta$ (also referred to as the adhesion tension, A_T) against $d\gamma_{L-G}$.

The work of adhesion (W_A) is defined as the reversible work required to separate a unit area of liquid from a solid surface. It quantifies the interactive forces between the solid and liquid phases and can be determined from the contact angle using the following equation:

$$W_A = \gamma_{L-G}(1 + \cos\theta) \tag{7}$$

For $\theta = 0°$, $W_A = 2\gamma_{L-G}$, indicating that the attraction between the liquid and solid is at least as strong as the cohesive forces within the liquid itself.[22]

In this study, the wettability of CTAB and SDS on a hydrophilic glass surface was evaluated by measuring the contact angle in various volume fractions of acetonitrile.

Fig. 6 represents the variation of the work of adhesion with the concentration of CTAB in the premicellar region in different volume fractions of ACN. The trend clearly demonstrates that increasing ACN volume fractions results in enhancement

of surfactant adsorption, thereby increasing the interactive forces between the liquid and solid surfaces. The trend is more pronounced for SDS, highlighting its stronger affinity for the glass surface compared to CTAB.
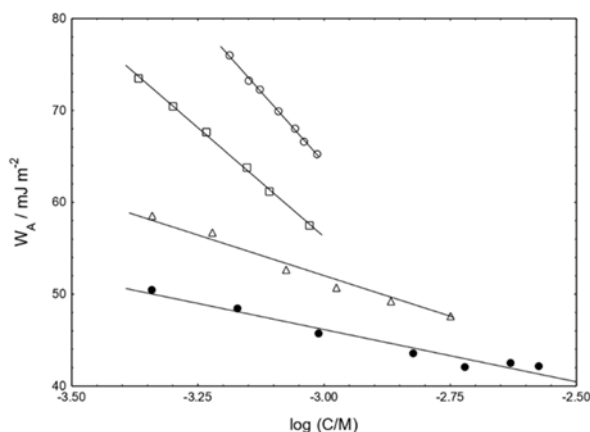
Fig. 6. Variation of W_A with concentration of CTAB in water (o) and several volume fractions of ACN (0.10 (□), 0.20 (Δ) and 0.40 (●)).

Fig. 7 illustrates the relationship between adhesion tension and surface tension for CTAB solutions containing different volume fractions of ACN. It shows a linear relationship between adhesion tension and surface tension for CTAB in all volume fractions of ACN. The evaluated slopes are all positive (+0.83 in water) and slightly increase with volume fractions of ACN, indicating unequal adsorption at the solid/liquid and liquid/gas interfaces. Similar observations were found in our previous study.[23]
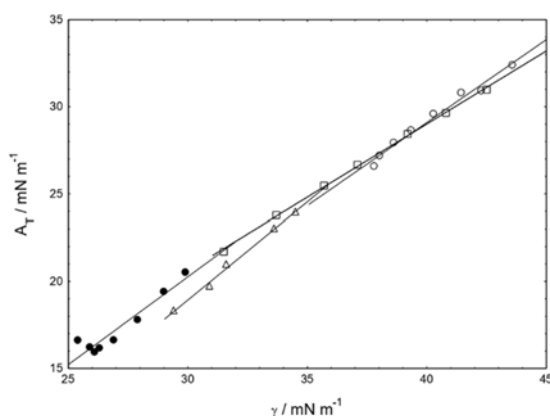

Fig. 7. Variation of A_T with γ of CTAB in water (o) and several volume fractions of ACN (0.10 (□), 0.20 (Δ) and 0.40 (●)).

CONCLUSION

In this study we elucidated how solvent polarity modulates the interfacial and self-assembly behaviour of anionic (SDS) and cationic (CTAB) surfactants in 0.10, 0.20 and 0.40 volume fractions of acetonitrile–water (ACN–water) mixtures at 298.15 K. By measuring surface tension and contact angles, we showed that the presence of ACN systematically increases the *CMC* and reduces the surface excess concentration ($\Gamma_{\max}$), while enlarging the minimum area per molecule ($A_{\min}$), lowering the micellar surface pressure (π_{CMC}) and the packing parameter (*P*). These trends reflect the weakening of hydrophobic and electrostatic interactions in less-polar media, leading to looser packing of surfactant molecules. The contact angle data reveal that higher ACN volume fraction produces larger θ values on borosilicate glass, indicating diminished wettability and weaker surfactant adsorption at the solid–liquid interface. Importantly, *CMC* values derived from contact angle measurements align with those obtained from surface tension data, confirming the reliability of the dual-method approach. Overall, these findings show that adjusting the acetonitrile content in the solvent directly influences surfactant adsorption, wetting and aggregation behaviour. The comparative analysis of SDS and CTAB also suggests that anionic and cationic surfactants respond differently to polarity changes, with SDS showing larger shifts in contact angle, hinting at differing adsorption mechanisms. Future work could extend this approach to other co-solvents, explore the influence of temperature or ionic strength and examine a wider range of substrates to build a more general framework for controlling surfactant-mediated processes.

ИЗВОД

УПОРЕДНА СТУДИЈА МИЦЕЛИЗАЦИЈЕ И ПОВРШИНСКИХ СВОЈСТАВА КАТЈОНСКИХ И АНЈОНСКИХ СУРФАКТАНАТА У МЕШАНОМ РАСТВАРАЧУ АЦЕТОНИТРИЛ–ВОДА

SUJIT KUMAR SHAH, SANDESH KARKI и AJAYA BHATTARAI

Department of Chemistry, Mahendra Morang Adarsh Multiple Campus, Tribhuvan University, Biratnagar, Nepal

Спроведена је упоредна студија ради испитивања способности мицелизације, површинских својстава и квасивости катјонског сурфактаната цетилтриметиламонијум-бромида (CTAB) и анјонског сурфактаната натријум-додецил-сулфата (SDS) у мешаном растварачу ацетонитрил–вода (ACN–вода). Мерења површинског напона и контактног угла извршена су у чистој води и смешама ACN-вода (0,10, 0,20 и 0,40 запреминских удела ACN) на 298,15 K ради одређивања критичне мицеларне концентрације (*CMC*), површинског вишка концентрације ($\Gamma_{\max}$), минималне површине по молекулу ($A_{\min}$), мицеларног површинског притиска (π_{CMC}) и параметра паковања (*P*). Мерења контактног угла коришћена су за процену квасивости на површинама боросиликатног стакла. Резултати показују да повећање садржаја ACN доводи до повећања *CMC*, што указује на смањену мицелизацију у мање поларним срединама. Површински вишак концентрације се смањује са вишим фракцијама ACN, док се минимална површина по молекулу пове-

ћава, што указује на лабавије молекулско паковање на граници ваздух/раствор. Мерења контактног угла показују смањење квасивости са вишим садржајем ACN, што значи побољшану адсорпцију сурфактанта на граници чврста супстанца–течност. Поред тога, мицеларни површински притисак и параметар паковања опадају са повећањем концентрације ACN. Ови резултати истичу критичну улогу састава растварача у модификовању агрегације сурфактанта и понашања на граници фаза.

REFERENCES

1. M. J. Rosen, J. T. Kunjappu, *Surfactants and Interfacial Phenomena*, 4th ed., Wiley, New York, 2012, pp. 1–33 (https://doi.org/10.1002/0471670561)
2. M. E. Jiménez-Castañeda, D. I. Medina, *Water* **9** (2017) 235 (https://doi.org/10.3390/w9040235)
3. M. X. Gao, C. F. Liu, Z. L. Wu, Q. L. Zeng, X. X. Yang, W. B. Wu, Y. F. Li, C. Z. Huang, *Chem. Comm.* **49** (2013) 8015 (https://doi.org/10.1039/C3CC44624G)
4. T. F. Tadros, *An Introduction to Surfactants*, De Gruyter, Berlin, 2014, pp. 179–220 (https://doi.org/10.1515/9783110312133.179)
5. T. Wang, D. Chang, D. Huang, Z. Liu, Y. Wu, H. Liu, H. Yuan, Y. Jiang, *Appl. Microbiol. Biotechnol.* **105** (2021) 7619 (https://doi.org/10.1007/s00253-021-11602-6)
6. I. Kralova, J. Sjöblom, *J. Dispers. Sci. Technol.* **30** (2009) 1363 (https://doi.org/10.1080/01932690902735561)
7. S. K. Shah, A. Bhattarai, *J. Chem.* **2020** (2020) 4653092 (https://doi.org/10.1155/2020/4653092)
8. H. A. Bhuiyan, J. M. Khan, M. R. Islam, S. Rana, A. Ahmad, M. A. Hoque, M. M. Rahman, S. E. Kabir, *Int. J. Biol. Macromol.* **222** (2022) 181 (https://doi.org/10.1016/j.ijbiomac.2022.09.169)
9. S. K. Shah, S. K. Chatterjee, A. Bhattarai, *J. Chem.* **2016** (2016) 2176769 (https://doi.org/10.1155/2016/2176769)
10. S. K. Shah, S. K. Chatterjee, A. Bhattarai, *J. Surfactants Deterg.* **19** (2016) 201 (https://doi.org/10.1007/s11743-015-1755-x)
11. Y. Ghimire, S. Amatya, S. K. Shah, A. Bhattarai, *SN. Appl. Sci.* **2** (2020) 1295 (https://doi.org/10.1007/s42452-020-3036-1)
12. L. G. Ionescu, T. Tokuhiro, B. J. Czerniawski, E. S. Smith, in *Solution Chemistry of Surfactants*, K. L. Mittal, Ed., Plenum Press, New York, 1979, p. 487 (https://doi.org/10.1007/978-1-4615-7880-2_24)
13. T. P. Niraula, S. K. Shah, S. K. Chatterjee, A. Bhattarai, *Karbala Int. J. Mod. Sci.* **4** (2018) 26 (https://doi.org/10.1016/j.kijoms.2017.10.004)
14. M. Bielawska, A. Chodzińska, B. Jańczuk, A. Zdziennicka, *Colloids Surfaces, A* **424** (2013) 81 (https://doi.org/10.1016/j.colsurfa.2013.02.017)
15. S. Das, S. Mondal, S. Ghosh, *J. Chem. Eng. Data* **58** (2013) 2586 (https://doi.org/10.1021/je4004788)
16. P. K. Misra, B. K. Mishra, G. B. Behera, *Colloids Surfaces* **57** (1991) 1 (https://doi.org/10.1016/0166-6622(91)80175-N)
17. J. Šteflová, M. Štefl, S. Walz, M. Knop, O. Trapp, *Electrophoresis* **37** (2016) 1287 (https://doi.org/10.1002/elps.201500553)

18. F. Jalali, A. Gerandaneh, *J. Dispers. Sci. Technol.* **32** (2011) 659 (https://doi.org/10.1080/01932691003800049)
19. A. J. Ležaić, N. Pejić, J. Goronja, L. Pavun, D. Đikanović, A. Malenović, *Maced. J. Chem. Chem. Eng.* **40** (2021) 277 (https://doi.org/10.20450/mjcce.2021.2394)
20. R. K. Banjare, M. K. Banjare, S. Panda, *J. Solution Chem.* **49** (2020) 34 (https://doi.org/10.1007/s10953-019-00937-4)
21. S. K. Shah, A. Giri, S. Adhikari, A. Bhattarai, *Tenside Surfactants, Detergents* **62** (2025) 132 (https://doi.org/10.1515/tsd-2024-2642)
22. N. R. Biswal, S. Paria, *Ind. Eng. Chem. Res.* **51** (2012) 10172 (https://doi.org/10.1021/ie301198k)
23. S. K. Shah, P. K. Das, A. Bhattarai, *Heliyon* **11** (2025) e42352 (https://doi.org/10.1016/j.heliyon.2025.e42352)
24. S. K. Shah, R. M. Leblanc, A. Bhattarai, *Results Chem.* **15** (2025) 102262 (https://doi.org/10.1016/j.rechem.2025.102262)
25. K. M. Sachin, S. A. Karpe, M. Singh, A. Bhattarai, *Heliyon* **5** (2019) e01510 (https://doi.org/10.1016/j.heliyon.2019.e01510)
26. R. A. Khalil, A. H. A. Zarari, *Appl. Surf. Sci.* **318** (2014) 85 (https://doi.org/10.1016/j.apsusc.2014.01.046)
27. C. Tanford, *The hydrophobic effect: formation of micelles and biological membranes*, J. Wiley & Sons, 1980
28. D. Das, K. Ismail, *J. Coll. Interface Sci.* **327** (2008) 198 (https://doi.org/10.1016/j.jcis.2008.07.045)
29. E. H. Lucassen-Reynders, *J. Phys. Chem.* **67** (1963) 969 (https://doi.org/10.1021/j100799a005).

A CFD investigation of the performance of stirred tanks

KAMLA YOUCEF[1]*, ZIED DRISS[2], MOHAMMED FOUKRACH[1], SERGIO ROSA[3]
and TOUHAMI BAKI[4]

[1]*Laboratory of Mechanics and Energy, Faculty of Technology, University Hassiba Ben Bouali of Chlef (UHBC), Algeria,* [2]*Laboratory of Electro-Mechanic Systems (LASEM), National School of Engineers of Sfax (ENIS), University of Sfax (US), Tunisia,* [3]*Polytechnic Institute of Bragança (IPB), Santa Apolonia Campus, Portugal and* [4]*Mechanical Faculty, Gaseous Fuels and Environment Laboratory, University of Sciences and Technology of Oran Mohamed Boudiaf (USTO-MB), BP 1505, El-M'Naouer, Oran 31000, Algeria*

Abstract: Rushton turbine was employed in this study to numerically analyze the fluid flow it generates within a stirred tank. The topology of the resulting flow was found to be strongly dependent on several parameters, including the geometric configurations of the system and the properties of the moving fluids. The governing equations, based on the k–ε model, were solved using the finite volume method. Velocity field profiles, streamlines and vortex sizes were analyzed for several geometries, varying the number of blades from 6 to 12 and others. A comparison was also conducted to evaluate the effect of the number of stirring mobiles used to mix the fluid (single stage, two stages and three stages), as well as the influence of the spacing ratio between the different stirrers. Finally, our numerical simulation procedure was validated through comparing the results obtained with experimental work available in the literature, showing good agreement between the different approaches.

Keywords: Rushton turbine; turbulent flow field; power number; mixing; simulation.

INTRODUCTION

Mechanical agitation is a process used in many industrial sectors; its field of application is extremely wide. The choice of the stirring system depends on the operation to be performed (*e.g.*, homogenization, heat transfer, dispersion of a gaseous phase in a liquid or emulsion, *etc*.). For this reason, many researchers have focused on optimizing mixing processes and reducing energy consumption. By combining experimental studies and numerical modeling, they seek to improve

---

1369

mixing performance while limiting energy consumption, an essential aspect for ensuring the sustainability of industrial processes.

The aim of this work is to improve the mixing efficiency of a tank agitated by a Rushton turbine by modifying important geometric parameters, such as the number of blades and the spacing between impellers. The objective is to identify the most effective configuration that promotes vortex formation without disturbing the free surface, while significantly reducing energy consumption compared to the standard geometry.

As shown in the study by Driss,[1] the inclination angle of the blades significantly affects energy consumption, with lower angles resulting in reduced power numbers. These results provide clear evidence that mixers which generate a mixed flow (inclined blades: 45, 75 and 60°) consume less energy than mixers that generate a radial flow (90°), which can be explained by the character of the fluid generated by the mobile and the contact surface between the stirred system and the fluid. According to investigations conducted by Li *et al.* and Cui *et al.*,[2,3] the effect of blade pitch on the recirculation zone structure and power consumption was examined, revealing that power consumption increases as the blade pitch angle becomes larger. As reported by Jaszczur *et al.*,[4] an experimental and numerical study analyzed the effect of stirrer mobile design on mixing efficiency. The analysis was mainly based on the distribution of water in the stirred tank. Three configurations were studied: one with a tank fitted with a six-bladed Rushton turbine, and the other two mixers designed as scaled-down versions of a standard industrial mixer. In the numerical study by Yang,[5] the geometry of a two--blade stirrer was examined for its impact on flow distribution and power requirements required for mixing an incompressible Newtonian fluid in the laminar regime. The results showed that the new shapes of stirrers exhibit characteristics similar to turbines, generating not only tangential but also increased axial velocities, which lead to the formation of secondary flows around the blades. In another simulation by Liangchao *et al.*,[6] the hydrodynamic characteristics of the fluid in a tank stirred by a Rushton turbine in the laminar regime were investigated. It was found that the power number decreases when the impeller is larger. Furthermore, in a baffled tank with a small impeller, the power number was almost identical to that in a tank without baffles. As shown in the experimental study conducted by Kordas *et al.*,[7] the influence of a new stirrer on mixing time was assessed. It was found that the type of motion (rotary or reciprocating) significantly affected mixing time and energy consumption. The geometry of an anchor-type stirrer was also analyzed with respect to mixing improvement. In a comparative study by Ameur *et al.* and Kamla *et al.*,[8,9] three modified impeller geometries were evaluated to improve fluid circulation throughout the tank, particularly in the lower part. The proposed configurations were also aimed at minimizing energy consumption. In the study carried out by Dang *et al.*,[10] the geometry of a two-blade stirrer was

analyzed using numerical simulation to determine its effect on flow distribution and the power required to mix an incompressible Newtonian fluid in the laminar regime. The stirrer shapes demonstrated turbine-like behavior, enhancing both tangential and axial velocities, leading to the formation of secondary flows around the blades. As reported in the experiments by Youcefi,[11] the mass transfer performance of the cup blade mixer was evaluated and found to be superior to that of the 45° blade and the Rushton turbine. Additionally, the design of this new stirrer was shown to enable efficient mixing in multiphase flow systems. In the studies by Bonnot *et al.*, Hachemi and Yang,[12–14] the effects of rotation mode, impeller inner diameter, gas flow rate and viscosity were examined in a vessel agitated by a Rushton and anchor-type coaxial stirrer. The findings demonstrated that the co-rotation mode provided an advantage in reducing energy consumption compared to counter-rotation. According to research using particle image velocimetry (PIV) by Mortensen *et al.*,[15] the effect of stirrer slot width on flow and velocity profiles in a key mixing zone was explored. The study showed that flow decreases as slot width increases, and the velocity profile and reflux proportion vary with the number of flows, an essential parameter for describing the hydrodynamics of batch SMR. Finally, the studies summarized in the following table. Mahmoudi *et al.* and Rutherford[16,17] investigated the effect of wheel clearance on the transition between flow regimes in single and dual Rushton turbine systems. It was also found that different combinations of *C1* and *C2* values led to parallel, merging, and diverging flow regimes. In this work, *C1* represents the distance between the tank bottom and the impeller, while *C2* represents the distance between the impellers. A Rushton-type impeller was used in a tank with a diameter *T* (Table I).

TABLE I. Summary of the range of clearances corresponding to steady flow development in the literature

Flow model	Space between the agitators	Experimental date
Parallel flow	$C1 > 0.19T$, $\Delta C > 0.4T$	1992.[16]
	$C1 > 0.20T$, $\Delta C > 0.385T$	1996.[17]
	$C2 > 0.415T$	
Merging flow	$C1 > 0.17T$, $\Delta C < 0.34T$	1992.[16]
	$C1 > 0.20T$, $\Delta C < 0.385T$	1996.[17]
diverging flow	$C1 < 0.17 – 0.19T$	1992.[16]
	$C1 < 0.17T$, $\Delta C > 0.385T$	1996.[17]
Single loop flow pattern	$C1 < 0.167T$	1997.[18]
	$C1 < 0.15 – 0.20T$	1992.[19]
		2009.[20]

EXPERIMENTAL

Mathematical formulation

The basic equations used in the simulation of stirred vessels are the continuity equation and the momentum equations (Navier–Stokes). These equations describe the flow behavior of a fluid in the vessel and are used to analyze the hydrodynamics generated by the stirrer.

Continuity equation (conservation of mass). The continuity equation expresses the conservation of mass in an incompressible flow:

$$\frac{\partial \rho}{\partial t} + \frac{\partial}{\partial x}(\rho u) + \frac{\partial}{\partial y}(\rho v) + \frac{\partial}{\partial z}(\rho w) = 0 \tag{1}$$

Momentum equation. The Navier–Stokes equations describe the conservation of momentum taking into account the forces acting on the fluid (such as viscous forces, pressure and external forces). The governing equation is given as follows:

$$\rho(u\frac{\partial u}{\partial x} + v\frac{\partial u}{\partial y} + w\frac{\partial u}{\partial z}) = -\frac{\partial p}{\partial x} + \mu(u\frac{\partial^2 u}{\partial x^2} + v\frac{\partial^2 u}{\partial y^2} + w\frac{\partial^2 u}{\partial z^2}) \tag{2}$$

$$\rho(u\frac{\partial v}{\partial x} + v\frac{\partial v}{\partial y} + w\frac{\partial v}{\partial z}) = -\frac{\partial p}{\partial y} + \mu(u\frac{\partial^2 v}{\partial x^2} + v\frac{\partial^2 v}{\partial y^2} + w\frac{\partial^2 v}{\partial z^2}) \tag{3}$$

$$\rho(u\frac{\partial w}{\partial x} + v\frac{\partial w}{\partial y} + w\frac{\partial w}{\partial z}) = -\frac{\partial p}{\partial z} + \mu(u\frac{\partial^2 w}{\partial x^2} + v\frac{\partial^2 w}{\partial y^2} + w\frac{\partial^2 w}{\partial z^2}) \tag{4}$$

Power number. The power number, also known as the power coefficient, is a dimensionless parameter that characterizes the energy consumption of a stirrer in a stirred tank. It is defined by the following equation:

$$Np = \frac{P}{\rho N^3 D^5} \tag{5}$$

where *P* denotes the power consumption of the stirred system, which can be determined using the viscous dissipation function and is given by the following formula:

$$P = \mu \iiint Q_v \mathrm{d}x\mathrm{d}y\mathrm{d}z \tag{6}$$

where Q_v represents the viscous dissipation function, which is calculated based on the fluid flow velocities (*u*, *v*, *w*) inside the stirred vessel. The volumetric flow rate (*Qv*) used in this study is based on the formulation presented by Hadjeb *et al.*[21] The Reynolds number (Re) is a dimensionless parameter used to determine the flow regime (laminar, transitional or turbulent) in a stirred tank. It is defined by the formula:

$$\mathrm{Re} = \frac{ND^2\rho}{\mu} \tag{7}$$

Mixing system description

Fig. 1 shows the geometric configuration of the stirring system, which consists of a flat-bottomed cylindrical tank of diameter *D* and height *H*. The mechanical stirring system is equipped with a six-bladed Rushton turbine mounted on a disk of diameter *d*. To avoid contact with the tank bottom, the stirrer is positioned at a distance *c* and mounted on a central cylindrical shaft of diameter *da*. The fluid used in this study is water at 25 °C, which behaves as a Newtonian fluid with a density of $\rho = 997$ kg m^{-3} and a dynamic viscosity of $\mu = 8.9\times10^{-4}$ Pa s. In

this study, the effect of the spacing between the stirring mobiles was analysed. The different spacing configurations used are shown in Fig. 1 and Table II.
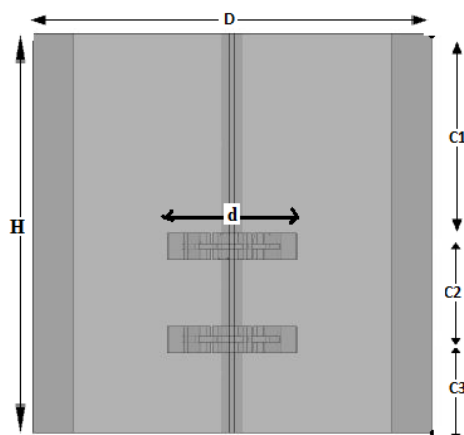

Fig. 1. Geometric configuration.

TABLE II. The spacing *C* values between stirrers for different geometries

Case	*C1*	*C2*	*C3*
Case 1	0.45*D*	0.70*D*	0.35*D*
Case 2	0.80*D*	0.35*D*	0.35*D*
Case 3	0.45*D*	0.35*D*	0.70*D*
Standard turbine	–	–	0.50*D*

The multiple reference frame (MRF) approach was used in this part of this research. It is commonly used to simulate flows in mechanically stirred tanks, as demonstrated by the works of Dabiri *et al.*[22] and more recently by Reid *et al.*[23] It allows us to model agitator motion without the need for a moving mesh. The principle behind the MRF method is to divide the simulation domain into two distinct zones. A moving (rotating) zone corresponding to the region around the stirrer, where the Navier–Stokes equations are solved in a reference frame rotating at the same speed as the stirrer system and a fixed (static) zone representing the rest of the tank, where the equations are solved in a stationary reference frame. At the interfaces between these zones, coupling conditions ensure the continuity of physical quantities such as velocity and pressure. This approach is particularly well suited for steady-state and turbulent studies and provides a good compromise between accuracy and computational efficiency.

RESULTS AND DISCUSSION

In order to evaluate the simulation method used, we relied on the experimental work of Wu *et al.*[24] and Driss *et al.*[25] These studies served as a reference and it should be noted that the same geometric conditions, as well as the same fluid, were reproduced during the simulation, using a six-blade Rushton turbine with vertical baffles symmetrically positioned to enhance mixing performance. The numerical results obtained for tangential velocity (Fig. 2) and radial velocity (Fig. 3) were compared with experimental data from the literature and showed satisfactory agreement.

The dimensionless quantities used in these comparisons are defined as follows: Vt^* is the dimensionless tangential velocity, Vx^* is the dimensionless axial velocity, Vr^* is the dimensionless radial velocity and Z^* is the dimensionless liquid height in the tank.
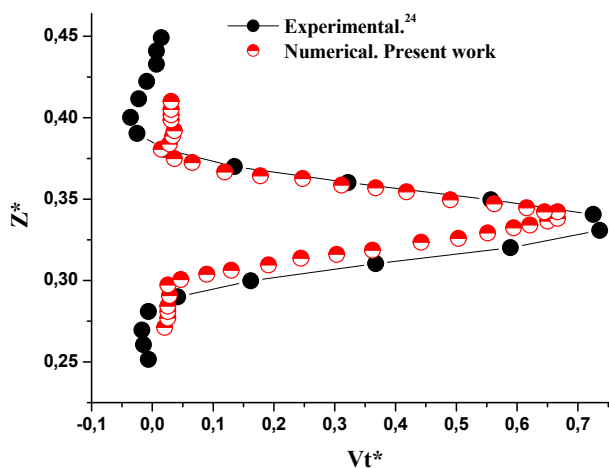
Fig. 2. Tangential velocities (Re = 40000).
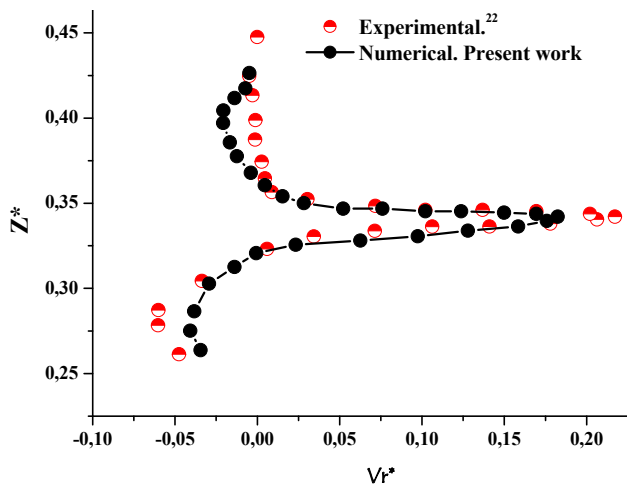
Fig. 3. Radial velocities (Re = 17000).

Effect of the number of blades on the flow generated

Figs. 4 and 5 show axial velocity profiles for different numbers of blades. It can be observed that the velocities are more intense when the agitator has a high number of blades (*e.g.*, 12 blades). In this case, the fluid motion is more intense, resulting in instability of the free fluid surface. On the other hand, for a 3-blade

Rushton turbine, the axial velocity in the free fluid surface is null, which explains why the number of blades has a positive influence on the stream flow. Negative velocity signs indicate the presence of vortices above and below the impeller.
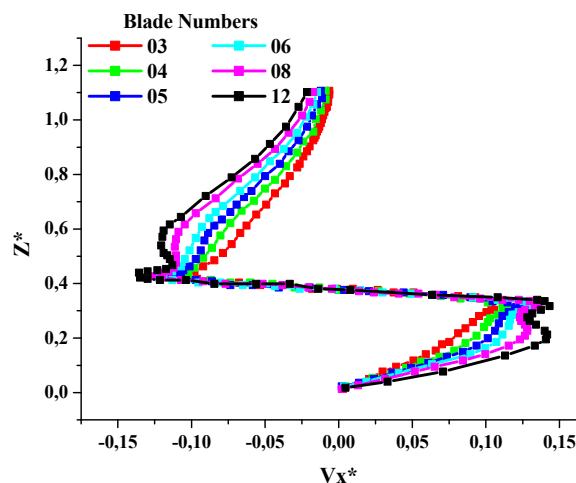
Fig. 4. Axial velocities for different numbers of blades (Re = 40000, $X^* = 0.185$).
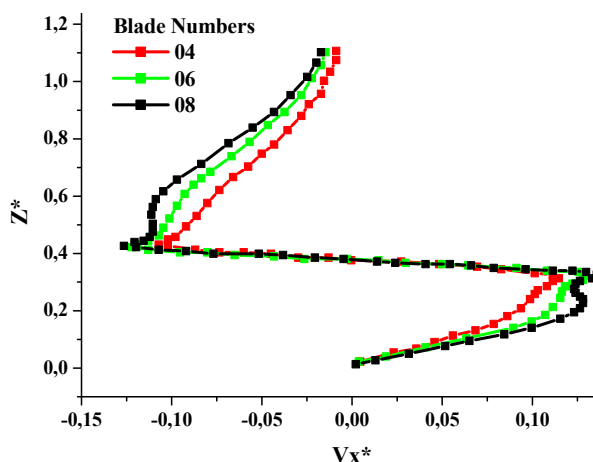
Fig. 5. Axial velocities for different numbers of blades (Re = 40000, $X^* = 0.185$).

Fig. 6 shows the tangential velocities for different numbers of blades. At the bottom of the tank, the fluid elements stagnate due to the wall effect at this location, which reduces the development of the flow. On the other hand, at the agitator, these velocities reach maximum values due to the increase in the number of blades, which leads to an increase in the discharge flow generated by the agitator blade. These phenomena are also illustrated in Fig. 7.
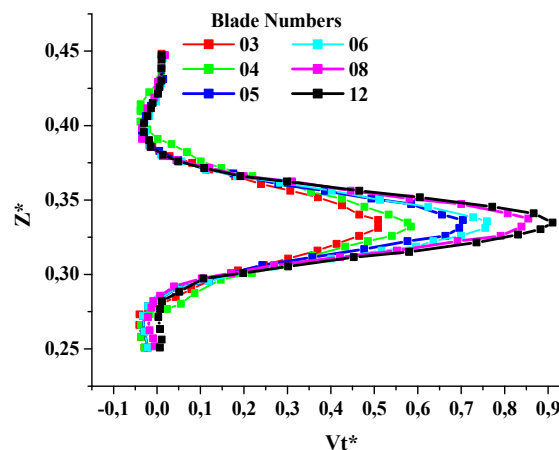
Fig. 6. Tangential velocities for different numbers of blades (Re = 40000, X^* = 0.185, baffled tank).
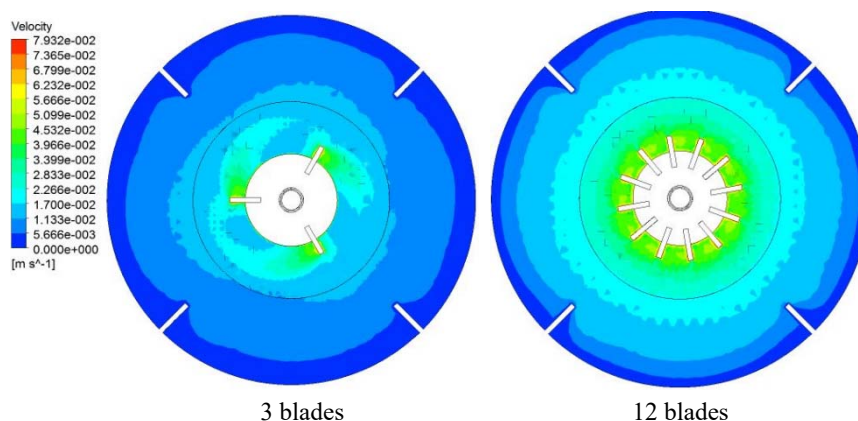
Fig. 7. Velocity champs (Re = 40000, baffled tank).

As presented in Table III, the numerically calculated power number for a six-bladed Rushton-type stirrer is 0.82 for a six-bladed Rushton-type stirrer with an unbaffled vessel and 6.72 with a baffled vessel. These results were compared with those found numerically and experimentally in the literature. The values are almost identical to those obtained in other experimental and numerical studies, making it possible to determine the effect of the number of blades on energy consumption.

Fig. 8 shows that the power number increases with increase of the number of blades, which can be explained by the increased contact surface between the stirrer and the fluid and also by the greater interaction between the radial flow generated by the stirrer and the side wall of the tank, resulting in a higher power requirement. In addition, the presence of baffles improves mixing quality, but also results in an 87 % increase in power consumption compared to an unbaffled tank (Fig. 8). This

is because the baffles act as an obstacle to the flow and change its direction, which is mainly tangential in a tank without baffles.

TABLE III. Power number for Rushton turbine with and without baffles

Type	Present work	Exp.[24]	Num.[26]	Num.[27]	Exp.[28]
Baffle tank	6.72	6.07	5.40	–	6.0
Unbaffled tank	0.82	–	–	1.2	0.85
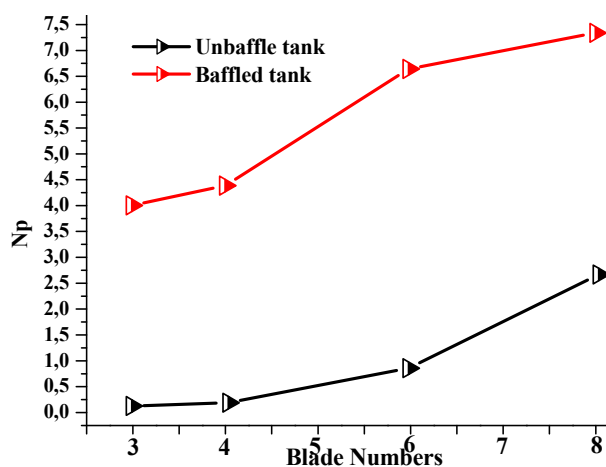
Fig. 8. Power number for different numbers of blades (Re = 40000).

Effect of the number of agitators on the flow rate

Figs. 9 and 10 illustrate the tangential and axial velocities of tanks with various stage numbers. As can be seen, the volume of fluid agitated is greater when there are three stages. Consequently, the intensity of the agitated fluid increases with the number of stirrers used. Figs. 9 and 10 illustrate the effect of the number of stirrers and Table IV provides the geometric dimensions used in the simulations. All configurations use the same type of stirrer, *i.e.*, a Rushton turbine with six blades mounted in a tank with vertical baffles. Table IV also indicates the distances between the stirrers for the multi-stage configurations. The standard geometry consists of a single Rushton turbine and was used in the validation phase. These results confirm that increasing the number of agitators enhances axial and tangential circulation, leading to better homogenization across the tank volume. Table IV.

Fig. 11 (a, b and c) shows the effect of the number of agitator stages on the induced flow in the tank. It can be seen that the tank equipped with three agitators has a larger volume of the agitated zone than the other configurations. However, this improvement is accompanied by an increase in energy consumption.
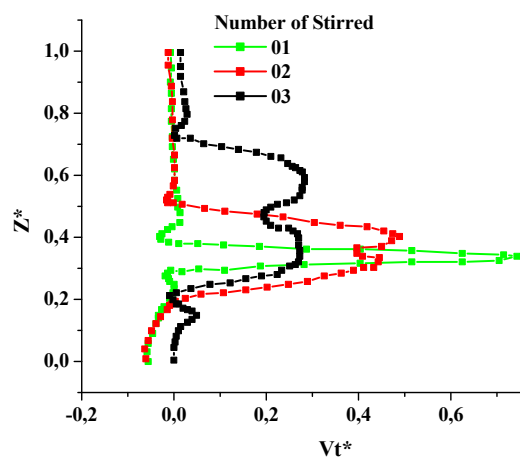
Fig. 9. Tangential velocity for different number of stirrers, Re = 40000.
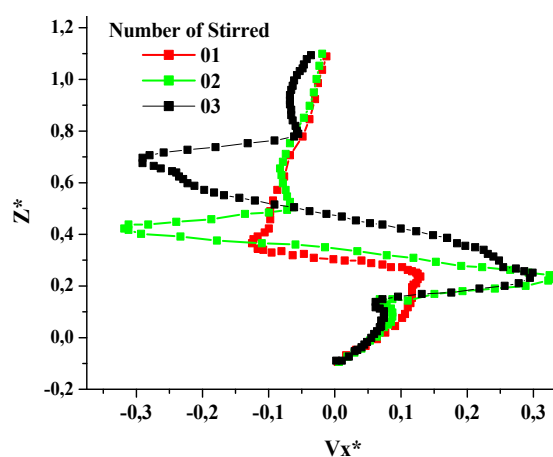
Fig. 10. Axial velocity for different number of stirrers, Re = 40000.

TABLE IV. Geometric parameters of multi-stage stirred tank configurations with Rushton turbines

Number of stirred	C1	C2	C3
2	0.80D	0.35D	0.35D
3	0.45D	0.35D	0.30D
Standard turbine	–	–	0.50D

a) standard turbine   b) two stirrers   c) three stirrers
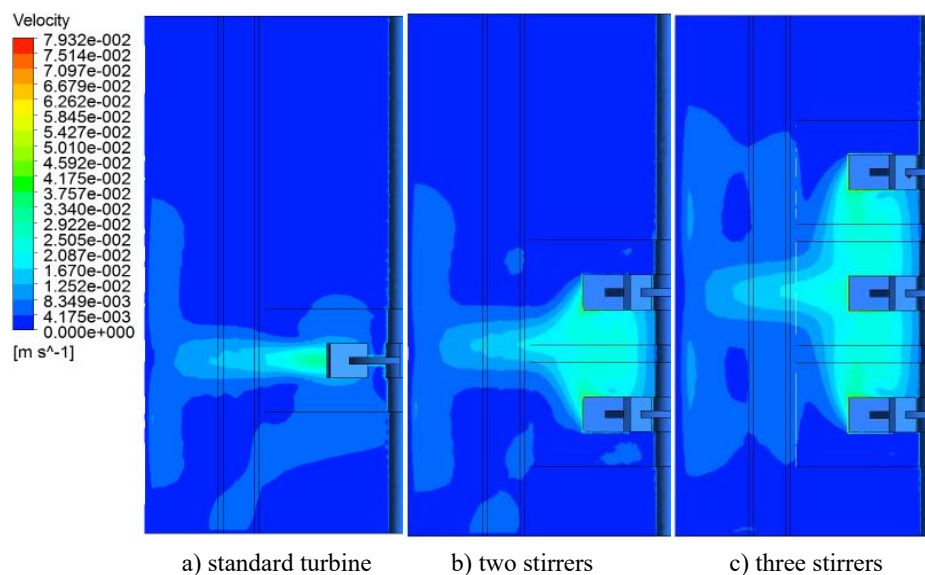
Fig. 11. Velocity champs for different numbers of agitators.

Effect of the space between agitators

Figs. 12 and 13 clearly show that the effect of the distance between the mixers on the formation of recirculation loops is significant. When the distance between the two stirrers is equal to $0.35D$, we observe that each stirrer develops only one recirculation loop (Case N°2 and Case N°3), suggesting that the two stirrers could be replaced by a single stirrer. On the other hand, when the difference exceeds $0.7D$, each stirrer generates two recirculation loops (Case N°1). In addition, when
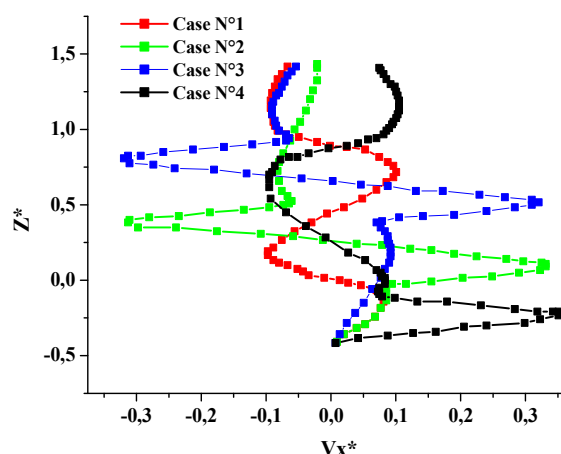
Fig. 12. Axial velocity for different positions of agitator ($X^* = 0.185$, Re = 40000).

the distance between the two stirrers increases further, as in Case N°4, three recirculation loops can be observed, as shown in Fig. 13. The flow intensity is higher in the lower part of the vessel compared to the upper part, which is caused by the large spacing between the two stirrers. This phenomenon is explained by the independent operation of each agitator, which has a positive effect on the efficacy of fluid mixing.
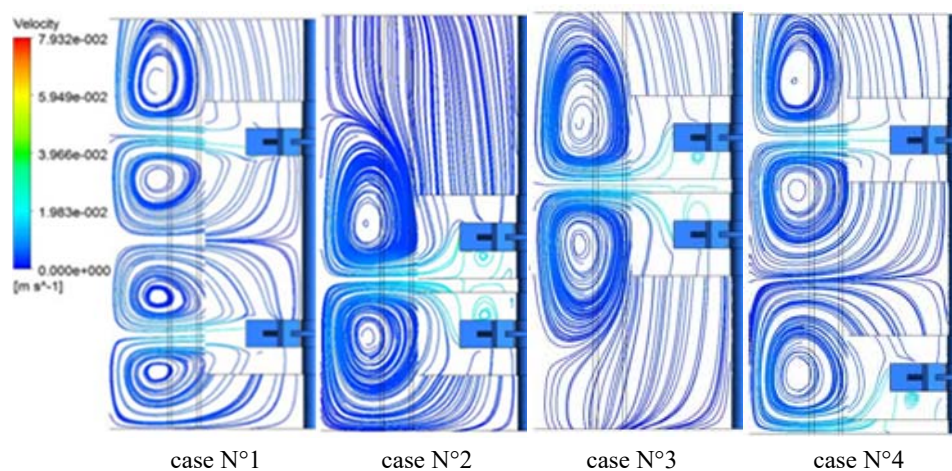
case N°1   case N°2   case N°3   case N°4
Fig. 13. Stream lines for different cases (Re = 40000).

CONCLUSION

The aim of this work is to study the influence of geometric parameters on the flow generated by a Rushton turbine, with and without baffles. The effect of the number of blades on energy consumption and mixing quality was clearly shown.

This study highlights the effect of the number of blades on the structure of the flow generated by the stirrer. The results show that increasing the number of blades has a significant effect on the volume of fluid swept, with a higher number of blades improving this coverage. In particular, an 8-blade Rushton turbine consumes 12 % more power than the standard 6-blade geometry.

The number of agitators in the tank also has a positive effect on flow intensity. In addition, the distance between the impellers plays a key role in the formation of recirculation zones. When the spacing is equal to 0.7D, recirculation loops are formed, which can disrupt the free surface of the fluid.

These findings provide useful insights for the practical design and optimization of stirred tanks, particularly in terms of improving mixing efficiency while managing power consumption. Parameters such as the number of blades and the presence of baffles significantly influence energy demand. The results also emphasize the importance of impeller spacing in controlling flow structures and surface stability.

For future work, optimizing the geometry and shape of baffles is identified as a promising direction. Since baffles play an important role in enhancing mixing but also increase power consumption, modifying their design may lead to better mixing performance with reduced energy costs. Moreover, the current numerical model does not account for multiphase flow or non-Newtonian behavior, which could be explored in future studies to enhance the model's applicability to real industrial processes.

ИЗВОД

CFD СИМУЛАЦИЈА ПЕРФОРМАНСИ РЕЗЕРВОАРА СА МЕШАЊЕМ

KAMLA YOUCEF[1], ZIED DRISS[2], MOHAMMED FOUKRACH[1], SERGIO ROSA[3] и TOUHAMI BAKI[4]

[1]Laboratory of Mechanics and Energy, Faculty of Technology, University Hassiba Ben Bouali of Chlef (UHBC), Algeria, [2]Laboratory of Electro-Mechanic Systems (LASEM), National School of Engineers of Sfax (ENIS), University of Sfax (US), Tunisia, [3]Polytechnic Institute of Bragança (IPB), Santa Apolonia Campus, Portugal u [4]Mechanical Faculty, Gaseous Fuels and Environment Laboratory, University of Sciences and Technology of Oran Mohamed Boudiaf (USTO-MB), BP 1505, El-M'Naouer, Oran 31000, Algeria

У овом раду извршена је нумеричка анализа тока флуида који генерише Раштонова турбина приликом свог рада. Топологија резултујућег тока флуида у великој мери зависи од неколико параметара, који укључују геометријску конфигурацију система и својства флуида који струји. У оквиру овог рада, једначине које описују систем засноване на k–ε моделу су решаване коришћењем методе коначних запремина. За неколико геометрија турбина, уз варирање броја лопатица од 6 до 12, анализирани су профили брзина, струјнице и димензије вртлога. Моделовање је укључило системе са једностепеним, двостепеним и тростепеним мешалицама, уз испитивање утицаја растојања између појединих мешалица на слику струјања. Коначно, нумеричке симулације извршене у оквиру овог рада валидиране су поређењем добијених резултата са експерименталним резултатима доступним у литератури, уз добро слагање експерименталних вредности са резултатима симулација.

(Примљено 15. априла, ревидирано 2. јуна, прихваћено 12. августа 2025)

REFERENCES

1. Z. Driss, in *Procedings of the International Conference on Advances in Mechanical Engineering and Mechanics, Hammamet, Tunisia*, 2006, pp. 1–6 (https://dx.doi.org/10.15866/irease.v7i3.3729)
2. L. Li, B. Xu, *Chem. Papers* **71** (2017) 1863 (https://dx.doi.org/10.1007/s11696-017-0180-1)
3. Y. Cui, H. Zhang, X. Li, M. Yang, Z. Guan, *Int. J. Agric. Biol. Eng.* **11** (2018) 111 (https://dx.doi.org/10.25165/j.ijabe.20181104.2729)
4. M. Jaszczur, A. Młynarczykowska, L. Demurtas *Energies* **13**(3) (2020) 640 (https://dx.doi.org/10.3390/en13030640)
5. F. L. Yang, S. J. Zhou, C. X. Zhang, *Korean J. Chem. Eng.* **32** (2015) 816 (https://doi.org/10.1007/s11814-014-0255-4)
6. L. Liangchao, C. Ning, X. Kefeng, X. Beiping, *Int. J. Chem. React. Eng.* **17** (2019) 20180215 (https://doi.org/10.1515/ijcre-2018-0215)
7. M. Kordas, G. Story, M. Konopacki, R. Rakoczy, *Ind. Eng. Chem. Res.* **52** (2013) 13818 (https://doi.org/10.1021/ie303086r)

8. H. Ameur, Y. Kamla, *Instal* **6** (2020) 42 (https://doi.org/10.36119/15.2020.6.5)
9. Y. Kamla, H. Ameur, M. I. Arab, B. Azeddine, *Data Brief* **39** (2021) 107669 (https://doi.org/10.1016/j.dib.2021.107669)
10. X. Dang, J. Guo, L.Yang, S. Xue, B. Ai, X. Li, L. Chen, W. Li, H. Qin, J. Zhang, *J. Taiwan Inst. Chem. Eng.* **131** (2022) 104 (https://doi.org/10.1016/j.jtice.2021.11.016)
11. S. Youcefi, A. Mokhefi, M. Bouzit, A. Youcefi, *Int. J. Heat Tech.* **41** (2023) 1489 (https://doi.org/10.18280/ijht.410611)
12. S. Bonnot, F. Cabaret, L. Fradette, P. A. Tanguy, *Chem. Eng. Res. Des.* **85** (2007) 1129 (https://doi.org/10.1205/cherd06215)
13. N. Hashemi, F. Ein-Mozaffari, S. R. Upreti, D. K. Hwang, *Chem. Eng. Sci.* **151** (2016) 25 (https://doi.org/10.1016/j.ces.2016.05.003)
14. C. Yang, J. Yao, X. Chen, M. Xie, G. Zhou, Z. Xu, B. Liu, *Chem. Eng. Res. Des.* **202** (2024) 377 (https://doi.org/10.1016/j.cherd.2023.12.040
15. H. H. Mortensen, F. Innings, A. Håkansson, *Chem. Eng. Res. Des.* **121** (2017) 245 (https://doi.org/10.1016/j.cherd.2017.03.016)
16. S. M. Mahmoudi, M. Yianneskis, in *Fluid Mechanics of Mixing. Modelling, Operations and Experimental Techniques*, R. King, Ed., Springer, Dordrecht, 1992, pp. 11–18 (https://doi.org/10.1007/978-94-015-7973-5_2)
17. K. Rutherford, K. C. Lee, S. M. M. Mahmoudi, M. Yianneskis, *AIChE* **42** (1996) 332 (https://doi.org/10.1002/aic.690420204)
18. A. W. Nienow, *Chem. Eng. Sci.* **52** (1997) 2557 (https://doi.org/10.1016/S0009-2509(97)00072-9)
19. P. M. Armenante, Y. T. Huang, T. Li, *Chem. Eng. Sci.* **47** (1992) 2865 (https://doi.org/10.1016/0009-2509(92)87143-E)
20. G. Montante, A. Brucato, K. C. Lee, M. Yianneskis, *Canadian J. Chem. Eng.* **77** (2009) 649 (https://doi.org/10.1002/cjce.5450770405)
21. A. Hadjeb, M. Bouzit, Y. Kamla, H. Ameur, *Green Sci.* **19** (2017) 83 (https://doi.org/10.1515/pjct-2017-0053)
22. S. Dabiri, A. Noorpoor, M. Arfaee, P. Kumar, W. Rauch, *Water (Switzerland)* **14** (2021) 105 (https://doi.org/10.3390/w13121629)
23. A. Reid, R. Rossi, C. Cottini, A. Benassi, *Meccanica* **15** (2024) 1 (https://doi.org/10.1007/s11012-024-01824-z)
24. H. Wu, G. K. Patterson, *Chem. Eng. Sci.* **44** (1989) 2207 (https://doi.org/10.1016/0009-2509(89)85155-3)
25. Z. Driss, A. Kaffel, B. B. Amira, G. Bouzgarrou, M. S. Abid, *Am. J. Energy Res.* **2** (2014) 67 (https://doi.org/10.12691/ajer-2-3-4)
26. D. A. Deglon, C. J. Meyer, *Minerals Eng.* **19** (2006) 1059 (https://doi.org/10.1016/j.mineng.2006.04.001)
27. C. D. Tacă, M. Păunescu, *Chem. Eng. Sci.* **56** (2001) 4445 (https://doi.org/10.1016/S0009-2509(01)00096-3)
28. J. Karcz, M. Major, *Chem. Eng. Process. Proc. Intens.* **37** (1998) 249 (https://doi.org/10.1016/S0255-2701(98)00033-6).

Investigation of corrosion causes and failures in the interior metal components of an automobile

JOVANKA N. PEJIĆ[1], BORE V. JEGDIĆ[1], BOJANA M. RADOJKOVIĆ[1]*, ANDJELA R. SIMOVIĆ[1], DUNJA D. MARUNKIĆ[1], BRANIMIR Z. JUGOVIĆ[2] and ALEKSANDRA S. POPOVIĆ[3]

[1]University of Belgrade, Institute for Chemistry, Technology and Metallurgy, Njegoševa 12, Belgrade, [2]Institute of Technical Sciences SASA, Knez Mihailova 35, Belgrade and [3]University of Belgrade, Faculty for Technology and Metallurgy, Karnegieva 4, Belgrade, Serbia

Abstract: The extent of corrosion and the underlying causes of damage to the interior metal components of a one-year-old automobile from a known brand, owned by a rental car company in Serbia, were investigated. The vehicle's interior, including upholstery and carpeting, showed no chemical spills or other damage. The solution obtained after rinsing a carpet sample from the car floor exhibited neutral pH. The corrosion behavior of the analyzed samples was determined using electrochemical impedance spectroscopy (EIS), linear polarization resistance (*LPR*) and linear sweep voltammetry (LSV, Tafel method). X-ray diffraction (XRD) and Fourier-transform infrared spectroscopy (FTIR) analyses showed that corrosion products taken from corroded steel parts contain akaganeite β-FeO(OH) and iron (II) chloride. FTIR analysis of the organic coating revealed that the applied epoxy layer was insufficiently crosslinked, making it permeable to moisture and chloride ions. Electrochemical corrosion measurements on steel with a similar chemical composition demonstrated an increased corrosion rate in a solution containing dissolved corrosion products compared to a reference solution. This accelerated corrosion was attributed to the acidity of akaganeite and iron (II) chloride, formed due to the vehicle's exposure to a humid and chloride-rich environment.

Keywords: car; corrosion; akaganeite; electrochemical methods; epoxy coatings.

INTRODUCTION

Corrosion poses a significant threat to the longevity and reliability of automobiles, impacting both their structural integrity and aesthetic appeal. From environmental factors like road salts and pollutants to inherent material vulnerabilities,

---

1383

vehicles are susceptible to various forms of corrosion that can compromise their performance.[1,2] Understanding the mechanisms and factors that contribute to automotive corrosion is crucial for developing effective prevention and mitigation strategies.[3–5] Numerous studies have examined corrosion failures in specific automotive components, providing valuable insights into real-world scenarios.[6–16]

Electrochemical corrosion, a primary cause of metal degradation, arises from chemical reactions between the metal surface and its environment.[17] This process involves anodic and cathodic reactions, leading to the dissolution of the metal in the presence of water or humidity. In the case of steel, a common material in automobiles, electrochemical corrosion results in the formation of iron oxy-hydroxides ($FeO(OH)$) on the surface.[18–20] These corrosion products, such as goethite (α-$FeO(OH)$) and lepidocrocite (γ-$FeO(OH)$), can sometimes form a protective layer, slowing down further corrosion. However, localized corrosion can still occur depending on the specific type of corrosion products present.

Akaganeite (β-$FeO(OH)$), another crystalline form of corrosion product, forms in humid environments with high chloride ion concentrations.[21–23] The incorporation of chloride ions into its crystal lattice makes akaganeite stable but also compromises its protective capabilities. The formation of akaganeite is facilitated at room or lower temperatures, under slightly acidic to neutral conditions (pH values from 4 to 7). If chloride ions are present to a lesser extent, then (instead of akaganeite) goethite, lepidocrocite and sometimes misawite (δ-$FeO(OH)$)[18–20] are formed. Unlike goethite and lepidocrocite, akaganeite offers minimal protection against further corrosion. It is considered that the presence of akaganeite in steel corrosion products is a sign of its active corrosion.

This study investigates an instance of significant corrosion observed in the interior metal components of a relatively new automobile from a known brand, used by a rental car company in Serbia. Despite no visible signs of chemical spills or damage inside the vehicle, substantial corrosion was evident. The research aims to identify potential chemical residues on the carpet and upholstery and analyze the corrosion products on the steel surfaces. By employing instrumental methods such as Fourier-transform infrared spectroscopy (FTIR) and X-ray diffraction (XRD), the composition of the organic coating and corrosion products were determined.

Furthermore, the corrosion resistance of steel (AISI 4130), which is similar in composition to the steel used in the analyzed automobile, was directly compared in a solution containing dissolved corrosion products versus a standard solution. Electrochemical methods, including electrochemical impedance spectroscopy (EIS), linear polarization resistance (*LPR*), and the linear sweep voltammetry (LSV, Tafel method) were applied to study the corrosion properties of investigated specimens.

The investigation revealed that the corrosion of the automobile's interior steel components is likely the result of exposure to a humid environment rich in chlorides rather than improper use during its short operational period. The inadequately crosslinked epoxy coating was found to be permeable to moisture and chlorides, contributing to the corrosion process. Additionally, the presence of akaganeite and iron (II) chloride in the corrosion products, along with the moderately acidic nature of the solution, indicates ongoing corrosion activity that necessitates further attention to protective measures in automotive design.

EXPERIMENTAL

Materials

The AISI 4130 steel (25CrMo4 according to the EN standard) used in this study belongs to the category of low-alloy Cr-Mo steels. The purity and source of all employed materials were verified before experimentation. Table I lists the chemical composition of the tested steel AISI 4130, according to the standard,[24] and the actual chemical composition determined by the XRF method (Olympus Vanta C Series Handheld XRF Analyzer).

TABLE I. Chemical composition of tested steel, wt. %

Composition	C	Mn	P	S	Si	Cr	Mo
Standard	0.28–0.33	0.40–0.60	0.035	0.040	0.15–0.35	0.80–1.1	0.15–0.25
Measured	–	0.49	0.023	0.038	0.43	0.88	0.21

Corrosion product analysis

The composition of the corrosion products extracted from corroded steel parts within the automobile was analyzed using a Nicolet iS10 (Thermo Scientific) Fourier transform infrared (FTIR) spectrometer. FTIR spectra were recorded over a range of 4000-400 cm^{-1} with a resolution of 4 cm^{-1} at room temperature. Additionally, a Philips PW 1710 powder diffractometer (XRD) was employed to analyze the steel corrosion products under the following conditions: an operating voltage of 40 kV, a current strength of 30 mA, with copper (Cu) as the anticathode (wavelength CuKα, 1.54178 Å). The test range was set from 2θ 4 to 65°, with a step size of 2θ 0.01° and a recording rate of 5 ° min^{-1}.

Electrochemical measurements

A standard condensate solution served as the comparison solution for the electrochemical corrosion measurements. Corrosion products from the steel parts were added to this standard solution until saturation was achieved, followed by thorough mixing and three-stage squeezing to extract dissolved substances.

Corrosion measurements were conducted in both the standard solution prior to adding corrosion products and in the saturated solution containing dissolved corrosion products. The pH values of both solutions were determined using a pH meter (HI 2210 Hanna Instruments), with a precision of 0.01 pH unit.

The linear polarization resistance (*LPR*) method was utilized to determine the corrosion current density and the corrosion rate. The polarization resistance (R_p) is defined as the slope of the potential–current density curve ($\Delta E/\Delta j$) at the corrosion potential (E_{corr}). The relationship between R_p and the corrosion current density (j_{corr}) is given by:[25]

$$R_p = B/j_{corr} \tag{1}$$

where B is a constant that depends on the anodic (b_a) and the cathodic (b_c) Tafel slopes, calculated as:

$$B = b_a b_c / 2.3(b_a + b_c) \tag{2}$$

For low-alloy steels in neutral solutions containing chloride ions, B is typically set at 25 mV.[26] The conversion of j_{corr} into the corrosion rate (v_{corr} in mm year^{-1}) was performed using Faraday's law:

$$v_{corr}(\text{mm year}^{-1}) = 0.01166 j_{corr}(\mu\text{A cm}^{-2}) \tag{3}$$

while the values for the constant were obtained from ASTM G1 and ASTM G102.[27,28]

Electrochemical impedance spectroscopy (EIS) measurements involved applying a sinusoidal voltage of ±10 mV amplitude across a frequency range from 100000 to 0.001 Hz, with the system responses recorded as real and imaginary impedance components. The values of j_{corr} and v_{corr} were also obtained by Linear sweep voltammetry (LSV, Tafel method). After establishing a stable corrosion potential (E_{corr}), the working electrode was polarized from –0.25 to 0.25 V relative to E_{corr} at a sweep rate of 0.5 mV s^{-1}. In all electrochemical measurements, a saturated calomel electrode (SCE) served as the reference electrode, while a Pt-grid acted as the auxiliary electrode. All electrochemical methods were conducted using a Gamry 620 potentiostat/galvanostat device.

RESULTS AND DISCUSSION

Corrosion damage: visual evidence from the automobile interior

A detailed visual inspection of the automobile interior was carried out, and appropriate photographs were taken. The automobile interior looked new and preserved without any visible mechanical or other failure. Fig. 1a shows the exterior view of the automobile's back seat. There is no noticeable damage on the upholstered parts of the rear bench and the upholstery looks brand new. The carpet on the automobile floor also seems to be preserved, without damage. The carpet in the trunk was clean completely and undamaged as well (Fig. 1b). There are no traces of liquid spillage (water stains, aggressive liquids, etc.), nor visible external damage to the carpet in the trunk.

Fig. 1. Exterior view of: a) the back seat of the car and b) the carpet in the automobile trunk.

However, corrosion was observed on various metal components located in the double bottom of the automobile trunk. Specifically, the metal parts around the spare wheel exhibited corrosion, and the towing hook was completely corroded.

Significant corrosion was also evident on the automobile jack (Fig. 2a), with the surfaces of these components entirely coated in characteristic yellow––brown to brown corrosion products. Upon removing the seat upholstery, corrosion was found on the seat frame and axle, similarly covering their entire surfaces (Fig. 2b). Notably, the sponge and seat material showed no signs of water stains, chemical residue, or other liquids that might have contributed to the corrosion of these metal parts; they appeared undamaged and well-preserved.

Fig. 2. Corrosion of: a) the automobile jack components and b) the frame and shaft inside.

Beneath the dashboard, behind the control pedals, extensive corrosion of several metal components was evident (Fig. 3a). These parts were entirely covered with the characteristic yellow–brown to brown corrosion products. Lifting the protective cover on the rear seat revealed similarly complete corrosion on some metal components (Fig. 3b). Galvanized screws were used to fasten the protective covers. Zinc is expected to corrode preferentially, thereby protecting the steel from corrosion. However, the steel components exhibited extensive corrosion while the zinc coating on the screws remained intact.

Fig. 3. Corrosion of: a) the steel components under the control panel and b) the steel parts under the protective mask on the rear seat.

When steel objects lack adequate corrosion protection, they corrode much faster than galvanized screws. Thus, under the prevailing corrosive conditions, the

zinc coating effectively protected the screws, but it was insufficient to prevent corrosion of the surrounding steel parts.

Building upon the previously observed corrosion patterns, Fig. 4 further illustrates instances of corrosion failure on steel parts within the automobile's interior. The surfaces of these components are entirely covered in characteristic yellow-brown to brown steel corrosion products, consistent with previous findings. Notably, Fig. 4d reveals significant corrosion along the edges of a corroded steel part, along with layers of powdery steel corrosion products, suggesting that the corrosion process occurred over an extended period.

Fig. 4. Corrosion of steel parts.

To further investigate the nature of the corrosive environment, pH measurements were taken. The solution derived from a sample of corrosion products obtained from the corroded steel parts exhibited a pH of 3.45, indicating moderate acidity. In contrast, the standard solution used for comparison registered a pH of 5.70, confirming its near-neutral character. Furthermore, the solution resulting from washing a carpet sample taken from the automobile floor showed a neutral pH of 6.92. These pH values support the conclusion that the corrosion products themselves created a moderately acidic environment, while the carpet remained neutral. This neutrality suggests that the corrosion was unlikely caused by an acid

spillage onto the carpet, nor did any acid appear to have permeated through the carpet to induce steel corrosion.

Characterization of corrosion products and organic coatings via *FTIR spectroscopy*

FTIR analysis of the corrosion products (Fig. 5) revealed characteristic peaks at 3348 and 1614 cm^{-1}, corresponding to asymmetric and symmetric O–H stretching vibrations, respectively. Additionally, bands observed at 844 and 639 cm^{-1} can be attributed to –OH bending modes, indicative of the presence of β-FeOOH.[29–32] The presence of chloride ions in the corrosion products can be observed based on the base peak at the 420 cm^{-1} wavelength, which originates from an acid chlorides in-plane deformation.[33]
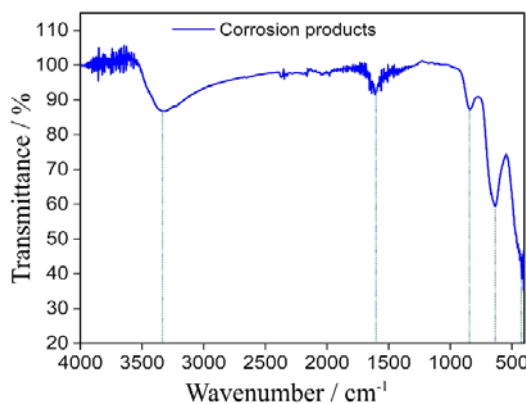
Fig. 5. FTIR diagram of steel corrosion products.

Given the extensive corrosion observed on the steel components, assessing the thickness and adhesion of the original organic coating proved challenging. On many components, the coating was absent, while on others, it was peeling away from the metal surface (Fig. 6). As a result, our analysis focused on determining the composition of the remaining coating fragments using FTIR spectroscopy.

Fig. 6. Appearance of the applied organic coating (paint) on the surface of the towing hook.

Fig. 7 shows the characteristic peaks obtained during the examination of the organic coating by the FTIR method. The organic coating contains a series of peaks corresponding to aromatic and aliphatic organic compounds, as well as an epoxy group, which is present in epoxy coatings.[34]
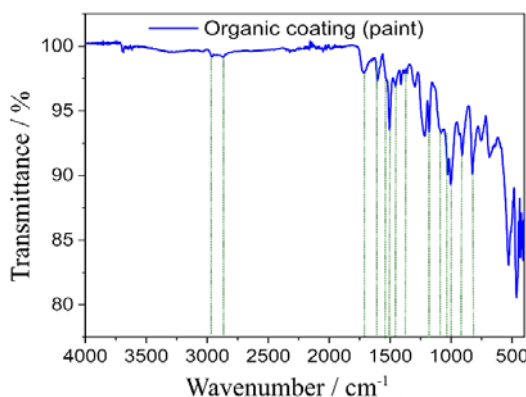
Fig. 7. Characteristic peaks obtained during the examination of the organic coating by the FTIR method.

The non-crosslinked epoxy coating (paint) has two characteristic peaks, which indicate the presence of the epoxy group: the first peak is located in the range of wavelengths from 3060 to 3000 cm^{-1}, while the second peak is located in the range of wavelengths from 960 to 810 cm^{-1} and it refers to the C–O deformation of the epoxy group.[35–39] The presence of peaks at 910 and 826 cm^{-1} wavelengths on the FTIR diagram (Fig. 7) indicates that the epoxy coating was not properly crosslinked. However, the absence of peaks in the range of wavelengths from 3060 to 3000 cm^{-1} is a sign that the epoxy coating is still partially crosslinked.[35–39]

In addition to the identification of peaks that are particularly characteristic of the epoxy group, other peaks that are also characteristic of the epoxy coating were identified. The peaks at 2965, 2863, 1456 and 1383 cm^{-1} wavelengths correspond to asymmetric and symmetric CH stretching of aromatic and aliphatic organic compounds.[37–40] The peak at wavelength 1602 cm^{-1} indicates the presence of the C=C group, and the peaks at the wavelengths 1531 and 1505 cm^{-1} indicate the presence of C–C stretching. The peak at 1180 cm^{-1} wavelengths corresponds to C–O stretching.[36] Also, the presence of the esters group (C=O) can be seen based on the peak at 1713 cm^{-1}, and the presence of the ethers group (C–O–C) is confirmed by peaks in the range of wavelengths from 1100 to 1000 cm^{-1}.[37]

The scheme structure of an epoxy resin before crosslinking is present in Fig. 8. It can be seen that the epoxy polymer on the ends of the molecule contains a characteristic epoxy group in the form of a three-angle. During curing, the characteristic epoxy group is opened, enabling proper epoxy coating cross-linking.
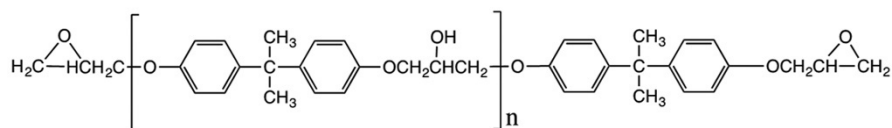
Fig. 8. Scheme structure of the epoxy polymer before crosslinking.

The inadequate cross-linking of the epoxy coating can be attributed to an improper curing process, such as curing at insufficiently high temperatures and/or for an inadequate duration. This incomplete crosslinking results in a porous coating, allowing chloride ions and moisture to penetrate through the pores, thereby creating favorable conditions for corrosion to occur. Additionally, the poorly crosslinked epoxy coating is brittle, making it prone to peeling from the steel surface. The weak adhesion of the coating may also stem from inadequate surface preparation or cleaning of the steel components before the application of the coating. These factors collectively explain the observed condition of the organic coating in the automobile and its inability to provide effective corrosion protection.

XRD characterization of corrosion products

The XRD analysis of the corrosion products collected from the automobile (Fig. 9) identified two crystalline phases: β-FeO(OH) (ferric oxy-hydroxide) and $FeCl_2 \cdot 4H_2O$. Semi-quantitative analysis showed that β-FeO(OH) accounted for approximately 88 wt. % of the corrosion products, while $FeCl_2 \cdot 4H_2O$ made up about 12 wt. %. The β-FeO(OH), also known as akaganeite, crystallizes in a monoclinic structure within space group I2/m (No. 12). Literature indicates that akaganeite requires chloride ions to stabilize its structure, with its formula more accurately represented as $FeO_{0.833}(OH)_{1.167}Cl_{0.167}$.[41] In its structure, octahedral chains form tunnels that are partially filled with chloride ions, occupying approximately two-thirds of the available sites. Hydrogen bonds between chlorides and surrounding hydrogen further stabilize the structure. At temperatures above 200 °C, akaganeite releases chloride ions and transforms into hematite Fe_2O_3, a more stable phase. The crystal structure and microstructure of akaganeite have been extensively documented in the literature.[21,22,42]

The identified phases are characteristic of steel corrosion under humid conditions with significant chloride ion presence. Akaganeite is commonly associated with active corrosion processes, while iron (II) chloride hydrate plays a role in sustaining these processes. In environments with lower chloride concentrations, alternative corrosion products such as goethite, lepidocrocite or misawite are typically formed, which tend to slow down steel corrosion compared to akaganeite. Thus, the presence of akaganeite in the analyzed sample indicates ongoing active

corrosion and suggests that the corrosive processes have persisted for a considerable period.
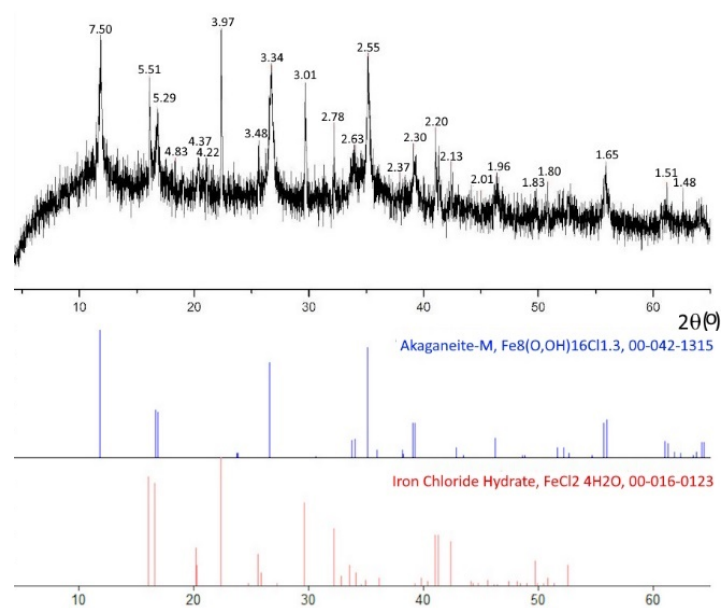
Fig 9. Diffractogram of the examined sample of corrosion products.

Iron (II) chloride present in the corrosion products undergoes hydrolysis in the presence of oxygen and moisture from the air, forming akaganeite, hydrogen ions, and additional chloride ions according to:[42]

$$2Fe^{2+} + 4Cl^- + 3H_2O + 1/2O_2 \rightarrow 2FeO(OH) + 4H^+ + 4Cl^- \qquad (4)$$
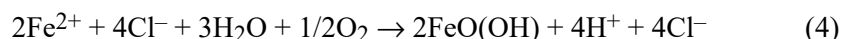
The generated hydrogen and chloride ions further accelerate steel corrosion through the reaction described as:

$$2Fe + 4H^+ + 4Cl^- + O_2 \rightarrow 2Fe^{2+} + 4Cl^- + 2H_2O \qquad (5)$$
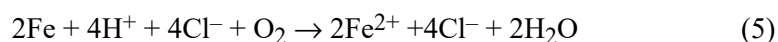
The resulting Fe^{2+} and Cl^- re-enter the hydrolysis cycle described in Eq. (4), perpetuating a self-sustaining process known as the Askey cycle.[43] This cycle produces an acidic environment due to H^+ generation and continuously forms akaganeite (β-FeO(OH)). The presence of akaganeite is thus a clear indicator of active steel corrosion.

As previously noted, no evidence of an acidic liquid spillage was observed on the carpet covering the corroded steel parts. The solution obtained by washing carpet particles exhibited a neutral pH while the solution containing dissolved corrosion products was acidic. This confirms that the corrosion was not caused by

external acidic substances penetrating through the carpet but rather by environmental factors such as moisture, oxygen, and chloride ions.

The non-properly crosslinked epoxy coating on the steel surface further facilitated corrosion. Its porous and brittle nature allowed moisture and chloride ions to diffuse through to the steel surface, initiating and sustaining the Askey cycle.[43] This continuous regeneration of hydrogen and chloride ions promotes an acidic environment conducive to active corrosion. Only complete drying of the corrosion products, including akaganeite and iron (II) chloride hydrate, can disrupt this cycle and stop further degradation.

Electrochemical measurements

Linear polarization resistance (*LPR*) measurements were conducted to assess the corrosion resistance of steel in different solutions, and the results are presented in Fig. 10. As can be seen from Fig. 10, the polarization resistance (R_p) for steel in the solution containing corrosion products was 2.38 kΩ cm^2, while the R_p for steel in the standard solution was 3.28 kΩ cm^2.
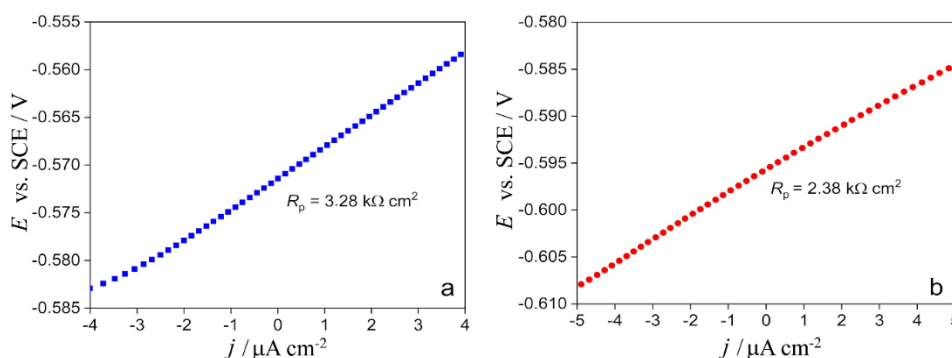
Fig. 10. Results of the *LPR* testing in: a) standard solution and b) solution obtained by dissolving corrosion products in the standard solution.

Therefore, *LPR* measurements indicated that the standard solution exhibited a higher R_p than the solution with dissolved steel corrosion products. This suggests that the corrosion products, which contain akaganeite (*β*-FeO(OH)) and iron (II) chloride, release hydrogen ions according to Reaction (4), creating a moderately acidic environment. It is well-established that the corrosion rate of steel is higher in acidic environments compared to neutral ones, which explains the lower R_p value observed in the solution containing corrosion products.

The main corrosion parameters obtained by the *LPR* method are presented in Table II.

The results of the electrochemical impedance spectroscopy (EIS) testing of steel are presented in Fig. 11. The equivalent electrical circuit (EEC) used to fit the

EIS data is shown in Fig. 11d. In this circuit, R_e represents the electrolyte resistance, R_p denotes the polarization resistance and CPE is the constant phase element that accounts for surface inhomogeneities of the tested steel.

TABLE II. Test results using the *LPR* method

Solution	R_p / kΩ cm²	j_{corr} / µA cm⁻²	v_{corr} / mm year⁻¹
Standard	3.28	7.62	0.089
Standard + corrosion product	2.38	10.5	1.22

The polarization resistance values obtained from the EIS measurements, based on both the Nyquist and Bode modulus diagrams (Fig. 11), revealed that the R_p value for steel in the solution containing dissolved corrosion products was 1.67 kΩ cm², while in the standard solution it was higher, at 2.64 kΩ cm².
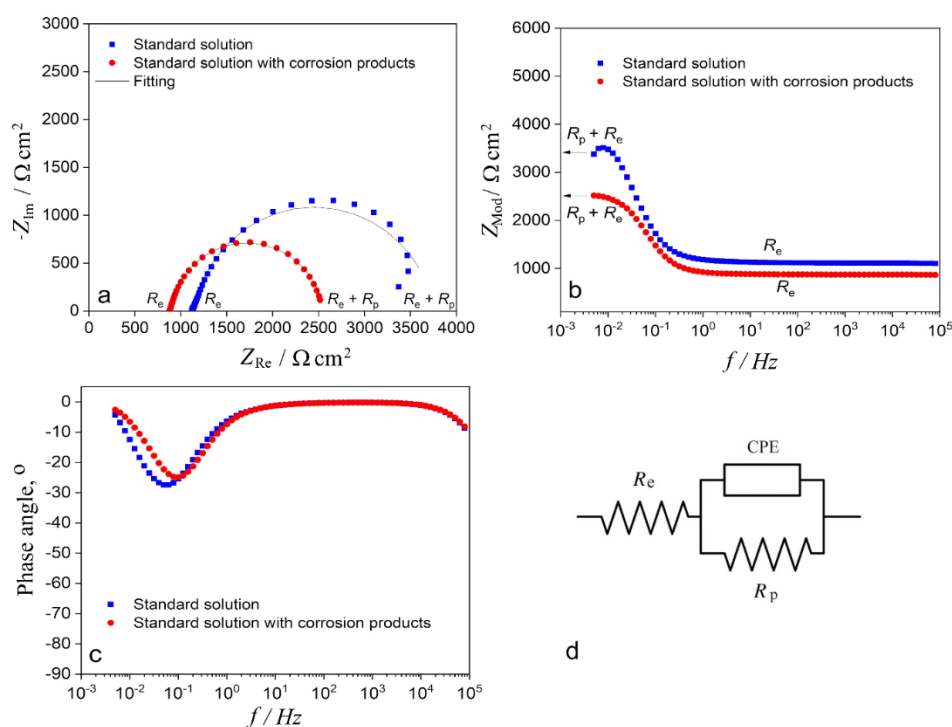
Fig 11. Results of the EIS test in the standard solution and in the standard solution in which corrosion products are dissolved; a) Nyquist diagrams, c) Bode modulus diagrams, c) Bode phase diagrams and d) equivalent electric circuit (EEC).

The polarization resistance (R_p) values obtained by the EIS method are consistent with the results obtained from the *LPR* method. Specifically, a lower R_p value was recorded for the solution containing dissolved corrosion products com-

pared to the pure standard solution, which is also reflected in Tables II and III. This reduction in polarization resistance is attributed to the moderate acidity present in the solution with dissolved corrosion products.

TABLE III. The results of the EIS method

Solution	R_e kΩ cm²	R_p kΩ cm²	CPE Q / mΩ⁻¹ sⁿ cm⁻²	n	C_{eff} mF cm²	j_{corr} µA cm⁻²	v_{corr} mm year⁻¹
Standard	1.13	2.64	1.545	0.875	1.889	9.47	0.110
Standard + corrosion product	0.88	1.67	1.578	0.899	1.759	15.0	0.175

Additionally, Table III presents the effective capacitance (C_{eff}), calculated using the Brug Equation,[44] which incorporates values for R_p, Q and n from the same table:

$$C_{eff} = R_p^{(1-n)/n} Q^{1/n} \qquad (6)$$

The C_{eff} value for specimens tested in the standard solution is somewhat higher than that for specimens exposed to the solution containing corrosion products.

Furthermore, Fig. 11 indicates a relatively high electrolyte resistance (R_e), attributed to the low concentration of ions in the tested solutions. In contrast, the electrolyte resistance is lower in the solution with dissolved steel corrosion products due to the presence of hydrogen ions.

The Bode phase diagram further supports these observations, revealing that steel exhibits reduced corrosion resistance in the standard solution containing corrosion products (Fig. 11 c and Table III) compared to the pure standard solution. The narrowing of the peak at low frequencies reinforces this conclusion, along with a shift of the peak towards higher frequencies, consistent with the literature findings.[45]

Linear sweep voltammetry (LSV) testing of steel (Fig. 12) revealed a higher corrosion current density (j_{corr}) in the solution containing dissolved corrosion products compared to the standard solution. Specifically, the j_{corr} value for steel in the solution with corrosion products was 11 µA cm⁻², while in the standard solution, it was 5 µA cm⁻². The corrosion rate values (v_{corr}) were then calculated using Faraday's law based on the measured j_{corr} values (Table IV).

These results demonstrate that the presence of corrosion products increases the corrosion rate, which is consistent with the findings from the *LPR* and EIS measurements. This increased corrosion rate is attributed to the acidic environment generated by akaganeite (β-FeO(OH)) and iron (II) chloride present in the corrosion products, according to Reaction (4).

While the absolute corrosion rate values vary somewhat depending on the method used (*LPR*, EIS or LSV), all methods consistently indicated a higher steel

corrosion rate in the solution containing dissolved corrosion products compared to the standard solution.
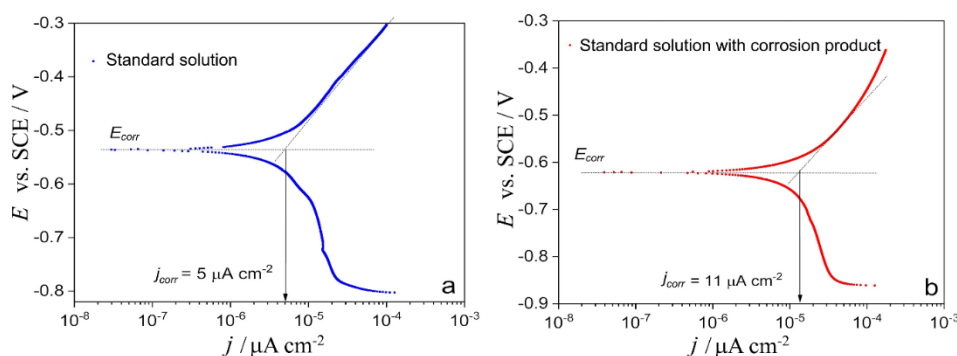
Fig. 12. Results of testing steel by the Tafel method in: a) the standard solution and b) the solution obtained by dissolving corrosion products in the standard solution.

TABLE IV. The results of the LSV test

Solution	j_{corr} / μA cm^{-2}	v_{corr} / mm year^{-1}
Standard	5	0.058
Standard + corrosion products	11	0.128

CONCLUSION

In conclusion, the evidence suggests that the observed corrosion within the automobile was likely initiated before its short-term use. Visual inspection ruled out a spillage as a cause, while XRD and FTIR analyses identified akageneite (β-FeO(OH)) and iron (II) chloride within the corrosion products, indicating a chloride-rich environment. The presence of akaganeite, a known indicator of active corrosion, suggests that the steel components were exposed to humidity and chlorides, possibly during storage. Furthermore, the epoxy coating's improper crosslinking, as revealed by FTIR, would have compromised its protective capabilities, allowing corrosive agents to reach the metal surface. Electrochemical measurements confirmed these findings, demonstrating a higher corrosion rate in solutions containing the identified corrosion products. This study highlights the importance of proper material selection, storage conditions, and coating application techniques in preventing premature corrosion in automotive components, ultimately extending the lifespan and reliability of vehicles.

И З В О Д

ИСПИТИВАЊЕ УЗРОКА КОРОЗИЈЕ И ОШТЕЋЕЊА УНУТРАШЊИХ МЕТАЛНИХ КОМПОНЕНАТА АУТОМОБИЛА

ЈОВАНКА Н. ПЕЈИЋ[1], БОРЕ В: ЈЕГДИЋ[1], БОЈАНА М. РАДОЈКОВИЋ[1], АНЂЕЛА Р. СИМОВИЋ[1], ДУЊА Д. МАРУНКИЋ[1], БРАНИМИР З. ЈУГОВИЋ[2] и АЛЕКСАНДРА С. ПОПОВИЋ[3]

[1]*Универзитет у Београду, Институт за хемију, технологију и металургију, Његошева 12, Београд,* [2]*Институт техничких наука Српске академије наука и уметности, Кнез Михаилова 35, Београд* и [3]*Универзитет у Београду, Технолошко–металуршки факултет, Карнегијева 4, Београд*

У раду су испитане размере корозије и основни узроци оштећења унутрашњих металних компоненти аутомобила познате марке, који је у власништву компаније за изнајмљивање аутомобила у Србији и који је био у употреби годину дана. Унутрашњост аутомобила, тапациринзи и тепих на поду аутомобила, су очувани, без трагова оштећења, а такође није утврђено присуство неке корозивне хемикалије. Раствор настао после испирања делова тепиха узетог са пода аутомобила се понашао неутрално. Корозивно понашање анализираних узорака одређено је коришћењем спектроскопије електро-хемијске импеданције, линеарне поларизационе отпорности и линеарне волтаметрије. Резултати анализе методама рендгенске дифракције (XRD) и инфрацрвене спектро-скопије са Фуријеовом трансформацијом (FTIR) показали су да производи корозије узети са кородираних челичних делова садрже акаганеит (β-FeO(OH)) и гвожђе(II)-хлорид. FTIR анализа органске превлаке открила је да је примењена епоксидна превлака недовољно умрежена, што је чини пропусном за влагу и хлоридне јоне. Електрохемијска мерења корозије на челику сличног хемијског састава са челиком коришћеним за израду аутомобила су показала повећану брзину корозије у раствору који садржи растворене производе корозије у поређењу са референтним раствором. Ова убрзана корозија при-писује се киселости акаганеита и гвожђе(II)-хлорида, који су настали услед изложености делова возила влажном и хлоридима богатом окружењу.

(Примљено 27. марта, ревидирано 17. априла, прихваћено 10. јула 2025)

REFERENCES

1. L. J. Korb, D. L. Olson, in *ASM Handbook, Volume 13: Corrosion*, ASM International, Materials Park, OH, 1987
2. A. Kumar, J. Singh, *Proc. Eng. Sci.* **4** (2022) 13 (https://doi.org/10.24874/PES04.01.003)
3. D. Mizuno, S. Suzuki, S. Fujita, N. Hara, *Corros. Sci.* **83** (2014) 217 (http://dx.doi.org/10.1016/j.corsci.2014.02.020)
4. K. Dhonde, M. Mirhassani, E. Tam, S.Sawyer-Beaulieu, *Materials* **15** (2022) 3211 (https://doi.org/10.3390/ma15093211)
5. S. Sawyer-Beaulieu, E. Tam, A. Hussein, *Materials* **15** (2022) 3053 (https://doi.org/10.3390/ma15093053)
6. E. Díaza, L. Soria, J. M. Gallardo, *Eng. Fail. Anal.* **105** (2019) 828 (https://doi.org/10.1016/j.engfailanal.2019.07.022)
7. F. Bergh, G.C. Silva, C. Silva, P. Paiva, *Eng. Fail. Anal.* **129** (2021) 105679 (https://doi.org/10.1016/j.engfailanal.2021.105679)
8. J. Gweon, J. Park, W.K. Lee, D.Y. Kim, H. Jang, *Eng. Fail. Anal.* **128** (2021) 105583 (https://doi.org/10.1016/j.engfailanal.2021.105583)
9. C. Langer, W. Wendland, K. Honold, L. Schmidt, J.S. Gutmann, M. Dornbusch, *Eng. Fail. Anal.* **91** (2018) 255 (https://doi.org/10.1016/j.engfailanal.2018.04.031)

10. D. H. Sohn, Y. Lee, H. J. Jang, S. Y. Cho, *Corros. Sci. Technol.* **21** (2022) 1 (https://doi.org/10.14773/cst.2022.21.1.1)

11. L. Kosec, A. Nagode, G. Kosec, D. Kovacevic, B. Karpe, B. Zorc, B. Kosec, *Case Stud. Eng. Fail. Anal.* **4** (2015) 100 (http://dx.doi.org/10.1016/j.csefa.2013.12.004)

12. N. Solomon, I. Solomon, *Eng. Fail. Anal.* **92** (2018) 44 (https://doi.org/10.1016/j.engfailanal.2018.04.049)

13. M. Torkar, M. Godec, *Eng. Fail. Anal.* **10** (2003) 325 (https://doi.org/10.1016/S1350-6307(02)00069-9)

14. M. Godec, Dj. Mandrino, M. Jenko, *Eng. Fail. Anal.* **16** (2009) 1252 (https://doi.org/10.1016/j.engfailanal.2008.08.022)

15. M. I. Khana, M. A. Khan, A. Shakoor, *Eng. Fail. Anal.* **85** (2018) 77 (https://doi.org/10.1016/j.engfailanal.2017.12.001)

16. E. Arslan, K. Genel, *Eng. Fail. Anal.* **153** (2023) 107569 (https://doi.org/10.1016/j.engfailanal.2023.107569)

17. R. W. Revie, H. H. Uhlig, *Corrosion and Corrosion Control: An Introduction to Corrosion Science and Engineering*, John Wiley and Sons, Hoboken, NJ, 2008 (https://doi.org/10.1002/9780470277270)

18. J. Labbe, J. Ledion, F. Hui, *Corros. Sci.* **50** (2008) 1228 (https://doi.org/10.1016/j.corsci.2007.08.023)

19. T. Misawa, T. Kyuno, W. Suetaka, S. Shimodaira, *Corros. Sci.* **11** (1971) 35 (https://doi.org/10.1016/S0010-938X(71)80072-0)

20. T. Misawa, T. Kyuno, W. Suetaka, S. Shimodaira, *Corros. Sci.* **14** (1974) 279 (https://doi.org/10.1016/S0010-938X(74)80037-5)

21. S. Reguer, F. Mirambet, E. Dooryhee, J. Hodeau, P. Dillmann, P. Lagarde, *Corros. Sci.* **51** (2009) 2795 (https://doi.org/10.1016/j.corsci.2009.07.012)

22. K. Stahl, K. Nielsen, J. Jiang, B. Lebech, J. Hanson, P. Norby, J. Lanschot, *Corros. Sci.* **45** (2003) 2563 (https://doi.org/10.1016/S0010-938X(03)00078-7)

23. M. Gilberg, N. Seeley, *Stud. Conserv.* **26** (1981) 50 (https://doi.org/10.1179/sic.1981.26.2.50)

24. *ASTM A29: Standard Specification for General Requirements for Steel Bars, Carbon and Alloy, Hot-Wrought*, ASTM International, West Conshohocken, PA, 2023

25. *ASTM-G59: Standard Test Method for Conducting Potentiodynamic Polarization Resistance Measurements*, ASTM International, West Conshohocken, PA, 2023

26. S. Papavinasamt, in *Techniques for corrosion monitoring*, L. Yang, Ed., Woodhead Publishing, Cambridge, 2008, p. 49 (https://doi.org/10.1016/B978-0-08-103003-5.00003-5)

27. *ASTM G1: Standard Practice for Preparing, Cleaning, and Evaluating Corrosion Test Specimens*, ASTM International, West Conshohocken, PA, 2023

28. *ASTM G102: Calculation of Corrosion Rates and Related Information from Electrochemical Measurements*, ASTM International, West Conshohocken, PA, 2023

29. G. Nauer, P. Strecha, N. Brinda-Konopik, G. Liptay, *J. Therm. Anal.* **30** (1985) 813 (https://doi.org/10.1007/bf01913309)

30. S. Bashir, R. W. McCabe, C. Boxall, M. S. Leaver, D. Mobbs, *J. Nanopart. Res.* **11** (2008) 701 (https://doi.org/10.1007/s11051-008-9467-z)

31. L. Mei, L. Liao, Z. Wang, C. Xu, *Adv. Mater. Sci. Eng.* **2015** (2015) 250836 (https://doi.org/10.1155/2015/250836)

32. M. Amini, Y. Mousazade, Z. Zand, M. Bagherzadeh, M. M. Najafpour, *Sci. Rep.* **11** (2021) 6642 (https://doi.org/10.1038/s41598-021-85672-x)
33. J. B. Lambert, H. F. Shurvell, R. G. Cooks, *Introduction to Organic Spectroscopy*, 1st ed., Macmillan, New York, 1987
34. P. Maity, S. V. Kasisomayajula, V. Parameswaran1, S. Basu, N. Gupta, *IEEE T. Dielect. El. In.* **15** (2008) 63 (https://doi.org/10.1109/T-DEI.2008.4446737)
35. S. Zlatković, G. S. Nikolić, J. V. Stamenković, *Chem. Ind.* **57** (2003) 563 (https://doi.org/10.2298/HEMIND0311563Z)
36. G. Nikolic, S. Zlatkovic, M. Cakic, S. Cakic, C. Lacnjevac, Z. Rajic, *Sensors* **10** (2010) 684 (https://doi.org/10.3390/s100100684)
37. M. G. González, J. C. Cabanelas, J. Baselga, in *Infrared Spectroscopy – Materials Science, Engineering and Technology*, T. Theophanides Ed., InTech, London, 2012 (https://doi.org/10.5772/36323)
38. L.A. Teixeira, V.D.L. Junior, S.M. da Luz, in *Proceedings of 16th Brazilian Polymer Conference (16 CBPOL)*, Ouro Preto-MG, Brazil, October 24–28, 2021, p. 1338 (http://e-democracia.com.br/cbpol/anais/2021/pdfs/plenary/4DPJ.pdf)
39. D. S. Achilias, M. M. Karabela, E. A. Varkopoulou, I. D. Sideridou*, J. Macromol. Sci., A* **49** (2012) 630 (https://doi.org/10.1080/10601325.2012.696995)
40. N. Rajagopalan, A. S. Khanna, *J. Coat.* **2014** (2014) 515470 (https://doi.org/10.1155/2014/515470)
41. C. Rémazeilles, Ph. Refait, *Corros. Sci.* **49** (2007) 844 (https://doi.org/10.1016/j.corsci.2006.06.003)
42. L. S. Selwyn, in *ASM Handbook, Volume 13C: Corrosion: Environments and Industries*, S. D. Cramer, B. S. Covino, Jr., Eds., ASM International, Materials Park, OH, 2006, p. 306 (ISBN**:** 978-0-87170-709-3)
43. A. Askey, S. B. Lyon, G. E. Thompson, J. B. Johnson, G. C. Wood, M. Cooke, P. Sage, *Corros. Sci.* **34** (1993) 233 (https://doi.org/10.1016/0010-938X(93)90004-Z)
44. B. Hirschorn, M. E. Orazem, B. Tribollet, V. Vivier, I. Frateur, M. Musiani, *J. Electrochem. Soc.* **157** (2010) C458 (https://doi.org/10.1149/1.3499565)
45. L. G. Ecco, S. Rossi, F. Deflorian, M. Fedel, *J. Electrochem. Soc.* **165** (2018) C933 (https://doi.org/10.1149/2.0371814jes).

Effect of pyrolysis temperature and time of Robusta coffee husk on yield and product characteristics

THI THU HUONG NGUYEN*, NGOC TOAN VU, HONG MINH LE
and HONG SON NGUYEN

*Department of Chemical and Radiological Toxicology Technology Research,
Institute of New Technology, Hanoi, Vietnam*

Abstract: The utilization and recycling of biochar from coffee husks is a global issue, as 1.8 Mt of coffee husks were produced in 2023. The mechanism of coffee husk pyrolysis and the factors influencing pyrolysis temperature and time on the properties of biochar were studied. Coffee husks were pyrolyzed at 350, 450 and 550 °C and held for 30, 45 and 60 min to form biochar, the physicochemical properties of biochar were characterized by thermogravimetric analysis, X-ray diffraction, surface morphology and Fourier-transform infrared spectroscopy. The pyrolysis of coffee husks occurs due to dehydration, decomposition and carbonization reactions. Pyrolysis temperature and time directly affect the yield of biochar, pH, fixed carbon, volatile matter, ash, nitrogen, phosphorus and potassium contents. Furthermore, pyrolysis temperature has a greater influence on the properties of biochar than pyrolysis time. The high potassium content of biochar can significantly replace conventional potash fertilizers. Therefore, biochar plays a dual role as a liming agent and can be used as a soil additive.

Keywords: pyrolysis mechanism; biochar properties; nitrogen content; phosphorus content; potassium content; soil additive.

INTRODUCTION

Over five billion tons of agricultural by-products are generated annually.[1] However, these agrarian by-product utilization options account for a small part because they are costly, laborious and time-consuming.[2,3] In the Central Highlands of Vietnam, agricultural by-products are often landfilled, stored on soil and direct combustion after the end of the harvest season.[4] These irreparable environmental effects, such as increased emissions of CH_4, N_2O, CO_2, loss of nutrients and soil fertility and soil and groundwater pollution, affect human health and cause global warming.[2,5] The conversion of agricultural by-products such as coffee husks into

---

1401

biochar as soil improvement additives provides nutrients to plants such as trace and macroelements, helps plants photosynthesize and increases the sugar content of fruits.[6–8] In addition, biochar is a carbon-rich material, which increases soil carbon storage, is biodegradable, some heavy metals convert to less toxic forms, eliminates pathogens, increases cation exchange capacity, increase pH, reduce compaction and increase soil water holding capacity.[2,9–12]

Biomass from agricultural, industrial, food and forestry waste produces biochar.[13] This biochar is produced by pyrolysis of biomass under temperature conditions from 350 to 600 °C and an oxygen-deficient environment.[14,15] The products of the biomass pyrolysis process, in addition to biochar, also include bio-oil and gas.[15] In 2023, Vietnamese coffee will be harvested at 29.2 million 60-kg bags, while world coffee will be 168.2 million 60-kg bags, meaning that Vietnamese coffee accounts for 17 % of global production, and is the second largest coffee producer in the world.[16] Since coffee husks account for about 18 % of the weight of fresh coffee cherries, more than 1.8 Mt of husks will be produced worldwide in 2023.[17,18]

This by-product is currently less reused as a raw material for the biochar production process. Biochar characteristics depend on factors that affect the quantity and quality of charcoal production, namely temperature and pyrolysis time.[19] Various studies have compared the efficiency of biochar generated at low and high temperatures for soil reclamation.[20,21] However, the effects of coffee husk pyrolysis on temperature and time are still unclear. Furthermore, the pyrolysis mechanism of coffee husks has been little studied in previous studies due to the complex reactions and mechanisms.[15,22] Determining the structure of biochar is also very important to clarify coal's physical and chemical properties.[14]

This research focuses on determining the biochar structure through TGA, XRD, FE-SEM and FTIR techniques and evaluating the physicochemical properties of biomass and biochar derived from coffee husks at different temperatures and pyrolysis times. Moreover, the mechanism of pyrolysis of coffee husks is also proposed.

EXPERIMENTAL

Reagents

o-Phenanthroline monohydrate ($C_{12}H_8N_2.H_2O$, ≥ 99.5 %, Merck, Germany). Sulfuric acid (H_2SO_4, ≥ 95 %) and ethanol (C_2H_5OH, ≥ 99.8 %) from Fisher, UK. Nessler reagent, 2,4--dinitrophenol ($C_6H_4N_2O_5$, ≥ 99 %) from Alpha Chemika, India. Hydrochloric acid (HCl, 37 %), potassium dichromate ($K_2Cr_2O_7$, ≥ 99.8 %), phosphoric acid (H_3PO_4, ≥ 85 %), nitric acid (HNO_3 concentrate, ≥ 65 %), iron (II) sulfate heptahydrate ($FeSO_4.7H_2O$, ≥ 99 %), ammonium iron (II) sulfate hexahydrate ($FeSO_4(NH_4)_2SO_4.6H_2O$, ≥ 99.5 %), sodium hydroxide (NaOH, ≥ 96 %), boric acid (H_3BO_3, ≥ 99.5 %), methyl blue ($C_{37}H_{27}N_3Na_2O_9S_3$, ≥ 98.5 %), methyl red ($C_{15}H_{15}N_3O_2$, ≥ 95 %), ammonia solution (NH_4OH, 27 %) from Xilong, China. 0.1 mol/L HCl standard tube (Cemaco, Vietnam) and ultrapure water (Milli-Q Reference, Millipore, France).

Equipment

Analytical weighing (Shimadzu Auw220d, Japan), drying cabinet (HN101, China), sift (hole size 0.22 mm), kiln (SX2-5-12, China), ball mill (Retsch PM100, USA), pH measuring equipment (Mettler Toledo S220K, China), distillation equipment UDK 139 (Velp, Italy), UV––Vis measuring equipment (Shimadzu 1900i, Japan), flame photometer (FP6400, China).

TGA analysis using the Netzsch TG 209F1 Libra thermal analyzer (Netzsch Instrument Corp., Germany) in a nitrogen medium with a heating rate of 10 °C/min from a temperature of 30 °C to a final temperature of 800 °C with samples weighing about 5 mg to determine the thermal decomposition properties of coffee husks. Then, the first-order derivative of the TG function, the DTG curve, is used to determine the mass loss in the temperature range.

X-ray diffraction analysis is performed to detect all mineral phases and chemical structures present in biochar. Powdered biochar samples were fed into glass dishes and analyzed on the D8-Advance instrument (Bruker, Germany) with CuKα radiation (wavelength about 1.5418 Å), measurement range 2θ from 10 to 70°, with a jump of 0.03°. Mineral phases are determined by comparing and contrasting distances d with the ICDD standard database system.

The surface morphology of biochar samples was measured using a FE-SEM scanning electron microscope device (JSM-IT800, Japan). Samples were dried at 70 °C in an oven before SEM measurements.

Coffee husks, crushed biochar with KBr, pellets, then FTIR measurement on the Tensor II instrument (Bruker, Germany), wavelength range 400 to 4000 cm^{-1}, with a resolution of 1.4263 cm^{-1} with 16 scans.

Raw material preparation and biochar production

Coffee husks of the Robusta variety (Fig. 1) are collected from households in Ea Tan commune, Krong Nang district, Dak Lak province. The sampling location is 13.10° N, 108.30° E, and transported to the experimental site, the Institute of New Technology. After being separated from the ripe coffee cherries, the coffee husks were dried on a tarpaulin for 5 days, avoiding direct sunlight. Then, the coffee husks were manually removed from impurities such as dry branches and filtered through a 3 mm sieve to remove soil. Oven-dried coffee husks were done at 70 °C for 8 h. The samples were stored in sealed plastic containers at room temperature.
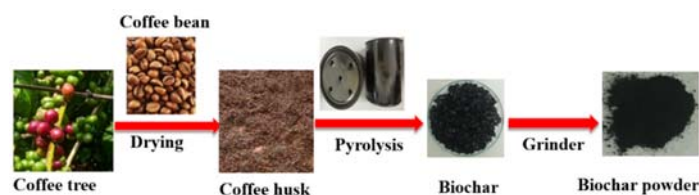
Fig. 1. The process of biochar formation.

Biochar from seed husks is said to work well with soil when pyrolysis is at temperatures not more than 550 °C, so this study selected temperatures of 350, 450 and 550 °C to conduct[23] Nine types of biochar are produced from coffee husks with three pyrolysis temperatures (350, 450 and 550 °C) and pyrolysis time (30, 45 and 60 min). Before pyrolysis, coffee husks are dried at a temperature of 70 °C. In each pyrolysis process under an anoxygenic atmosphere, approximately 160 g of biomass mass was used. The final pyrolysis temperatures reached 350, 450 or 550 °C with a constant heating rate of 10 °C/min. The biochar samples were held for 30, 45 or 60 min at a final temperature, and then allowed to cool to room temperature. After that,

the biochar samples are crushed by a ball mill for 1 h at 300 rpm. After grinding the marbles, the samples are sieved through a 0.22 mm grid and dried at 70 °C for low humidity before analysis. The particle size of coffee husks is essential in the resulting biochar properties and affects the concentration of volatiles during pyrolysis.[22,24] To address concerns related to particle size, the biochar in this study had a particle size no larger than 0.22 mm to increase uniformity in analysis.

Characteristic assessment of properties of biochar

Biochar from coffee husks is characterized by pH, moisture content, performance, volatile solids content, ash, fixed carbon, calcification value, organic carbon, total nitrogen, phosphorus and potassium.

The pH of biochar is determined according to ISO 10390:2021 by pH measuring equipment in water at 1:5 volume ratio immediately after shaking the sample for 1 h.

The moisture content of the biochar is obtained by drying about 5 g of the sample (recording the weighing mass before drying, m_0) in the drying cabinet at 70 °C to constant weight, and then weighing the mass after drying (m_s) to calculate the result according to:

$$\text{Humidity(\%)} = \frac{100(m_0 - m_s)}{m_0} \tag{1}$$

Volatile solids, ash, and fixed carbon are defined according to ASTM D1762-84 (2021). Biochar samples are placed in a covered crucible in a furnace at 950 °C for 6 min. Mass loss is associated with volatile material (DBH). That biochar is returned to the kiln at 750 °C for 6 h. The material remaining after burning is ash. The fixed carbon content is determined as:

$$\text{Fixed carbon(\%)} = 100 - DBH - Ash \tag{2}$$

The biochar calcification value is determined by acid–base titration using Eq. (3).[25] Weigh 0.5 g of biochar and 20 mL of shake for 2 h, then titrate with 0.1 mol/L HCl to the endpoint with pH 2.0. To ensure that the pH of biochar is stable at 2.0 after 12 h of equilibrium, the pH is measured again and adjusted with the above HCl solution if necessary. The volume of acid used and the pH value are recorded:

$$\text{Calcification value} = \text{Total volume of HCl reaches stable value / pH range} \tag{3}$$

The total nitrogen content is determined by the Kjeldahl decomposition and distillation method in 3 stages: conversion of nitrogen compounds in the sample into ammonium by H_2SO_4 and catalyst (K_2SO_4 and Se, stage 1), followed by distillation of ammonium by 40 % NaOH solution (stage 2), collect NH_3 (stage 3) with a solution of boric acid.[26] Stage 1: weigh about 2 g of sample, add 1 g of catalyst (ratio of K_2SO_4 and Se to mass is 100:1), gradually increase the temperature to 200 °C, keep 200 °C for 120 min, continue to increase the temperature to 350 °C for about 60 min (until the white smoke is gone, the sample solution is clear), cool, add 50 mL of water, boil 10 min, add water until the volume of solution is 200 mL (solution A). Stage 2: distillation of 30 mL of solution A using distillation equipment UDK 139 yields solution B. The installation mode of UDK 139 equipment is 50 mL H_2O, 50 mL NaOH 40 %, and 5 min. Solution B dissolves with 25 mL of 5 % boric acid. 25 mL of 5 % boric acid contains 0.5 mL of methyl blue–methyl-red color indicator. Ammonium was determined in the mixture using Nessler's reagent. The final stage: titrate solution B with HCl, 0.2 M. The nitrogen content is calculated by the Eq. (4). In particular, V_{test}, and V_0 are the volume of 0.2 M HCl used for titration of the test sample and the white sample (mL), and m is the mass of analyzed biochar (g):

$$N(\%) = \frac{0.2802(V_{\text{test}} - V_0)}{m} \tag{4}$$

The phosphorus content is determined by Eq. (5) according to the molybdenum blue method measured by UV–Vis.[27] About 200 mL of 2 % citric acid solution contains 2 g of sample, shake for 60 min, filter through green tape filter paper, and obtain solution A. Take 20 mL of solution A, 1 mL H_2SO_4, 1 mL H_2O, boil slightly for about 30 min, add 10 mL of thick HNO_3, boil slightly until almost empty, cool, add 10 mL of water, boil 5 min, add water so that the volume reaches 50 mL (solution B). Measure optical absorption at a wavelength of 720 nm on a UV–Vis measuring device by preparing a solution before measuring as follows: the mixture has 5 mL of solution B, 5 mL of water, 2 drops of indicator α-dinitrophenol, drip drops of 10 % NH_4OH until the solution turns yellow, then drip a few drops of 10 % HCl for all yellow, add 8 mL of molybdenum blue mixture, add water until the solution has a volume of 50 mL. Construct a calibration representing the correlation between photo-adsorption and standard phosphorus solution concentration, where *Abs* is the optical adsorption, *m* is the mass of analyzed biochar (g):

$$P(\%) = \frac{0.5(0.5114\,Abs - 0.0054)}{m} \tag{5}$$

The potassium content is determined by a flame photometer with an extraction solvent of 0.05 N HCl.[28] The potassium content is calculated by the Eq. (6). In particular, K_1 and K_0 are the potassium concentration in the sample and the white sample (mg/L), respectively, and *m* is the mass of biochar analyzed (g):

$$K(\%) = \frac{K_1 - K_0}{42.768m} \tag{6}$$

Statistical analysis

The data is analyzed for variance analysis (ANOVA) to find significant differences between factors such as pyrolysis temperature, pyrolysis time and their interaction. The test result reaches the *F* probability level of 0.05. All data is used using Origin (software Origin, version 9.85, OriginLab Corporation, Northampton, MA, USA) for data analysis and graphing. The acronym T350-30 means that coffee husks are pyrolysis at 350 °C, and when it reaches 350 °C, they calcine for 30 min.

RESULTS AND DISCUSSION

Influence of pyrolysis temperature and time on biochar performance

The resulting biochar yield is calculated as the ratio between the volume of biochar obtained and biomass. The biochar yield decreased with increasing pyrolysis temperature (Fig. 2a). This is explained by the fact that as the temperature increases, moisture loss occurs, and large amounts of volatile organic compounds are released, resulting in a decrease in the volume of biochar formed.[2,29] The 300––450 °C coal formation process produces an immense amount of coal biomass, consistent with the results of DTG spectroscopy and the other research.[30] The increase in pyrolysis time on the same low pyrolysis temperature (at 350 and 450 °C) also reduces the biochar yield (Fig. 2a) since the higher temperature leads to more

cracking reactions occurring that change the internal structure and surface of biochar, similar to Hu and Das's reports.[22,31]
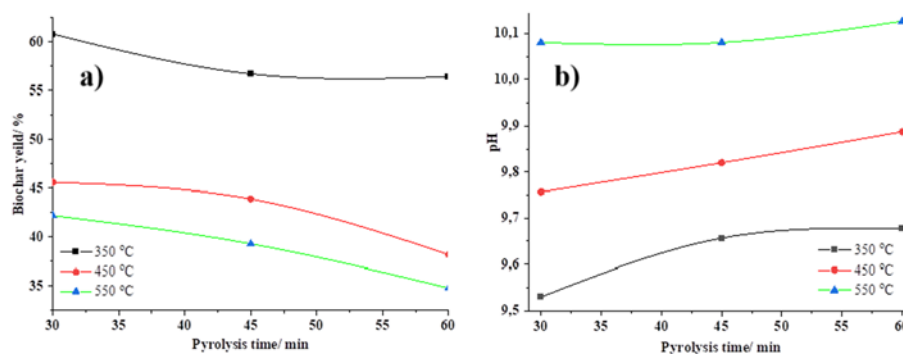

Fig. 2. a) Biochar performance obtained at different temperatures and pyrolysis times; b) pH of biochar at different temperatures and pyrolysis times.

Influence of pyrolysis temperature and time on the pH of biochar

The increased pyrolysis temperature and time cause the pH of biochar to increase. Overall, the pH value of biochar is higher than 9 (Fig. 2b). This is explained by the relative concentration of non-pyrolyzed inorganic elements already present in the original coffee husk, the cations in the ash are enriched, the loss of acid functional groups, and the formation of oxides, hydroxides, alkalis such as Ca–Mg-bearing K, Na, carbonate mineral phases and reduced concentration of functional groups on acidic surfaces.[8,31,32] Compared to the pH of coffee husks (pH 6.5), pyrolysis increases the pH in water, and the pH value increases to 3.5 units of biomass when pyrolysis is at 550 °C (Fig. 2b). The pH value of biochar increases with increasing pyrolysis temperature, which has been reported with biochar from rice straw and sawdust.[19,33] Among biochar, the highest pH value was recorded in pyrolysis coffee husks at 550 °C for 60 min, and pH was 10.1.

To produce biochar with pH 10, a 57 % increase in pyrolysis temperature (from 350 to 550 °C) is necessary. However, doubling the time (from 30 to 60 min) at the same pyrolysis temperature of 350 or 450 °C) still cannot produce biochar with a pH of around 10. This shows that the pyrolysis temperature has a more significant influence on the pH of biochar than the pyrolysis time.

Influence of pyrolysis temperature and time on the content of elements (N, P, K) of biochar

The pyrolysis temperature and time values of coffee husks are directly proportional to the content of phosphorus, and potassium and inversely proportional to the nitrogen content of biochar (Fig. S-1 of the Supplementary material to this paper). Sometimes, the temperature and duration of pyrolysis increases, and the

nitrogen content decreases. This result is consistent with the research of Das and Pariyar.[2,14] This is explained by the volatility of nitrogen during pyrolysis, which causes nitrogen loss.[14] When using biochar to fertilize crops, additional fertilizers, especially nitrogen, should be applied to avoid nitrogen fixation in the soil and maintain soil fertility. However, N fixation can be a beneficial mechanism to minimize N_2O emissions and reduce the amount of N leached from soil.[34] Notably, all types of biochar contain significant amounts of phosphorus (Fig. S-1). This may be due to the interaction process between organic compounds and PO_4^{3-}, producing a precipitate of phosphorus oxide.[2] The high potassium content in coffee husks (Fig. S-1) can significantly replace the conventional source K, which serves as a slow-release fertilizer K, indicating these biochars' high agronomic value.[12] The high K content in biochar (Fig. S-1) is mainly because carbonates and oxides of K are more soluble in water than carbonates and oxides of Mg and Ca.[2] Biochar pyrolysis occurs at low temperatures and acid dissolves faster, also nutrients such as K and P are less soluble in acid.[2] Nitrogen, phosphorus, and potassium help biochar play a role in adding minerals to soil and plants.

Influence of temperature and pyrolysis time on the physical properties of biochar

The higher the temperature and pyrolysis time of coffee husks, the higher the fixed carbon and ash content while reducing biochar's volatile content (Fig. S-2 of the Supplementary material). In addition, Fig. S-2 shows high fixed carbon content in biochar samples (85.67 %) and high volatile matter content in coffee husk samples (80.66 %). Coffee husks and biochar have different moisture contents.

Fig. S-2 shows apparent differences in ash content between biochar samples. The ash content in biochar ranges from 12.68 to 22.51 %. The high ash content in biochar from coffee husks can be attributed to the high content of K (4.29 %) in biomass (Fig. S-2) to protect the composition of organic substances and the structure of biochar during pyrolysis.[35] High ash content is associated with $KHCO_3$, verified by XRD analysis (Fig. S-2). The fixed carbon content is inversely proportional to the ash content (Fig. S-2). However, all are below 9 % (Fig. S-2), sufficient for determining the content of volatiles, ash, and fixed carbon.[36] The moisture content in the samples can be thought to be the free water content, the amount of desiccant water present in the cell wall, and linked to hydroxyl groups.[14] That characteristic makes biochar from coffee husks a potential material to increase the neutralization ability of the soil to overcome the acidity of the soil.

Coffee husks have a high volatile matter content (80.66 %), which makes pyrolysis occur faster (Fig. S-2), similar to Yousef's report when studying mangoes.[36] The volatile content of biochar decreases when the pyrolysis temperature increases from 450 to 550 °C (Fig. S-2). This is explained by the increase in aromatization, water evaporation, low molecular weight hydrocarbons and increased hydroxide and carbonate content, the presence of lignin that can resist thermal decomposition

at temperatures of 450 °C, but not at temperatures as high as 550 °C.[37] The magnitude of the volatile matter content in biochar is a vital attribute for evaluating the C and N-cycle bioavailability of biochar in the soil ecosystem.

The ability to neutralize acidity was assessed through the reduced calcification value of biochar with increasing temperature and pyrolysis time of coffee husks (Fig. 3c). That said, soil acidity is judged by calcification value and pH. In addition, at any temperature, the pyrolysis of coffee husks has a higher calcification value than other types of biochar, which is related to the high concentration of minerals present in biochar, especially $KHCO_3$ found in XRD spectroscopy (Fig. S-2).[38] Therefore, the calcification value of biochar is mainly adjusted by the ash content of coal, chemical composition (especially basic cations), and pH of biochar. This characteristic should be considered when applying biochar to the soil to adjust soil acidity.

Spectral characteristics

The TGA technique has been used to determine coffee husks' decomposition temperature and evaluate coffee husks' kinetics and other reactions over a wide temperature range of 0–800 °C (Fig. 3b). The TG curve clearly shows these phases (Fig. 3b, black). The DTG curve of coffee husks is used to determine the main composition of biomass during thermal decomposition (Fig. 3b, red).

The thermal decomposition process of coffee husks is divided into three main stages: dehydration, decomposition and coalization. The dehydration stage and low weight volatiles from room temperature to 190 °C. Water evaporation causes disruption of bonds and the formation of hydroperoxide groups, –COOH and –CO.[22] The initial 6.92 % weight loss was attributed to the moisture content of the coffee husk sample, as noted rice husk.[39] The stage of decomposition of hemicellulose, cellulose, and a small fraction of high lignin is from 190 to 450 °C, forming into biochar, bio-oil and gas. The most prominent degradation peak of coffee husks is 307.3 °C. Coffee husks cannot be used for synthetic applications as they are high thermal strength material, and they will decompose when the processing temperature is more significant than 190 °C. This situation is common in food waste such as mango peels, bagasse, bean husks and corn stalks.[15,36] Above 450 °C, thermal decomposition occurs more slowly due to the slow decomposition of lignin and carbon-containing solids. The heating rate increases, resulting in a shift of the TG curve to a temperature of 800 °C due to better heat transfer to the inside of the coffee husk. Fig. 3b shows that hemicellulose, cellulose and lignin have decomposition temperature ranges corresponding to 3 characteristic peaks at 204, 307 and 529 °C, consistent with the Chin-Pampillo report.[22] In summary, the thermal decomposition mechanism is necessary to determine the change in biochar's physicochemical properties and its application.
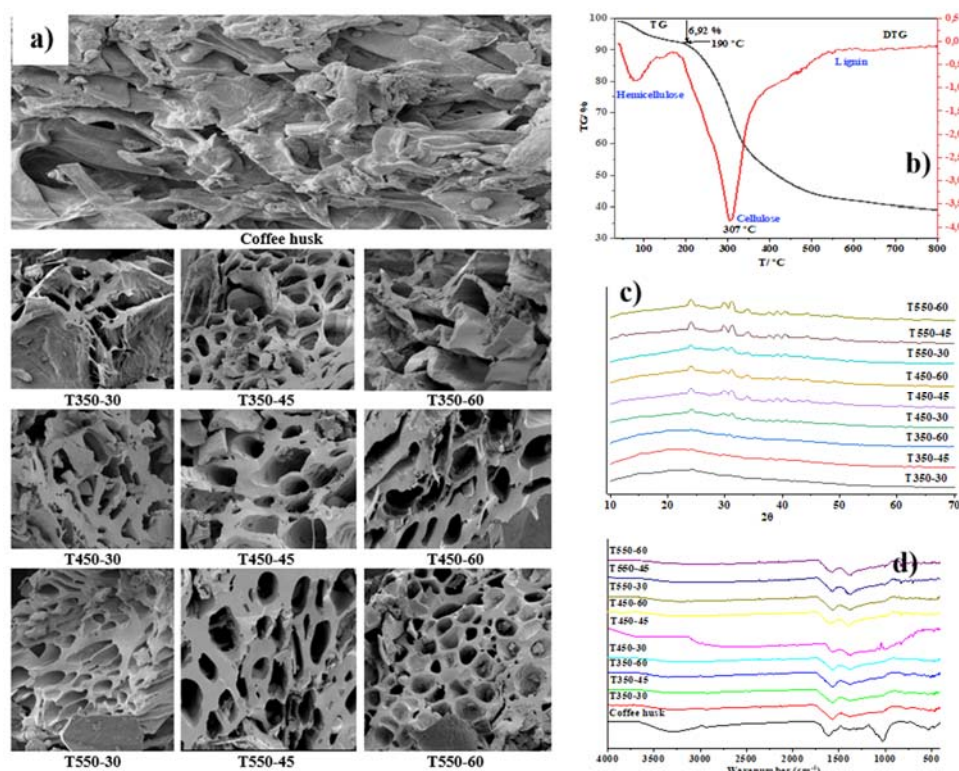
Fig. 3. a) FE-SEM of biochar samples (3000× magnification); b) TG and DTG analysis of coffee husks; c) XRD patterns of biochar; d) FTIR spectrum of coffee husks and biochar types from coffee husks at different temperatures and times.

XRD of biochar samples from coffee husks at different temperatures and pyrolysis times to determine the mineral composition in crystalline form in biochar (Fig. 3c). Peaks at 2θ 40.6445° are thought to be the presence of KCl. The presence of SiO_2 is also found from peaks at 2θ 49.2262 and 60.6585° in XRD spectrum. The peak of SiO_2 is more substantial at the pyrolysis husk at 450–550 °C and for 45–60 min (Fig. 3c). Biochar at three pyrolysis temperatures containing $KHCO_3$, SiO_2 and KCl was also observed: report on weeds and on rice straw.[2,3] The sharpness and peak intensity of the peaks increased slightly as the temperature and pyrolysis time increased, indicating that the crystalline mineral content evenly increased in biochar. At pyrolysis temperatures above 450 °C and pyrolysis times above 45 min stronger peaks appeared, indicating that part of the cellulose's crystal structure has been lost, similar to the different report.[40] Peak magnitude at 2θ 24.1345, 29.8655 and 31.1424° shows the relative accumulation of $KHCO_3$ in biochar from coffee husks (Fig. 3c). The formation of $KHCO_3$ is facilitated by the reaction of K and CO_2 released during the thermal decomposition of hemicellulose

and cellulose. The increased $KHCO_3$ content can also be explained by the high carbon content in coffee husks' biochar.

FE-SEM results show that coffee husks and biochar have rough surfaces and most of them have irregular shapes (Fig. 3a). The more you increase the pyrolysis temperature and the pyrolysis time, the biochar surface becomes smoother, the number of pores increases, the pore size increases and has a somewhat honeycomb--like structure, so the biochar has greater porosity (Fig. 3a). At a pyrolysis temperature of 450 °C and a pyrolysis time of 60 min, biochar has a more porous structure, rougher surface, and larger pore size. The pores on the biochar surface help microorganisms grow and the porosity of biochar helps increase water retention.[41] This is explained by the evaporation of water and volatile substances.[42]

FTIR spectroscopy of biomass and biochar obtained at different temperatures and pyrolysis times is shown in Fig. 3d. Table S-I of the Supplementary material presents the characteristics of the functional groups. Fig. 3d shows the peak characteristics of coffee husks' firm, medium and weak decomposition before and after pyrolysis at 350, 450 and 550 °C for 30, 45 and 60 min. With increasing temperature and pyrolysis time, the base content of the functional group in the aromatic ring increases, while the content of groups present in acids (–OH of phenol and C=O) decreases. Organic groups exist, even at high pyrolysis temperatures and long pyrolysis times, which may be associated with high ash content. Ash acts as a heat--resistant component, which can protect organic compounds against decomposition and hinder the formation of aromatic compounds as the temperature and pyrolysis time increase.[25]

CONCLUSION

Robusta coffee husks are the raw materials used to make 9 types of biochar, using temperature and pyrolysis time control processes. Increasing temperature and pyrolysis time reduce biochar generation performance, volatiles, surface functional groups, nitrogen content and increased pH, ash content, fixed carbon, organic carbon, phosphorus and potassium. Moreover, the pyrolysis temperature dramatically affects the pyrolysis time on the above characteristics of biochar. Biochars are characterized by high calcification value, which makes them a potential material for regulating soil acidity. This biochar serves as a source of P and K for plants. The more the temperature and pyrolysis time increase, the more stable and precise the phase structure of $KHCO_3$. With increasing temperature and pyrolysis time, the base content of the functional group in the aromatic ring increases, while the content of groups present in acids (–OH of phenol and C=O) decreases. Thus, biochar plays a dual role as a liming agent and a source of nutrients for the soil to grow crops. Biochar is made at 450 °C for 60 min for the best energy-saving and environmentally friendly nutritional content.

SUPPLEMENTARY MATERIAL

Additional data and information are available electronically at the pages of journal web-site: https://www.shd-pub.org.rs/index.php/JSCS/article/view/13070, or from the corresponding author on request.

ИЗВОД

УТИЦАЈ ТЕМПЕРАТУРЕ И ВРЕМЕНА ПИРОЛИЗЕ ЉУСКЕ КАФЕ РОБУСТА НА ПРИНОС И КАРАКТЕРИСТИКЕ ПРОИЗВОДА

THI THU HUONG NGUYEN, NGOC TOAN VU, HONG MINH LE и HONG SON NGUYEN

Department of Chemical and Radiological Toxicology Technology Research, Institute of New Technology, Hanoi, Vietnam

Коришћење и рециклажа биоугља из љуски кафе је глобално питање, с обзиром на то да је 2023. године произведено 1,8 милиона тона љуски кафе. Проучавани су механизам пиролизе љуске кафе и фактори као што су температура и време пиролизе који утичу на својства биоугља. Љуске од кафе су пиролизоване на 350, 450 и 550 °C и држане 30, 45 и 60 min на датој температури, да би се формирао биоугаљ, а физичко–хемијска својства биоугља су окарактерисана термогравиметријском анализом, рендгенском дифракцијом, испитивањем морфологије површине и инфрацрвеном спектроскопијом са Фуријеовом трансформацијом. Пиролиза љуски кафе настаје услед реакција дехидрације, разлагања и карбонизације. Температура и време пиролизе директно утичу на принос биоугља, pH, фиксни угљеник, испарљиве материје, пепео, азот, фосфор и садржај калијума. Осим тога, температура пиролизе има већи утицај на својства биоугља него време пиролизе. Висок садржај калијума у биоугљу може у великој мери да служи као замена за конвенционална калијумова ђубрива. Због тога, биоугаљ игра двоструку улогу као „*liming*" агенс, и може се користити као додатак земљишту.

(Примљено 2. октобра, ревидирано 10. октобра 2024, прихваћено 10. јануара 2025)

REFERENCES

1. R. Shinde, D. K. Shahi, P. Mahapatra, C. S. Singh, S. K. Naik, N. Thombare, A. K. Singh, *Ind. Crops Prod.* **181** (2022) 114772 (https://doi.org/10.1016/j.indcrop.2022.114772)
2. S. K. Das, G. K. Ghosh, R. Avasthe, K. Sinha, *J. Hazard. Mater.* **407** (2021) 124370 (https://doi.org/10.1016/j.jhazmat.2020.124370)
3. A. S. El-Hassanin, M. R. Samak, S. R. Radwan, G. A. El-Chaghaby, *Environ. Nat. Resour. J.* **18** (2020) 283 (https://doi.org/10.32526/ennrj.18.3.2020.27)
4. E. Cassou, S. M. Jaffee, J. Ru, *The challenge of agricultural pollution: evidence from China, Vietnam, and the Philippines*, World Bank Publications, Washington, DC, 2018
5. N. Kumar, A. Chaudhary, O. Ahlawat, A. Naorem, G. Upadhyay, R. Chhokar, S. Gill, A. Khippal, S. Tripathi, G. Singh, *Soil Till. Res.* **228** (2023) 105641 (https://doi.org/10.1016/j.still.2023.105641)
6. C. Doulgeris, Z. Kypritidou, V. Kinigopoulou, E. Hatzigiannakis, *J. Agron.* **13** (2023) 784 (https://doi.org/10.3390/agronomy13030784)
7. G. Enaime, M. Lübken, *Appl. Sci.* **11** (2021) 8914 (https://doi.org/10.3390/app11198914)

8. Z. Elkhlifi, J. Iftikhar, M. Sarraf, B. Ali, M. H. Saleem, I. Ibranshahib, M. D. Bispo, L. Meili, S. Ercisli, E. Torun Kayabasi, *Sustainability* **15** (2023) 2527 (https://doi.org/10.3390/su15032527)

9. M. Irfan, M. Mudassir, M. J. Khan, K. M. Dawar, D. Muhammad, I. A. Mian, W. Ali, S. Fahad, S. Saud, Z. Hayat, *Sci. Rep.* **11** (2021) 18416 (https://doi.org/10.1038/s41598-021-97525-8)

10. Z. Liu, Z. Xu, L. Xu, F. Buyong, T. C. Chay, Z. Li, Y. Cai, B. Hu, Y. Zhu, X. Wang, *Carbon Res.* **1** (2022) 8 (https://doi.org/10.1007/s44246-022-00007-3)

11. J. Poveda, Á. Martínez-Gómez, C. Fenoll, C. Escobar, *Phytopathology* **111** (2021) 1490 (https://doi.org/10.1094/PHYTO-06-20-0248-RVW)

12. M. Z. Hossain, M. M. Bahar, B. Sarkar, S. W. Donne, Y. S. Ok, K. N. Palansooriya, M. B. Kirkham, S. Chowdhury, N. Bolan, *Biochar* **2** (2020) 379 (https://doi.org/10.1007/s42773-020-00065-z)

13. M. Antar, D. Lyu, M. Nazari, A. Shah, X. Zhou, D. L. Smith, *Renew. Sustain. Energy Rev.* **139** (2021) 110691 (https://doi.org/10.1016/j.rser.2020.110691)

14. P. Pariyar, K. Kumari, M. K. Jain, P. S. Jadhao, *Sci. Total Environ.* **713** (2020) 136433 (https://doi.org/10.1016/j.scitotenv.2019.136433)

15. J. E. Silva, G. Q. Calixto, C. C. de Almeida, D. M. Melo, M. A. Melo, J. C. Freitas, R. M. Braga, *J. Therm. Anal. Calorim.* **137** (2019) 1635 (https://doi.org/10.1007/s10973-019-08048-4)

16. G. M. Ngure, K. N. Watanabe, *Front. Sustain. Food Syst.* **8** (2024) (https://doi.org/10.3389/fsufs.2024.1431849)

17. R. Manrique, D. Vásquez, C. Ceballos, F. Chejne, A. s. Amell, *ACS Omega* **4** (2019) 2957 (https://doi.org/10.1021/acsomega.8b02591)

18. N. T. H. Thăng, *Eur. J. Bus. Res.* **7** (2022) (https://doi.org/10.24018/ejbmr.2022.7.3.1356)

19. S. Chandra, J. Bhattacharya, *J. Clean. Prod.* **215** (2019) 1123 (https://doi.org/10.1016/j.jclepro.2019.01.079)

20. C. Setter, F. Silva, M. Assis, C. Ataíde, P. Trugilho, T. Oliveira, *Fuel* **261** (2020) 116420 (https://doi.org/10.1016/j.fuel.2019.116420)

21. J. S. Chin-Pampillo, A. Alfaro-Vargas, R. Rojas, C. E. Giacomelli, M. Perez-Villanueva, C. Chinchilla-Soto, J. M. Alcañiz, X. Domene, *Biomass Convers. Biorefin.* **11** (2021) 1775 (https://doi.org/10.1007/s13399-020-00714-0)

22. X. Hu, M. Gholizadeh, *J. Energy Chem.* **39** (2019) 109 (https://doi.org/10.1016/j.jechem.2019.01.024)

23. N. Panwar, A. Pawar, B. Salvi, *SN Appl. Sci.* **1** (2019) 1 (https://doi.org/10.1007/s42452-019-0172-6)

24. B. Deng, X. Yuan, E. Siemann, S. Wang, H. Fang, B. Wang, Y. Gao, N. Shad, X. Liu, W. Zhang, *J. Waste Manage.* **120** (2021) 33 (https://doi.org/10.1016/j.wasman.2020.11.015)

25. R. R. Domingues, P. F. Trugilho, C. A. Silva, I. C. N. d. Melo, L. C. Melo, Z. M. Magriotis, M. A. Sánchez-Monedero, *PloS One* **12** (2017) e0176884 (https://doi.org/10.1371/journal.pone.0176884)

26. S. Khajavi-Shojaei, A. Moezzi, M. Norouzi Masir, M. Taghavi, *Biomass Conv. Bioref.* **13** (2023) 593 (https://doi.org/10.1007/s13399-020-01137-7)

27. Y. Li, D. Xu, Y. Guan, K. Yu, W. Wang, *Int. J. Phytoremediation* **21** (2019) 145 (https://doi.org/10.1080/15226514.2018.1488806)

28. A. T. Nguyen, T. A. Bui, N. T. Mai, H. T. Tran, S. V. Tran, N. H. Nguyen, T. Tsubota, Y. Shinogi, S. Dultz, M. N. Nguyen, *J. Agron.* **112** (2020) 1713 (https://doi.org/10.1002/agj2.20209)

29. A. Tomczyk, Z. Sokołowska, P. Boguta, *Rev. Environ. Sci. Biotechnol.* **19** (2020) 191 (https://doi.org/10.1007/s11157-020-09523-3)
30. D. F. d. O. Torchia, E. Zonta, A. M. de Andrade, A. C. García, *Braz. J. Chem. Eng.* **39** (2022) 415 (https://doi.org/10.1007/s43153-021-00147-w)
31. S. K. Das, G. K. Ghosh, R. Avasthe, K. Sinha, *J. Environ. Manage.* **278** (2021) 111501 (https://doi.org/10.1016/j.jenvman.2020.111501)
32. S. Yu, W. Zhang, X. Dong, F. Wang, W. Yang, C. Liu, D. Chen, *J. Environ. Chem. Eng.* (2023) 111638 (https://doi.org/10.1016/j.jece.2023.111638)
33. D. Xu, J. Cao, Y. Li, A. Howard, K. Yu, *Waste Manage.* **87** (2019) 652 (https://doi.org/10.1016/j.wasman.2019.02.049)
34. Q. Liu, B. Liu, Y. Zhang, T. Hu, Z. Lin, G. Liu, X. Wang, J. Ma, H. Wang, H. Jin, *Global Change Biol.* **25** (2019) 2077 (https://doi.org/10.1111/gcb.14613)
35. M. M. Afessa, P. Debiagi, A. I. Ferreiro, M. A. Mendes, T. Faravelli, A. V. Ramayya, *J. Anal. Appl. Pyrol.* **162** (2022) 105435 (https://doi.org/10.1016/j.jaap.2022.105435)
36. S. Yousef, J. Eimontas, N. Striūgas, M. A. Abdelnaby, *Renew. Energy* **173** (2021) 733 (https://doi.org/10.1016/j.renene.2021.04.034)
37. T. Wang, H. Liu, C. Duan, R. Xu, Z. Zhang, D. She, J. Zheng, *Materials* **13** (2020) 3391 (https://doi.org/10.3390/ma13153391)
38. A. Bayata, G. Mulatu, *Am. J. Chem. Eng.* **13** (2024) 13 (https://doi.org/10.11648/j.ajche.20241202.11)
39. Z. R. Gajera, K. Verma, S. P. Tekade, A. N. Sawarkar, *Bioresour. Technol. Rep.* **11** (2020) 100479 (https://doi.org/10.1016/j.biteb.2020.100479)
40. B. C. Chaves Fernandes, K. Ferreira Mendes, A. F. Dias Júnior, V. P. da Silva Caldeira, T. M. da Silva Teófilo, T. Severo Silva, V. Mendonça, M. de Freitas Souza, D. Valadão Silva, *Materials* **13** (2020) 5841 (https://doi.org/10.3390/ma13245841)
41. J. W. Wong, U. O. Ogbonnaya, *Environ. Sci. Pollut. Res.* **28** (2021) (https://doi.org/10.1007/s11356-021-14803-8)
42. N.-T. Vu, K.-U. Do, *Biomass Conv. Bioref.* **13** (2023) 2193 (https://doi.org/10.1007/s13399-021-01337-9).

SUPPLEMENTARY MATERIAL TO
Effect of pyrolysis temperature and time of Robusta coffee husk on yield and product characteristics

THI THU HUONG NGUYEN*, NGOC TOAN VU, HONG MINH LE
and HONG SON NGUYEN

*Department of Chemical and Radiological Toxicology Technology Research,
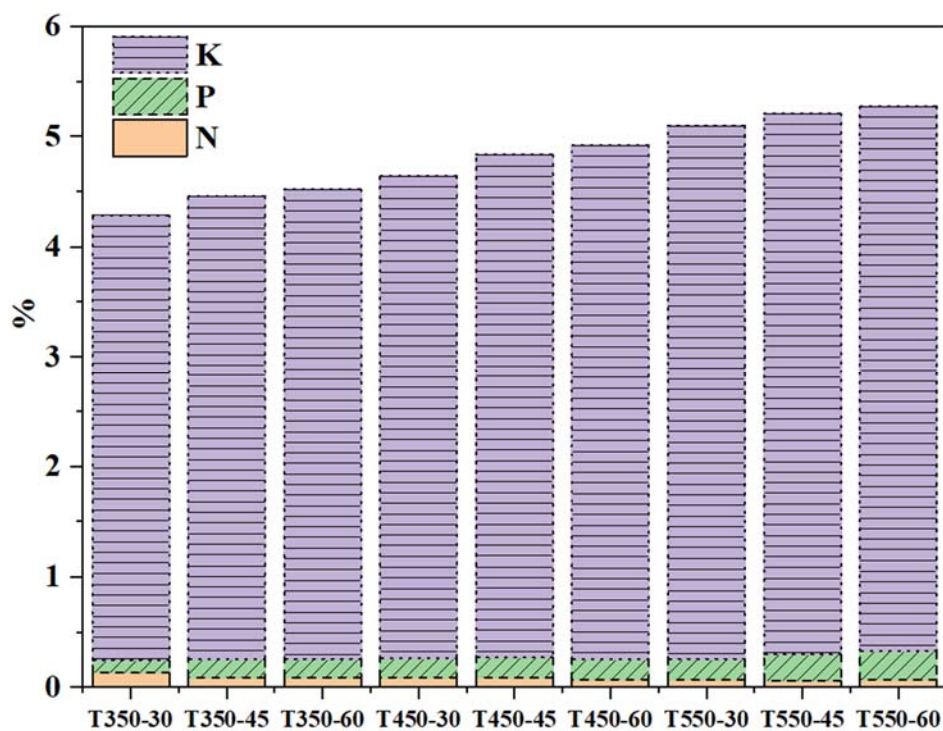Institute of New Technology, Hanoi, Vietnam*

Fig. S-1. Biochar's total nitrogen, phosphorus, and potassium content at different pyrolysis temperatures and times

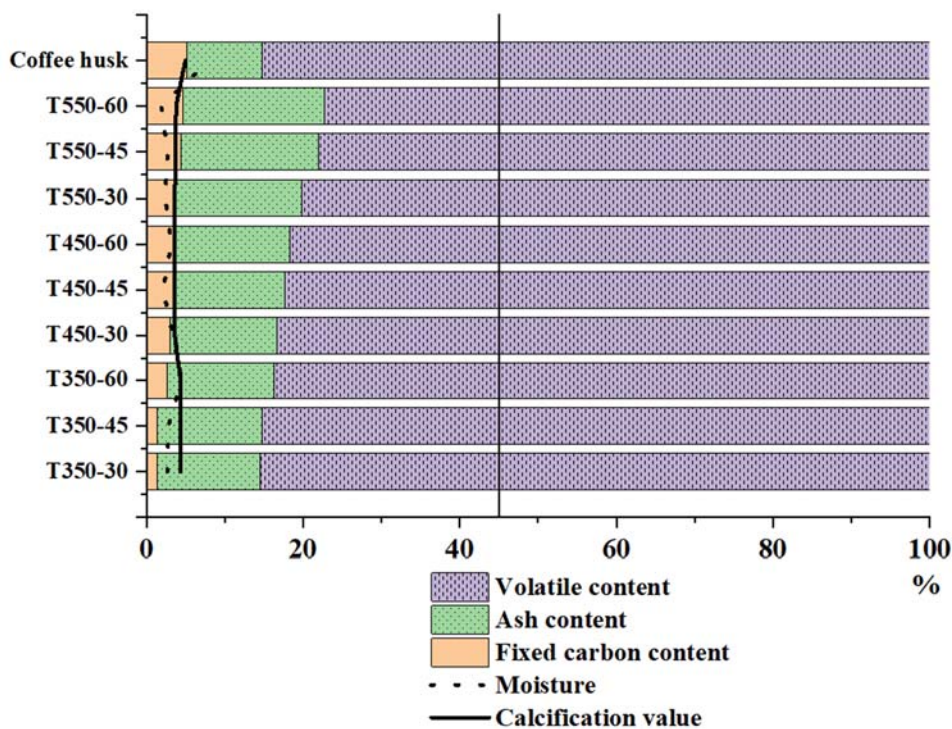* Corresponding author. E-mail: huong93mta@gmail.com

Fig. S-2. The average physicochemical characteristics of coffee husks and biochar from coffee husks at different pyrolysis temperatures and times

Table S-I. Functional groups in the FTIR spectrum

Wavelength, cm^{-1}	Functional groups
3400-3700	Vibrations of -OH bonds from H_2O, phenol, and organic acids.[44]
2850-2950	Vibrations of the stretched C-H bond of aliphatic CH_x.[44,45]
1700-1750	Vibrations of C=C bonds of aromatic and olefinic rings.[44,46]
1600-1650	Vibrations of C=C bonds of lignin and hemicellulose.[44,45] Vibrations of C=O bonds of amide (I), ketones and chinons.[44,45]
1500-1590	Oscillation of the asymmetric COO- bond.[46]
1400-1460	C-H change of CH_3 group.[47]
1200-1270	Phenolic -OH group.[24]
1000-1110	Symmetric elongation of C-O-C in ester groups of cellulose, hemicellulose, and methoxyl groups of lignin.[44,45]
460-990	Vibration of Si-O bond.[45]

Kinetic and equilibrium comparison of methylene blue and basic blue 41 adsorption by silica fume

SHOHRE MORTAZAVI[1]*, MIKA SILLANPÄÄ[2–5] and DEBAJYOTI BOSE[6]

[1]Semnan University, Department of Chemical, Petroleum and Gas Engineering, Semnan, Iran, [2]Saveetha School of Engineering, Saveetha Institute of Medical and Technical Sciences, Saveetha University, Chennai, India, [3]Centre of Research Impact and Outcome, Chitkara University Institute of Engineering and Technology, Chitkara University, Punjab, India, [4]Department of Civil Engineering, University Centre for Research & Development, Chandigarh University, Gharuan, Mohali, Punjab, India, [5]Sustainability Cluster, School of Advanced Engineering, UPES, Bidholi, Dehradun, India and [6]AI-Research Centre, School of Business, Woxsen University, Hyderabad, Telangana, India

Abstract: The complex molecular structures of synthetic dyes are not easily removed from water, so it is essential to treat dye pollutants before they enter the aquatic environments. In this study, cost-effective industrial waste silica fume (SF) was used as an adsorbent to investigate the adsorption of methylene blue (MB) and basic blue 41 (BB-41). The structure of the silica fume adsorbent was characterized using the FESEM technique, which confirmed that SF has a porous structure. The adsorption of these cationic dyes was examined using kinetics models (pseudo-first-order and pseudo-second-order) and isotherm models (Langmuir, Temkin, Dubinin–Radushkevich and Freundlich), and the results obtained were compared. Based on the findings, the adsorption process of MB and BB-41 on SF followed pseudo-second-order kinetics. The adsorption of MB and BB-41 on SF followed Freundlich isotherm model. According to Langmuir isotherm data, the maximum adsorption capacity for BB-41 and MB was found to be 41.95 and 189.31 mg/g, respectively.

Keywords: isotherm; wastewater; dye removal; water treatment; industrial waste.

INTRODUCTION

Chemicals enter water through different industries, such as petrochemical, plastic, textile and cosmetic products. Millions of tons of dyes have been used for the colouring materials. Dyes and pigments have complex structures and high stability, making them difficult to remove from wastewater.[1] The toxicity of dyes threatens human health. Long-term contact with these dyes causes bleeding and

---

damage to vital organs. Therefore, it is necessary to find some efficient methods to treat wastewater polluted by dyes.[2]

Methylene blue (MB) is not considered a toxic dye, but long-term inhalation can lead to symptoms such as breathing problems, vomiting, diarrhea and nausea. MB is commonly used for dyeing cloth, wood, and silk.[2,3] Basic blue-41 (BB-41) is a stable mono-azo dye used in various applications from the textile industry to dyeing wool and acrylic materials. BB-41 has the potential to cause permanent damage to vital organs of humans and animals.[4]

Several methods are used to remove pollutants from wastewater, such as elect-rochemical degradation,[5] membrane,[6] adsorption[7,8] and reverse osmosis.[9,10] Electrochemical degradation breaks down pollutants into simpler, less harmful compounds using an electric current.[5] The membrane filtration method removes pollutants using a membrane.[6] The reverse osmosis (RO) is a process which uses pressure to push water through a semipermeable membrane, separating and removing contaminants from the water.[9]

Adsorption is a process in which molecules of a substance, such as dye, adhere to the surface of another material, which can be a solid or a liquid.[11] This mechanism is also an effective method for removing textile dyes from wastewater. Various waste materials have been investigated to remove pollutants from wastewater, such as orange and lemon peels,[12] coconut shell,[13] palm-date stones,[14] ash,[15] almond shells,[16] pistachio shell,[4] Walnut shell,[17] eggshell[18] and steal slug.[19]

In the adsorption process, the determination of the rate limiting step of adsorption is one of the most important parameters. The kinetic studies are conducted to investigate the variables affecting the reaction rate.[20] The equilibrium isotherms of adsorption describe the interaction between the adsorbent and the adsorbate.[21]

The silica fume, a by-product of industrial waste with high purity and permeability, small particle size, high specific surface area, and low specific weight was used to eliminate MB and BB-41. Despite its low cost and easy accessibility, the previous researchers did not investigate the adsorption of cationic dyes using this adsorbent. In this research, we analysed the kinetics and equilibrium isotherms of the adsorption of MB and the BB-41 on SF from an aqueous solution to compare the optimal conditions for the adsorption of MB and BB-41 onto SF. The summary of the present study is illustrated in Fig. 1.

EXPERIMENTAL

The materials used in the study include BB-41 and MB as the synthetic dyes with specific empirical formulas and molecular weights (maximum adsorption wavelength is 610 nm for BB--41 and 665 nm for MB).

The pure SF was obtained from Lorestan Ferroalloy Company, passed through a 60-mesh sieve, and stored. The specific surface area of SF was 18 m^2/g. The chemical composition and surface characteristics (determined by X-ray fluorescence) are presented in **Error! Reference source not found.**I. The maximum wavelength of the colours was determined using a

spectrophotometer (PC 1650-UV, Shimadzu, Japan). Field emission scanning electron microscopy (FESEM, JSM 6400, JEOL, Japan) was used to identify the structure of SF. **Error! Reference source not found.** shows the FESEM image of SF, and it indicates that this industrial waste has a spherical and porous structure.
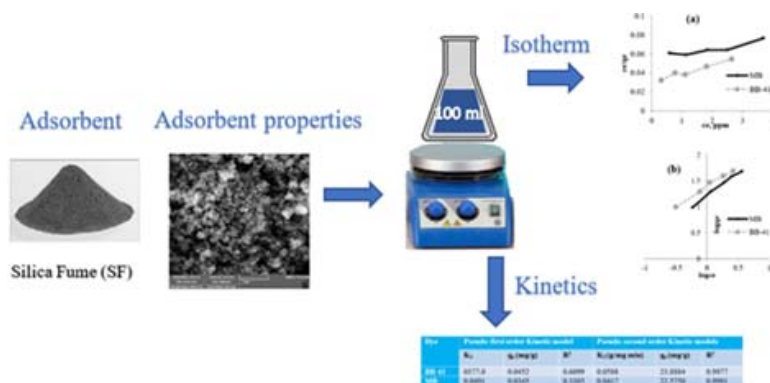

Fig. 1. Schematic of the present study in summary.

TABLE I. Chemical composition and Surface properties of SF

SiO$_2$ (wt. %)	K$_2$O (wt. %)	Al$_2$O$_3$ (wt. %)	Specific surface m^2/g	Density kg/m^3	Pore diameter μm
96.12	0.4	0.82	18	213	13
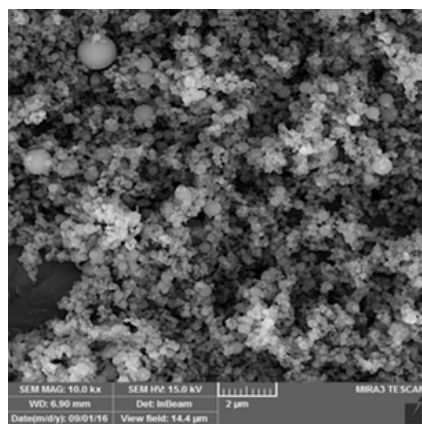
Fig. 2. FESEM structure of SF.

The 50 mg/L solution was diluted with distilled water to various concentrations in a batch system. The experiments were conducted using 0.1 to 0.5 g of adsorbent and 100 ml of solution at room temperature. The adsorption of MB and BB-41 solutions was studied using SF in the pH range of 2–11 for one hour at a speed of 300 rpm. The solution was then centrifuged and the adsorption capacity was determined using a spectrophotometer. The adsorption capacity of q (mg/g) is calculates as follows:[22]

$$q_e = \frac{C_0 - C_f}{M} V \tag{1}$$

The adsorption capacity of MB and BB-41, q, is determined by measuring the initial and final concentrations of the dyes in the aqueous solution, C_0 and C_f, and calculating the adsorption capacity based on the volume of the aqueous solution, V, and the amount of SF used, M.

The Langmuir isotherm is the simplest and most common method for expressing the equilibrium of adsorption.[23]

The Langmuir equation is:

$$\frac{C_e}{q_e} = \frac{1}{q_{max}K_L} + \frac{C_e}{q_{max}} \tag{2}$$

In the equation, q_e represent the amount of substance absorbed by SF (mg/g), C_e is the equilibrium concentration (mg/l), q_{max} is the maximum possible adsorption capacity of MB or BB-41 (mg/g) and K_L is a constant value (l/mg).

The desirability of the adsorption process is evaluated using the dimensionless parameter R_L, known as the separation factor:

$$R_L = \frac{1}{1 + K_L C_0} \tag{3}$$

According to the value of R_L, one of the following conditions may occur:[24]
• Irreversible adsorption occurs when R_L is zero,
• Favourable adsorption occurs when R_L is between 0 and 1 and
• $R_L = 1$ suggests a linear adsorption (C_0 is initial adsorbent (mg/l)).[25]

The Temkin isotherm consider interactions between adsorbates and adsorbents material, while ignoring low and high concentrations. This model assumes a multi-layer adsorption process. The Temkin isotherm is represented by the following equation:[26]

$$q_e = \frac{RT}{b_{TM}} \ln K_{TM} C_e \tag{4}$$

In this equation b_{TM} (J/mol) is related to the heat of 0.05 adsorption, R (8.314 J/(mol K)) is the universal gas constant, T is absolute temperature (K), and K_{TM} (L/mg) is Temkin model constant.

The Dubinin–Radushkevich isotherm considers the pore structure of the adsorbent for heterogeneous surfaces. This isotherm model is used to for physical or chemical adsorption. The Dubinin–Radushkevich equation is:[27]

$$q_e = q_{m,DR} e^{-K_{DR}\varepsilon_{DR}^2} \tag{5}$$

Where $q_{m,DR}$ is the maximum adsorption capacity of the Dubinin–Radushkevich model, K_{DR} is constant (mol^2/kJ^2), and ε_{DR} (kJ mol^{-1}) is calculated by the following equation:

$$\varepsilon_{DR} = RT \ln(1 + \frac{1}{C_e}) \tag{6}$$

The Freundlich isotherm model is a mathematical relationship based on empirical observations, designed to describe non-ideal and reversible adsorption. Like the Langmuir isotherm, this model is used to quantitatively determine equilibrium and heterogeneous adsorption systems. Freundlich's linear equation is:[28]

$$\log q_{\mathrm{e}} = \log K_{\mathrm{f}} + \frac{1}{n} \log C_{\mathrm{e}} \tag{7}$$

The pseudo-first-order kinetic model presents the adsorption rate of a soluble substance from the environment. This kinetic model is for the physical adsorption of the solute on the adsorbent. It indicates a weak interaction between the dissolved ions and the adsorbent. The pseudo-first-order kinetic model is expressed as follows:[14]

$$\ln(q_{\mathrm{e}} - q_t) = \ln q_{\mathrm{e}} - K_1 t \tag{8}$$

The adsorption capacity at time t, q_t, and at equilibrium time, q_{e}, are determined and compared. The pseudo-first-order kinetic model rate constant, K_1, describes the rate of adsorption and is calculated based on the data obtained. The pseudo-second-order model is based on the solid phase. Unlike other models, this model describes the adsorption behaviour in the entire adsorption range and shows that chemical adsorption is the slowest step and controls adsorption processes. The equation of the model is expressed as follows:[29]

$$\frac{t}{q_t} = \frac{1}{K_2 q_{\mathrm{e}}^2} + \frac{t}{q_{\mathrm{e}}} \tag{9}$$

K_2 is the apparent rate constant (g/(mg min)) which is a complex function of concentration. The width from the origin and the slope of the t/q_{e} line in terms of t, respectively, are obtained by the constant values of the speed and the amount of equilibrium adsorption predicted by the pseudo-second-order kinetic model.

RESULTS AND DISCUSSION

Error! Reference source not found. illustrates the impact of pH on the adsorption capacity of MB and BB-41 using SF. As the pH increased from 2 to 11, the adsorption capacity increased from 7.69 to 15.73 mg/g for MB and from 8.76 to 16.64 mg/g for BB-41. It is evident that at higher pH levels, the electrostatic force of the attraction between the dye and the adsorbent increases, resulting in the increase in adsorption capacity. The maximum adsorption capacity was observed at pH 10 for both MB and BB-41.
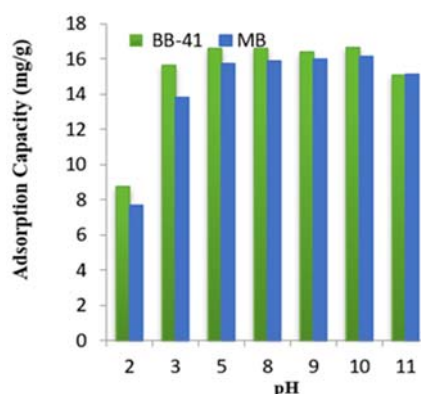

Fig. 3. Effect of pH on MB and BB-41 adsorption using SF (pH 2 to 11 at 25 °C).

To evaluate the effect of contact time on the adsorption capacity of MB and BB-41 onto SF, a series of experiments were conducted over a period of 20 to 90 min (**Error! Reference source not found.**). The results showed that the equilibrium was achieved within 30 min for MB and 20 min for BB-41.
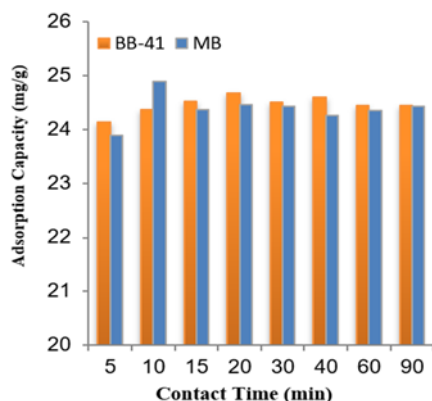
Fig. 4. Effect of contact time of MB and BB-41 on adsorption process using SF (at pH 10 and 25 °C).

Error! Reference source not found. demonstrates the effect of concentrations of MB and BB-41 on the adsorption capacity using SF at pH 10. The adsorption capacity increased with the rise in the concentrations of MB and BB-41, from 20 to 100 mg/L.
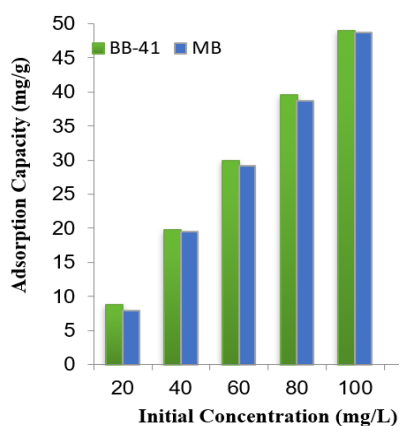
Fig. 5. Effect of initial concentration of MB and BB-41 on adsorption process using SF (at pH 10 and 25 °C).

Isotherm study

The isotherm equations were examined in order to investigate the balance of BB-41 and MB dye removal process. According to **Error! Reference source not found.**, the adsorption process of MB on SF follows the Freundlich isotherm. The maximum adsorption capacity of the Langmuir monolayer was obtained 189.31

mg/g. The adsorption process of BB-41 on SF was also fitted to the Freundlich isotherm.

The Langmuir isotherm analysis revealed that the separation factor R_L for both MB and BB-41 was found to be in the range of 0 to 1, suggesting that the adsorption process was favourable. The maximum adsorption capacity of the Langmuir monolayer for BB-41 was calculated to be 108.95 mg/g.

TABLE II. Parameters of isotherm models for removal of MB and BB-41 on SF

Model	BB-41	MB
Langmuir		
q_{max} / mg g^{-1}	108.9482	189.3101
K_L / L mg^{-1}	0.3075	0.0970
R_L	0.0752	0.1467
R^2	0.9588	0.8473
Temkin		
b_T	134.6605	117.3272
A_T / L g^{-1}	4.6603	2.4972
R^2	0.9672	0.9773
Dubinin–Radushkevich		
q_s / mg g^{-1}	43.2213	44.3289
β / mol^2 kJ^{-1}	7.9814×10^6	3.7931 × 10^6
E / kJ mol^{-1}	0.025	0.004
R^2	0.9227	0.9443
Freundlich		
K_F	24.4589	16.3956
N	1.3059	1.1304
R^2	0.9906	0.9909

Kinetics study

Pseudo-first-order and pseudo-second-order kinetic equations were investigated for the adsorption of BB-41 and MB on SF.

As it is shown in **Error! Reference source not found.**, the adsorption of BB-41 on SF follows pseudo-second-order kinetics ($R^2 = 0.9977$). Similarly, the adsorption process of MB on SF also follows the pseudo-second-order kinetic model ($R^2 = 0.9991$).

TABLE III. Parameters of kinetic models for the adsorption of BB-41 and MB on SF

Dye	Pseudo-first order kinetic model			Pseudo-second order kinetic models		
	K_1	q_e / mg g^{-1}	R^2	K_2 / mg g^{-1} min^{-1}	q_e / mg g^{-1}	R^2
BB-41	0377.0	0.0452	0.6099	0.0588	23.8884	0.9977
MB	0.0491	0.0345	0.3385	0.0417	22.5750	0.9991

CONCLUSION

In this study, SF industrial waste was evaluated for its ability to remove cationic dyes BB-41 and MB from aqueous solutions in a batch adsorption process. The kinetics and the isotherm of MB and BB-41 adsorption on SF were compared. The results indicated that the adsorption kinetics for both dyes followed the pseudo-second order model, and the isotherm data were well-described by the Freundlich model. Based on the findings, FESEM images of SF revealed a spherical and porous structure for this industrial waste. Additionally, due to its non-toxic nature, accessibility, low cost and high adsorption capacity, SF can serve as a cost-effective adsorbent for eliminating coloured pollutants from wastewater. Expand the research by chemically or physically modifying SF to improve its adsorption capacity for other contaminants such as heavy metals and pharmaceuticals, allowing for a broader range of applications. To fully manage its potential, the following strategic actions are recommended:

•   The future development of silica fume applications should align with circular economy principles. Efforts must focus on ensuring that silica fume is sourced sustainably, potentially through partnerships with industries that produce this byproduct.

•   The comprehensive evaluations, including life cycle assessments, toxicity assessments, and ecological impact studies, are essential to ensure compliance with environmental regulations and to build public trust in this technology.

•   The future research should prioritize the exploration of eco-friendly modification techniques for silica fume that enhance its adsorption capacity. Engaging local communities in projects involving silica fume for wastewater treatment can enhance industrial acceptance of its benefits.

Some further investigations are needed into the regeneration of silica fume after its use in dye removal processes. The exploring methods to effectively restore its adsorptive capabilities can significantly enhance the economic feasibility of silica.

ИЗВОД

ПОРЕЂЕЊЕ КИНЕТИКЕ И РАВНОТЕЖЕ АДСОРПЦИЈЕ МЕТИЛЕНСКОГ ПЛАВОГ И
BASIC BLUE-41 НА МИКРОСИЛИЦИ

HOHRE MORTAZAVI[1], MIKA SILLANPÄÄ[2-5] и DEBAJYOTI BOSE[6]

[1]*Semnan University, Department of Chemical, Petroleum and Gas Engineering, Semnan, Iran,* [2]*Saveetha Shool of Engineering, Saveetha Institute of Medical and Technical Sciences, Saveetha University, Chennai, India,* [3]*Centre of Research Impact and Outcome, Chitkara University Institute of Engineering and Technology, Chitkara University, Punjab, India,* [4]*Department of Civil Engineering, University Centre for Research & Development, Chandigarh University, Gharuan, Mohali, Punjab, India,* [5]*Sustainability Cluster, School of Advanced Engineering, UPES, Bidholi, Dehradun, India* и [6]*AI-Research Centre, School of Business, Woxsen University, Hyderabad, Telangana, India*

Синтетичке боје сложених молекулских структура тешко се уклањају из воде, због чега је неопходно третирати загађиваче боја пре њиховог уласка у водене екосистеме. У овој студији, као адсорбенс коришћен је економичан индустријски отпад микросилика (SF) ради

испитивања адсорпције метиленског плавог (MB) и *basic blue*-41 (BB-41). Структура адсорбенса од микросилике окарактерисана је техником FESEM, којом је потврђено да SF има порозну структуру. Адсорпција ових катјонских боја испитивана је применом кинетичких модела (псеудо-првог реда и псеудо-другог реда) и изотермских модела (*Langmuir*, *Temkin*, *Dubinin–Radushkevich* и *Freundlich*), а добијени резултати су међусобно упоређени. На основу резултата, процес адсорпције MB и BB-41 на SF следио је кинетику псеудо-другог реда. Адсорпција MB и BB-41 на SF пратило се Фројндлиховим изотермским моделом. Према подацима Ленгмирове изотерме, максимални капацитет адсорпције за BB-41 и метиленског плавог је износио 41,95 mg g^{-1}, односно 189,31 mg g^{-1}.

REFERENCES

1. C. Osagie, A. Othmani, S. Ghosh, A. Malloum, Z. Kashitarash Esfahani, S. Ahmadi, *J. Mater. Res. Technol.* **14** (2021) 2195 (https://doi.org/10.1016/j.jmrt.2021.07.085)
2. P. O. Oladoye, T. O. Ajiboye, E. O. Omotola, O. J. Oyewola, *Results Eng.* **16** (2022) 100678 (https://doi.org/10.1016/j.rineng.2022.100678)
3. S. T. Al-Asadi, F. F. Al-Qaim, *Research Square* **1** (2023) 1 (https://doi.org/10.21203/rs.3.rs-2449414/v1)
4. İ. Şentürk, M. Alzein, *Sustain. Chem. Pharm.* **16** (2020) 100254 (https://doi.org/10.1016/j.scp.2020.100254)
5. Y. Wang, M. Chen, C. Wang, X. Meng, W. Zhang, Z. Chen, J. Crittenden, *Chem. Eng. J.* **374** (2019) 626 (https://doi.org/10.1016/j.cej.2019.05.217)
6. S. Yu, H. Pang, S. Huang, H. Tang, S. Wang, M. Qiu, Z. Chen, H. Yang, G. Song, D. Fu, *Sci. Total Environ.* **800** (2021) 149662 (https://doi.org/10.1016/j.scitotenv.2021.149662)
7. A. Ashraf, J. Dutta, A. Farooq, M. Rafatullah, K. Pal, G. Z. Kyzas, *J. Mol. Struct.* **1309** (2024) 138225 (https://doi.org/10.1016/j.molstruc.2024.138225)
8. H. Bensalah, S. A. Younssi, M. Ouammou, A. Gurlo, M. F. Bekheet, *J. Environ. Chem. Eng.* **8** (2020) 103807 (https://doi.org/10.1016/j.jece.2020.103807)
9. R. H. Hailemariam, Y. C. Woo, M. M. Damtie, B. C. Kim, K.-D. Park, J.-S. Choi, *Adv. Colloid Interf. Sci.* **276** (2020) 102100 (https://doi.org/10.1016/j.cis.2019.102100)
10. C. F. Couto, A. V. Santos, M. C. S. Amaral, L. C. Lange, L. H. De Andrade, A. F. S. Foureaux, B. S. Fernandes, *J. Water Proc. Eng.* **33** (2020) 101029 (https://doi.org/10.1016/j.jwpe.2019.101029)
11. S. Mortazavi, E. Najafi Kani. *J. Turkish Chem. Soc., B* **6** (2023) 35 (https://doi.org/10.58692/jotcsb.1240859)
12. D. Ramutshatsha-Makhwedzha, A. Mavhungu, M. L. Moropeng, R. Mbaya, *Heliyon* **8** (2022) e09930 (https://doi.org/10.1016/j.heliyon.2022.e09930)
13. A. K. Prajapati, M. K. Monda, *J. Mol. Liq.* **307** (2020) 112949 (https://doi.org/10.1016/j.molliq.2020.112949)
14. M. Wakkel, B. Khiari, F. Zagrouba. *J. Taiwan Ins. Chem. Eng.* **96** (2019) 439 (https://doi.org/10.1016/j.jtice.2018.12.014)
15. R. Wu, A. H. Jawad, E. Kashi, S. A. Musa, Z. A. Alothman, *J. Polym. Environ.* **32** (2024) 6390 (https://doi.org/10.1007/s10924-024-03388-1)
16. I. Loulidi, F. Boukhlifi, M. Ouchabi, A. Amar, M. Jabri, A. Kali, S. Chraibi, C. Hadey, F. Aziz, *Sci. World J.* **2020** (2020) 5873521 (https://doi.org/10.1155/2020/5873521)
17. M. K. Uddin, A. Nasar, *Sci. Rep.* **10** (2020) 7983 (https://doi.org/10.1038/s41598-020-64745-3)

18. S. Rajoriya, V. K. Saharan, A. S. Pundir, M. Nigam, K. Roy, *Cur. Res. Green Sust. Chem.* **4** (2021) 100180 (https://doi.org/10.1016/j.crgsc.2021.100180)

19. M. S. Manzar, G. Khan, P. V. Dos Santos Lins, M. Zubair, S. U. Khan, R. Selvasembian, L. Meili, N. I. Blaisi, M. Nawaz, H. A. Aziz, T. S. Kayed, *J. Mol. Liq.* **339** (2021) 116714 (https://doi.org/10.1016/j.molliq.2021.116714)

20. M. Benjelloun, Y. Miyah, G. A. Evrendilek, F. Zerrouq, S. Lairini, *Arabian J. Chem.* **14** (2021) 103031 (https://doi.org/10.1016/j.arabjc.2021.103031)

21. H. Bensalah, S. A. Younssi, M. Ouammou, A. Gurlo, M. F. Bekheet, *J. Environ. Chem. Eng.* **8** (2020) 103807 (https://doi.org/10.1016/j.jece.2020.103807)

22. J. Benvenuti, A. Fisch, J. H. Z. Dos Santos, M. Gutterres, *J. Environ. Chem. Eng.* **7** (2019) 103342 (https://doi.org/10.1016/j.jece.2019.103342)

23. K. Y. Foo, B. H. Hameed, *Chem. Eng. J.* **156** (2010) 2 (https://doi.org/10.1016/j.cej.2009.09.013)

24. A. Sarı, Ç. Demirhan, M. Tuzen, *Chem. Eng. J.* **162** (2010) 521 (https://doi.org/10.1016/j.cej.2010.05.054)

25. M. A. Al-Ghouti, D. A. Da'ana, *J Hazard. Mater.* **393** (2020) 122383 (https://doi.org/10.1016/j.jhazmat.2020.122383)

26. M. M. Majd, V. Kordzadeh-Kermani, V. Ghalandari, A. Askari, M. Sillanpää, *Sci. Total Environ.* **812** (2022) 151334 (https://doi.org/10.1016/j.scitotenv.2021.151334)

27. B. S. Rathi, P. S. Kumar, *Environ. Pollut.* **280** (2021) 116995 (https://doi.org/10.1016/j.envpol.2021.116995)

28. S. Mortazavi, M. Sillanpaa, D. Bose. *Int. J. Environ. Anal. Chem.* (2024) (https://doi.org/10.1080/03067319.2024.2426003)

29. A. Bosacka, M. Zienkiewicz-Strzalka, A. Derylo-Marczewska, A. Chrzanowska, M. Blachnio, B. Podkoscielna, *Front. Chem.* **11** (2023) 1176718 (https://doi.org/10.3389/fchem.2023.1176718).